IN SITU SMALL SCALE MECHANICAL CHARACTERIZATION OF MATERIALS UNDER ENVIRONMENTAL EFFECTS

A Thesis

by

MATTHEW WAYNE SANDERS

Submitted to the Office of Graduate Studies of
Texas A&M University
in partial fulfillment of the requirements for the degree of

MASTER OF SCIENCE

August 2010

Major Subject: Mechanical Engineering

IN SITU SMALL SCALE MECHANICAL CHARACTERIZATION OF MATERIALS UNDER ENVIRONMENTAL EFFECTS

A Thesis

by

MATTHEW WAYNE SANDERS

Submitted to the Office of Graduate Studies of
Texas A&M University
in partial fulfillment of the requirements for the degree of

MASTER OF SCIENCE

Approved by:

Chair of Committee,	Hong Liang
Committee Members,	Karl Hartwig
	Jorge L. Alvarado
Head of Department,	Dennis O'Neal

August 2010

Major Subject: Mechanical Engineering

ABSTRACT

In Situ Small Scale Mechanical Characterization of Materials Under Environmental Effects. (August 2010)

Matthew Wayne Sanders, B.S., Texas A&M University

Chair of Advisory Committee: Dr. Hong Liang

This research investigates the mechanical properties and performance of structural materials at a small volume scale. In situ observation was made possible through the Small Punch Test (SPT) method as well as tribological testing. Experimentally, aluminum and titanium alloys were examined using those two techniques. Analysis of their behavior in comparison with their published mechanical properties made it possible to establish connections between test parameters and conventional uniaxial tensile test properties. Connections were generated between SPT parameters and tribological performance.

This research used experimental approaches to develop an understanding of the material behaviors during small punch testing and apply them to hydrogen embrittlement. The SPT for such alloys were highly repeatable and specimen surface roughness did not have visible impacts on repeatability. Analysis indicated that there is a link between the SPT and conventional mechanical properties. The relationship between the applied force and the slop of the FvE curve is associated with the tensile strength and elastic modulus. It was found that the SPT can be used to qualitatively gage wear

resistance. The SPT was used to analyize hydrogen effects, and no significant effects were seen on 3003-H14 and 2618-T61 aluminum alloys; however, effects were seen on a Ti-6Al-4V alloy. It was also found that hydrogen showed no visible effects on friction and wear. The SPT can now be applied more accurately to the testing of aluminum alloys and new doors for the potential of small punch testing in the application of hydrogen embrittlement and surface characterization have been opened.

This thesis consists of six chapters. The first chapter serves as an introduction to the background necessary to understand the rational and motivation for the present research. The second chapter will go into detail about the motivation and the objects of the research while the third chapter will explain the experimental procedures that were conducted to fulfill these objectives. The fourth chapter will present the results of these experiments, and they will be discussed in the fifth chapter. Finally, in the sixth chapter, conclusions will be stated and future work will be discussed.

ACKNOWLEDGEMENTS

I would first and foremost like to thank my committee chair, Dr. Liang for all of her wisdom, guidance, patience, and understanding. I would also like to thank my committee members, Dr. Hartwig, and, Dr. Alvarado for their guidance and support throughout the course of this research.

I would also like to thank all of my friends and colleagues, especially the members of the Liang research group for their listening ears and constructive comments. I would like to acknowledge Texas A&M University and the mechanical engineering department faculty and staff. I would also like to thank the National Science Foundation and ConceptsNRC for support in this research.

I also want to thank my mother for her encouragement, amazing love, wisdom, and for setting a great example of hard work and self-sacrificing love. I want to thank, my best friend, my beautiful wife for her patience, never-ending love, proofreading boring engineering papers, and always supporting me in everything I do. She is a great example of an amazing Christian, women, friend, and wife.

Finally, I would like to acknowledge my Lord and savior Jesus Christ for his sacrifice for my sins. May all my work bring glory and honor to him whose will is my purpose. The more I learn about science the more I learn how amazing God is. Being able to explore his creation is an awesome worship experience.

NOMENCLATURE

d	Ball bearing diameter [mm]
D	Clamping Jig hole diameter [mm]
E	Modulus of Elasticity [GPa]
F	Punch force [N]
F_c	Specimen clamping force [N]
F_{max}	Maximum punch force [N]
F_y	Point of deviation from linearity [N]
FvE	Force versus extension
J_{IC}	Fracture toughness [$N/m^{3/2}$]
R	Ball bearing radius [mm]
SPT	Small Punch Test
δ	Punch displacement [mm]
μ	Coefficient of friction
υ	Posson's ratio
σ	Stress
σ_{uts}	Ultimate tensile stress
σ_y	Yield Stress
WEDM	Wire Electo Discharge Machine

TABLE OF CONTENTS

Page

CHAPTER Page

LIST OF FIGURES

Page

Page

Page

Page

LIST OF TABLES

Page

CHAPTER I

INTRODUCTION

This chapter will introduce the need for better energy technologies and how hydrogen is a proposed solution, as well as some of the challenges associated with it. Details will be discussed on how hydrogen affects metals and how the mechanical properties of materials can be determined. A discussion will be given about the history and development of the small scale testing technique known as the Small Punch Test.

1.1. Energy Needs

The rate of world energy consumption has been estimated to be 15 Terawatts[1]. This amounts to $473x10^{18}$ Joules of energy used on earth every year. As human civilization becomes more technologically advanced, the amount of energy consumed will continue to increase. This means that the development of better energy technology is crucial for the development of mankind. According to the Department of Energy's Energy Information Administration, in 2007, 36 % of the world's energy was consumed through the burning of petroleum and 27 % by the burning of coal[2]. The amount of energy consumed through the utilization of renewable resources was only 7.2 % of the world's total energy used and only 3.7% was used for the United States[2-3]. This means that over 65 % of the world's energy comes from non-renewable fossil fuels including petroleum, natural gas, and coal. For the United States this number increases to 85 %[3]. With such a large amount of the energy needs being met by a resource that is limited and will one day expire, a great deal of pressure has been put on the need to move to a more

---

This thesis follows the style of *Journal of Testing and Evaluation*.

abundant source of energy production. The concern for the environmental impact of the burning of fossil fuels has, as well as, the growing price of such fuels has led to renewable energy sources becoming the fastest growing source of world energy[4]. Many types of renewable energy sources have received a lot of attention including; nuclear fusion, nuclear fission, geothermal, hydroelectric, solar cells, and wind energy. Figure 1 shows the distribution of world energy consumption by industry[2]. As the figure shows, about 37% of the world's energy is consumed for industrial purposes such as manufacturing and construction. The next largest energy consumption sector is personal and commercial transportation, which consumes about 20% of the world's energy. Over a quarter of the world's energy is lost through energy production inefficiencies and transportation. Oil is expected to remain the world's largest source of energy throughout all sectors until a feasible alternative is available[4]. However, with an ever increasing demand for energy, depleting oil reserves, and instability in the oil reserve nations the search for better energy sources is becoming more and more important. The most promising alternative is to replace liquid petroleum based fuels with hydrogen as an energy transport medium. Hydrogen is the most profuse element that has been seen to exist in the universe. In terms of liquid fuels hydrogen is a fuel that has a high specific energy content [5-6]. Hydrogen's energy yield is 2.75 times greater than the energy yield of hydrocarbon based fuels [7]. If the use of hydrogen could replace the gasoline, diesel, and petroleum based fuels in the transportation sector, over 20% of the world's energy could be saved. The chemical energy stored in the atomic bonds of hydrogen molecules can be transferred to electrical or kinetic energy without

the production of potentially harmful carbon dioxide gases. This means that hydrogen is being portrayed as a clean fuel alternative. It is the burning of limited resources that causes concern for not only how future energy needs will be met, but also the environmental impact of the burning of these fuels.

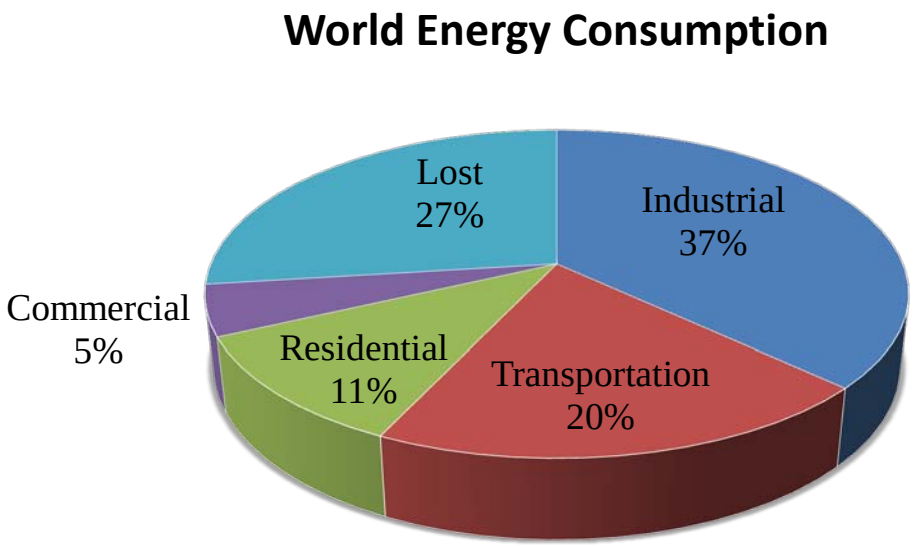

Figure 1: World energy consumption by industry[2]

Apart from energy production, energy storage and transport present themselves as areas where great improvement is needed. If hydrogen is to be truly considered as a replacement for petroleum based fuels many questions need to be answered about how viable this alternative is and if it can safely be used in the same capacity as current technologies. Many premature failures have been seen in metals that have been exposed to hydrogen[8-9]. Questions still remain about how hydrogen can be safely stored and

transported. In particular, how the strength, toughness, and wear resistance of titanium and aluminum alloys are affected by the presence of hydrogen.

1.2. Hydrogen Damage

With hydrogen showing itself as a viable contribution to the ever-growing energy need of humans, more and more components and structures will come in contact with hydrogen atoms. Therefore, an understanding of the effects hydrogen has on different materials is extremely important. A very brief review of some of the mechanisms of hydrogen damage will be presented here including the relatively unexplored area of trbiological influences resulting from hydrogen exposure.

1.2.1. Hydrogen Effects on Metals

Hydrogen within the matrix of a metal can change how a material behaves under load and can result in premature failure due to what is termed hydrogen damage. With only one proton and one electron, hydrogen is the smallest atom in the periodic table. Due to this property, atomic hydrogen can easily diffuse through steel and other metals[10]. Molecular hydrogen , H_2, however cannot diffuse through most metals[10]. This means that the basic mechanism for hydrogen damage occurs because of the presence of the atomic state of hydrogen within a material. Unpaired hydrogen atoms can become present at the surface of a material anytime a hydrogen electrolyte or molecular hydrogen is present. Hydrogen molecules can collect at the surface of a metal though an electrochemical process of hydrogen reduction. Hydrogen atoms can be found in many processes including sour well operations, hydrogen gas production, hydrogen compression to form liquid hydrogen for space craft fuel, acidic cleaning processes, and

in many chemical storage tanks. A common occurrence where hydrogen can be absorbed into a metal is during its forming process, while the metal is in its liquid state. The diffusion of hydrogen has been shown to be greater in liquid metal[9]. While a metal is in its liquid state it can absorb hydrogen from moisture in the surrounding atmosphere. The cleaning of metals through the use of acids is another common way hydrogen is introduced to the surface of a material. Acid pickling can create a hydrogen atom concentration at the surface of a material that is much greater than the concentration found through exposure to high pressure pure hydrogen gas[9]. Hydrogen damage is a term referring to the resulting failure of a material due to its interaction or absorption of hydrogen.

The effect of hydrogen in steels has been extensively studied and it has been shown that mechanical properties can be affected [11-17]. The mechanisms of how steels are affected have been attributed to the ability of hydrogen atoms to collect at locations such as dislocations, voids, defects, grain boundaries, and element interfaces[16]. With the history of the susceptibility of steels to hydrogen embrittlement aluminum and titanium alloys present themselves as natural candidates for uses in the hydrogen energy solution. Generally, there are four types of hydrogen damage that can be identified in failures relating to hydrogen exposure. The main mechanisms of hydrogen's effect on mechanical properties include: hydrogen blistering, hydrogen attack, hydrogen induced cracking, and hydrogen embrittlement. All of these mechanisms are not completely understood and research continues in these areas in order to help develop an understanding so that better preventative measures can be

implemented. All of these effects can occur anytime hydrogen is present, however, hydrogen attack is usually referred to as a high-temperature process[10]. These topics will now be discussed in further detail.

1.2.2. Hydrogen Blistering

Hydrogen blistering occurs when atomic or nascent hydrogen diffuses into the atomic matrix and collects at openings within the material. The nascent hydrogen is small enough that it can freely move throughout the matrix. Seeking a lower energy state, the nascent hydrogen will collect inside voids[10], defects, or around grain boundaries. Once collected, the individual atoms will form hydrogen molecules. The molecules then become much larger than the individual atoms and are trapped and cannot continue to diffuse through the matrix. A visual depiction of this process can be seen in Figure 2. The concentration of these molecules will continue to increase causing the pressure inside this space to increase. This pressure will cause unforeseen internal stresses that can lead to rapid crack propagation and premature failure. The formation and opening of crack tips in these voids due to the hydrogen presence can also increase the vulnerability of a material to fatigue. The internal pressure can sometimes be large enough to plastically deform the material and cause visible extrusions or “blisters” on the exterior of the surface of the material. This can aid a watchful inspector in the sustainability of a component. Hydrogen blistering can be controlled through the use of coatings, “clean” steel, inhibitors, and avoiding exposure to corrosive environments[10].

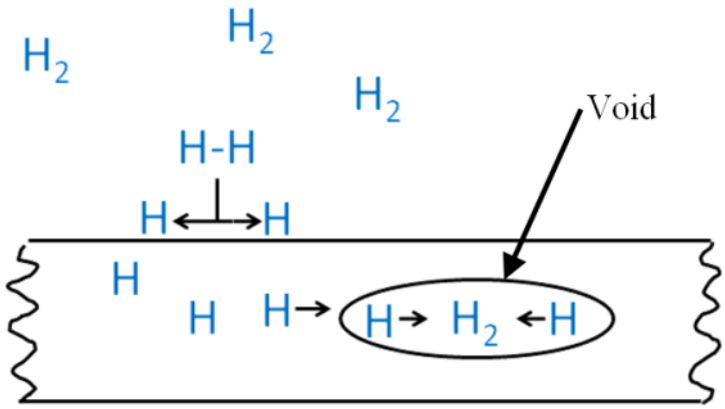

Figure 2: Mechanism of hydrogen blistering[10]

1.2.3. Hydrogen Attack

Once hydrogen has been absorbed into the matrix of a host material it can sometimes interact with alloying or impurity elements in what is called hydrogen attack. The hydrogen can chemically react to form an insoluble gaseous phase with elements in the host material[9]. This gaseous phase can sometimes produce steam when the hydrogen interacts with oxides, as in the case of some copper alloys, or it can form methane, as in the case of carbon steels[9]. The hydrogen tends to collect and interact with elements at grain boundaries. As the amount of the insoluble hydrogen product increases, the resulting pressure tends to push the grains apart, creating grain boundary fracture[9]. Such interactions tend to only occur at elevated temperatures; however, hydrogen attack is a large problem, especially for steels in the petroleum industry[9]. When steel with absorbed hydrogen is exposed to high temperatures the hydrogen will react with alloying carbon to produce methane in what is called decarburization. Nelson Curves produced by the American Petroleum Institute can help designers avoid

hydrogen attack by plotting safe operating rangers in terms of hydrogen partial pressures and temperatures.

1.2.4. Hydrogen Induced Cracking

Hydrogen has been noted to cause cracking and premature failure in components that have been designed to withstand normal crack propagation[10, 18]. Due to its lower solubility in molten metals, hydrogen can be absorbed from the atmosphere into a part as it is being manufactured[8-9]. As this part cools the absorbed hydrogen becomes trapped and residual stress can be developed. Hydrogen that is trapped in voids or inclusions causes an internal pressure that can be relieved through volume expansion in the form of a propagating crack. In most metals when the hydrogen concentration exceeds the solubility limit, precipitates will be produced which will lead to crack growth. Hydrogen induced cracking has also been shown to be the result of the formation of hydrides within a material. Rare earth, alkaline rare earth, transition metals, zirconium, tantalum, and titanium have been seen to form hydrides with certain concentrations of hydrogen[8-9, 19]. When the amount of hydrogen in aluminum or steel specimens exceeds the solubility limit, hydrogen gas bubbles precipitate out and can cause cracking. In hydride forming metals, however, when the hydrogen solubility limit is exceeded hydrides precipitate out[9]. These hydrides are typically less dense and brittle which can cause reduced ductility and fatigue resistance[9]. The hydride formation can also produce internal stresses which will cause a fracture of the hydride itself. Hydrogen will then move to this new void and stresses will concentrate at the new crack tips. The increased hydrogen concentration will cause the formation of a hydride which will again fracture.

This process will repeat itself until the critical crack length is reached and the material fails[9].

1.2.5. Hydrogen Embrittlement

Unlike the three previously mentioned phenomenon, the term hydrogen embrittlement is reserved for when absorbed hydrogen causes a normally ductile material to fail in a brittle manner without the formation of a new phase such as hydrides of hydrogen gas bubbles[9]. In hydrogen blistering, the material around the absorbed hydrogen remains ductile and allows for yielding to occur and form a blister. Alternatively, hydrogen embrittlement refers to the case when the material will experience brittle fracture around the concentrated hydrogen location without the formation of a hydride or new phase. The true mechanisms of hydrogen embrittlement are far less understood and researchers have been trying to understand it for almost a century [20-23]. It has been shown that the susceptibility of steels to hydrogen embrittlement depends on both temperature and strain rate[9]. It is believed that absorbed hydrogen will collect at highly stressed regions within a material and cause an increase in the yield strength in that region, as well as a reduction in the bond strength between faces such as between two grains[9]. If the hydrogen concentration is enough to cause this interfacial strength to become less than the stress on the material it will fail at the boundary, creating a crack. The hydrogen will then form at the stress concentration crack tip and the process will repeat resulting in brittle failure. It is also understood that increasing the strength of a material will only cause the embrittlement process to occur

faster[9]. This has resulted in the use of low-strength alloys and a possible loss of performance for components used in hydrogen environments.

1.2.6. Hydrogen Induced Tribological Effects

The effects of hydrogen on the bulk mechanical properties of materials have attracted a lot of interest and much research has been conducted in this area. In contrast to the amount of knowledge in this area, very little published work has been seen on the effects hydrogen has on the tribological performance of materials. No work has been found on how the tribological performance of aluminum and titanium alloys change after being exposed to a hydrogen environment. Only one study has been found that examines the effects of high-pressure hydrogen on wear, however, the material in this study was a non-metallic unfilled polytetrafluoroethylene (PTFE)[24]. The study showed that material that came in contact to hydrogen gas at high pressures saw an affect on the specific wear rate of PTFE[24]. With this result it is possible that other materials could exhibit an effect on tribological performance due to hydrogen exposure. Therefore, it is extremely important that research be conducted on other more commonly used materials. Apart from the exposure to pure hydrogen gas, the effects of absorbed hydrogen on tribological properties has been studied in regards to absorption resulting from corrosive environments. Many studies have shown that hydrogen from an acidic solution has been able to absorb into the material and exhibit an effect on titanium alloys[18, 25-28]. It has also been shown that hydrogen ions from H_2SO_4 can penetrate mild steel and cause a change in the wear mechanisms[29]. Hydrogen has also been shown to absorb into a material from a biological environment and have effects on the strength mechanisms of

titanium alloys[30-31]. The effects of the corrosive wear on Ti-6Al-4V[32] and HSLA steel[33] in an acidic solution have been studied and it was found that unusually high wear loses were seen due to the evolution of hydrogen atoms, resulting in the embrittlement of the alloy. These results suggest that embrittlement of a material can result from hydrogen absorption associated with an acidic solution; however, the change in wear mechanisms resulting from absorbed hydrogen has not been widely studied.

1.3. Wear Mechanisms

As moving parts slide and interact the surfaces can affect each other and can cause them to wear and change shape. Wear can be defined as the change in the physical condition of a surface through the interaction of another. It can also be described as the mechanical removal of material from a surface as a result of physical contact[34]. Wear has been classified into six general types: abrasive, erosive, cavitation, adhesion, corrosive, and fatigue [35].Abrasive and adhesive wear will be discussed in this study. Abrasive wear occurs when a harder material scrapes or cuts through the surface of a softer material[35]. Figure 3 shows an example of how a hard surface can cut though and wear a softer surface, leaving distinct cutting grooves. When metals come in contact there is some degree of adhesion between their surfaces[35]. However, layers of oil, water, and oxide films often prevent the adhesion from becoming great enough to critically affect the performance of a component. As parts rub together these upper protective layers can be removed and more adhesion becomes present[35]. Adhesive wear should always be considered by designers because of its high wear rates and large

unstable friction coefficients[35]. Figure 4 shows how material adhesion can occur where material can attach and be removed as one part slides across another.

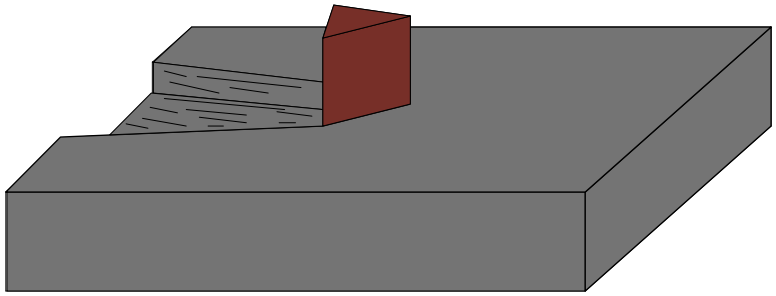

Figure 3: Cutting mode typical of abrasive wear

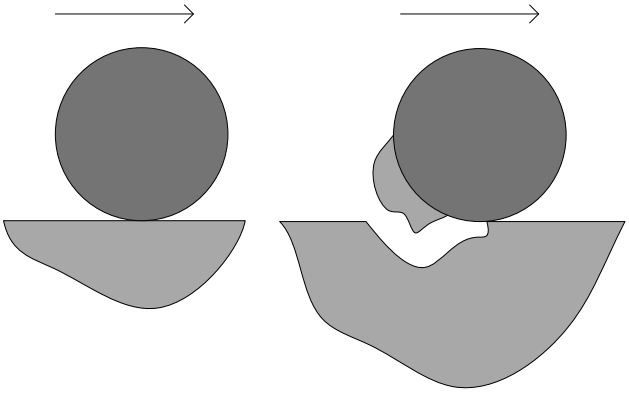

Figure 4: Adhesive wear mechanism showing material removal

1.4. Mechanical Testing

In evaluating the capabilities of different materials, researchers and designers rely on specific parameters in order to predict how materials will behave under certain conditions. In order to obtain these parameters, different testing techniques have been

devised and standards are set in place to ensure consentient and accurate mechanical testing methods[36]. Some of the mechanical testing methods include the Tension test, Hardness test, Charpy Impact test, and the Bend test. The Tension test can use flat or round specimens and is used to gain properties such as ultimate tensile strength and yield strength. ASTM standard A370-09A calls for an overall specimen length of 13mm for the flat geometry and 60mm for the round[36-37]. The Hardness test measures a material's resistance to penetration and can be used to obtain an estimate of tensile strength[38-40]. The limit to hardness testing is that the specimen being tested must be much greater than the indenter of the tester. The two most common hardness tests are the Brinell and Rockwell tests. The Brinell test uses a standard tungsten carbide ball which is 10mm in diameter[39]. The Rockwell test uses either diamond spheroconical or tungsten carbide balls, the smallest of which is 1.588 mm in diameter[40]. The Bend test is a test that is used to quantitatively characterize the ductility of materials and specimens are not to be less than 150mm[41-42]. The Charpy Impact Test strikes a notched specimen to measure the absorption of energy by the specimen, the shear fracture percentage, and the material movement on the other side of the notch [36, 43]. The test can be used to examine ductile and brittle behavior of materials in different conditions using specimens typically 40mm in length or larger[36, 43]. Schematic drawings of the different test specimen's geometries can be seen in Figure 5. As it can be seen, the amount of material volume needed for these tests can be relatively large and therefore cause the these test methods to be unusable in situations where only small

sample volumes are attainable. Such is the case when trying to charge specimens with hydrogen for testing.

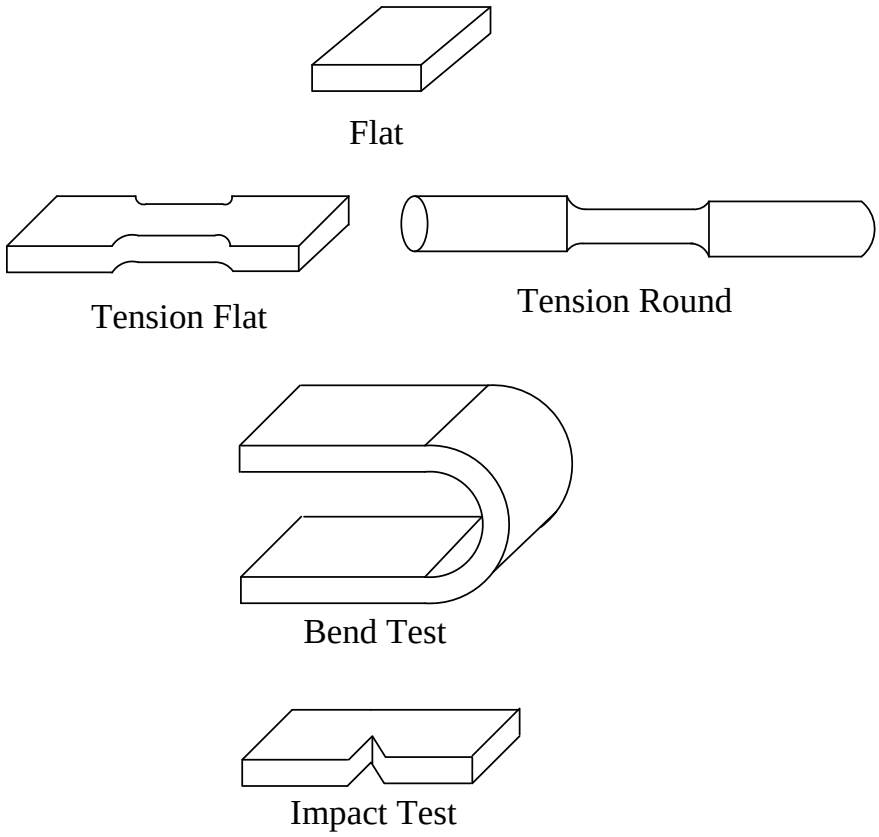

Figure 5: Common mechanical testing specimen geometries

1.4.1. Small Scale Mechanical Testing

The majority of standardized tests, involve relatively large specimen sizes thus rendering the test themselves destructive to the overall component being tested. The assessment of materials properties of a structure often require in situ evaluation of a particular component. Much work has been done to determine material properties using a specimen size that is as small as possible and even smaller than the methods mentioned above[44]. Miniature versions of the tension, hardness, bend, and impact tests have been

proposed. Many researchers have explored small specimen testing techniques in recent years[45-47]. One of the most promising techniques has been called the Small Punch Test (SPT) [48]. Compared to other larger scale types of mechanical testing, the SPT can be considered non-destructive for most tested components because it uses such a small volume of specimen to test. The advantage the SPT method is its ability to obtain consistent evaluation of mechanical properties from small specimen volumes effectively. In comparing the SPT to other small scale testing techniques, the SPT is favorable due to its relatively simple geometry and overall design. The SPT has been shown to provide a reliable technique for determining some of the materials properties of specimens with relatively small volumes [48]. The samples are easy to manufacture and can be made from a variety of materials. The test, first proposed by Manahan in 1981 and patented in 1983[49], used specimens similar in size to disks used for Transmission Electron Microscopy [50]. The 0.25-mm thick and 3-mm diameter disks were used to determine the mechanical properties of post-irradiated steels. The test was studied and further developed by Mao [51-52]. Foulds used the SPT to determine the fracture toughness of steels[53]. Brookfield was able to conclude that the calculated yield stress obtained from the SPT was not largely influenced by experimental error and that it could be used as a small specimen testing technique for steels [54]. Fouls studied how to obtain the ductile to brittle transition temperature using the SPT. The SPT has been used to evaluate the mechanical properties of ultra-high molecular weight polyethylene (UHMWPE), total joint replacement bone cement made of polymethylmethacrylate (PMMA) that has been used to anchor implants to underlying bone, and turbine rotors [55-57]. Due to the SPT's

ability to present and therefore analyze the mechanical properties of very small specimens, many local effects can be studied. The test can be used to examine the effects of coatings and surface properties of materials. One such example is using the SPT to examine the change in strength due to the heat affected zone for weld joints [58]. The results obtained from the SPT have been evaluated using finite element analysis(FEA) for many steel specimens[53-54, 59-60]. The experimental data and the FEA have been shown to be in good agreement [54]. Only a few studies have been done to show a connection between SPT parameters and the uniaxial tensile test parameters ultimate tensile and yield strength and of these studies only steel specimens have been used[48, 54, 61]. Of these tests Mao and Takahashi were able to find a relation between localized plastic straining load, P_y in Newtons and yield strength, σ_y in N/m. This relation can be seen in Equation 1 where t is the thickness of the specimen in meters[51].

$$\sigma_y = \frac{360P_y}{t} \tag{1}$$

They were also able to obtain a relation to the ultimate tensile strength, σ_{uts} and the maximum force of the SPT, $P_{max.}$ Which can be seen in Equation 2.

$$\sigma_{uts} = \frac{130P_{max}}{t} - 320 \tag{2}$$

The main issue with these relations is that no definite definition of the parameter P_y has been given. To try and help this problem, Brookefield was able to find a relation between the yield strength and the maximum force from the SPT which is more easily obtainable. This relation can be seen in Equation 3.

$$\sigma_y = \frac{P_{max}}{2.53x10^{-6}} + 49.2 \qquad (3)$$

This presented a better way to obtain the yield strength from SPT parameters however, one again only steel specimens were used to gain this relation.

More recently Milicka and Dobes were able to obtain a relationship using 8mm diameter chromium steel specimens. Their equation connecting the maximum punch force and ultimate tensile strength can be seen in Equation 4 where R_m is the ultimate tensile strength in N/mm and t is specimen thickness in mm.

$$R_m = \frac{F_{max}}{5.01t + 1.8t^2} \qquad (4)$$

Many studies have been done using the SPT technique, however, the technique has not been widely applied to aluminum and titanium alloys, although some mechanical behaviors of 6061 aluminum have been reported [62-63].

As a summary, this chapter discussed various aspects of energy, effects of hydrogen on materials, and the small punch test method. It is clear that the demand for energy requires a thorough understanding of materials behavior in hydrogen environments. It has been shown that there have been many attempts to find correlations between the SPT and uniaxial tensile test properties. However, all of these techniques have only considered steel in their formulations. The remaining thesis will focus on the effectiveness of surface and bulk mechanical characterization of materials in a hydrogen environment.

CHAPTER II

MOTIVATION AND OBJECTIVES

The extraordinary need for energy has pushed the development for newer and better energy technologies. Of these technologies, hydrogen has played a central role due to its use in hydrogen cars and hydrogen compressors, despite the somewhat unpredictable phenomenon it has on metallic materials. As discussed in Chapter I, the need to understand the interactions of hydrogen atoms in materials is not just crucial for new technologies, like hydrogen cars, but also for many current applications such as sour well operations, acidic storage, and many acidic cleaning processes. The interactions between steels and hydrogen have been studied however, there are great needs to explore the effects of hydrogen on aluminum and titanium alloys. To date, there is limited report in the mentioned area. The ability to physically and effectively test materials exposed to hydrogen is extremely important and currently insufficient. The Small Punch Test (SPT) has presented itself as a useful testing technique which could be applied in hydrogen testing. Yet the understanding of the test is limited and it has never been applied to hydrogen testing of aluminum and titanium alloys. The present research has three major objectives:

1. Gain a greater understanding of the SPT and further the connection between it and the standardized uniaxial tension test
2. Extend the usefulness of the SPT by developing a relationship between the bulk properties and the surface wear properties of tribological testing

3. Apply the SPT to hydrogen embrittlement testing and show the effects of hydrogen on the bulk mechanical and surface tribological properties of aluminum and titanium alloys

In gaining a greater understanding of the SPT, it is critical to also report on the repeatability of the method in testing aluminum and titanium alloys. If the test proves repeatable and a connection can be made to a typical tension test and tribological testing the ability to gain knowledge about the mechanical properties of small specimens will be greatly enhanced. With this understanding, links can be made from the bulk mechanical properties of the SPT to the surface tribological properties from tribological testing. Using this knowledge, a greater understanding of the effects of hydrogen can be added to a field in which there is little knowledge currently.

In order to meet those objectives, experimental approaches will be conducted. First, the repeatability of the SPT will be evaluated. The combination between Small Punch and tribological testing will provide a detailed study from surface to bulk in terms of mechanical properties. The effects of surface roughness on material behaviors will be studied. In addition, the influence of hydrogen on mechanical properties and the tribological performance of aluminum and titanium alloys will be conducted. Surface characterization will be carried out in order to understand the property-performance of tested metals. It is by this process that a small scale mechanical testing method will be developed and enhanced to prove more useful in the study of the effects of atomic hydrogen produced through chemical reactions on the behavior of metals.

CHAPTER III

EXPERIMENTAL

This chapter discusses the materials and experimental procedures used to investigate the mechanical and wear properties of different aluminum and titanium alloys. The chapter starts with a basic introduction to the materials tested including their composition and basic properties. This is followed by procedures involved in conducting Small Punch Tests (SPT) as well as triboligical testing. The technique used to charge specimens with hydrogen will also be discussed, as well as the chemical and imaging techniques that were used to characterize the effects of charging and testing.

3.1. Materials

Aluminum and titanium alloys were chosen for this study. Both materials have high strength to weight ratio, formability, and high corrosion resistance[64-65]. Aluminum alloys are extensively used for many different types of applications. The 3xxx series aluminum alloys are noted for their excellent formability and corrosion resistance properties. The series is also strain hardenable, has a high heat transfer rate, and good joinability properties such as welding. The 3003-H14 aluminum alloy is widely used in chemical handling equipment and cooking utensils [65]. The 2xxx series alloys are noted for their high strength, high toughness, and heat treatability. The series has more of an impurity of copper compared to the 3xxx series and thus gains its higher strength from precipitate hardening. The 2xxx series alloys are used for many aircraft and transportation applications. The 3xxx series aluminum alloys typically have more manganese then the 2xxx series alloys and they can also have a lower strength. Titanium

alloys are used in many applications, from heat exchangers to aircraft parts, due to their good corrosion resistance and strength to weight ratio[19, 66]. Titanium alloys exhibit good corrosion resistance due to their ability to easily passivate[67]. Titanium grade 5, or Ti-6Al-4V, is the most widely commercially used and produced titanium alloy and its production is responsible for almost half of the total weight of all titanium alloys produced[68]. Not only does the alloy have high strength and toughness it also has good workability and corrosion resistance. This alloy is also heat treatable. This combination of properties has made Ti-6Al-4V one of the most favorable titanium alloys for designers. The applications of Ti-6Al-4V include gas turbine engines, aerospace materials, pressure vessels, aircraft turbines, compressor blades, and surgical implants[68]. The Ti-6Al-4V alloy was used for this study because of its comparable mechanical properties with aluminum alloys. The chemical composition of each alloy is listed in Table 1 and Table 2.

Table 1: ASTM B209 chemical compositions of the aluminum alloys[69-70]

Alloy	Silicon	Iron	Copper	Manganese	Zinc	Titanium	Nickle	Other Elements		Aluminum
								Each	Total	
3003	0.6	0.7	0.05-0.20	1.0-1.5	0.10	…	…	0.05	0.15	remainder
2618	0.10-0.25	0.9-1.3	1.9-2.7	1.3-1.8	0.10	0.05	0.90-1.2	0.05	0.15	remainder

Table 2: Chemical compositions of Ti-6Al-4V[71]

Nitrogen, Max	Carbon, Max	Hydrogen, Max	Iron, max	Oxygen, max	Aluminum	Vanadium	Titanium
0.05	0.08	0.015	0.4	0.2	5.5-6.75	3.5-4.5	balance

The tensile strength, yield strength, hardness, and modulus of elasticity for each of the materials tested can be seen in Table 3. It shows that the 3003-H14 aluminum represents a low strength alloy while the 2618-T61 aluminum and Ti-6Al-4V are high strength alloys. The three materials represent a good range of strength.

Table 3: Material properties from literature [65, 69-71]

Material	Tensile Strength [MPa]	Yield Stength [MPa]	Modulus of elasticty [GPa]	Brinell Hardness
3003-H14	150	145	68	40
2618-T61	440	370	74	131
Ti-6Al-4V	900	830	113	369

3.2. Sample Preparation

Small disks of 3-mm diameter and 0.5-mm thickness were used for the SPT. The shape and dimensions of the specimens are shown in Figure 6. The 3003-H14 specimens were cut from a 0.5-mm thick sheet of aluminum using a water jet cutter. The sheet of aluminum was milled, unpolished, and meet ASTM B209-07. The 2618-T61 aluminum and Ti-6Al-4V alloys were cut from stock bar in a dielectric fluid environment using a Mitsubishi FX10 wire electrical discharge machine (WEDM). Rods of 3-mm diameter were cut from the stock bar and then 0.5-mm thick slices were made to produce the specimen disks.

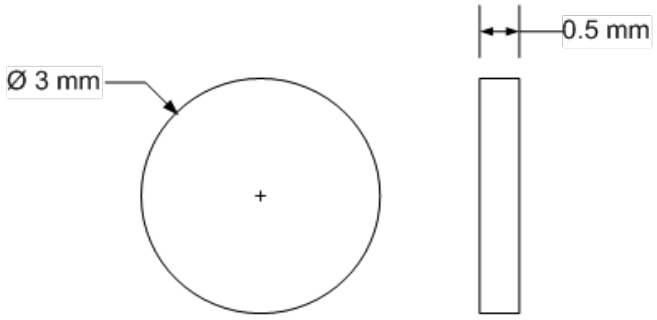

Figure 6: Dimensions of the small punch test specimens

Table 4 lists each of the alloys raw material standard, thickness tolerance, and heat treatment.

Table 4: Material specifications prior to specimen preparation

Material	Standard	Heat Treatment	Thickness tolarance [mm]
3003-H14	B0209-07	H14 temper 1/2 hard	±0.0381
2618-T61	AMS4132	T61	N/A
Ti-6Al-4V	AMS4928	Annealed	N/A

3.2.1. Hydrogen Charging

In order to expose specimens to hydrogen, the specimens were placed in a solution of 5-grams zinc powder and 7-mL of 50%vol water diluted sulfuric acid for 48 hours at room temperature prior to small punch testing. The specimens were removed from the solution and immediately tested. The chemical reaction between the zinc powder and the sulfuric acid can be seen in Equation 5. This equation shows that the zinc will react with the sulfuric acid to produce hydrogen gas. These hydrogen

molecules will then participate in the mechanisms of hydrogen transport as mentioned in the introduction.

$$Zn + H_2SO_4 = ZnSO_4 + H_2 \quad (5)$$

Apart from the reaction between the zinc and sulfuric acid, a cathodic reaction will also occur between the acid and the specimens themselves. When a surface of the metallic samples comes in contact with the sulfuric acid the electrochemical oxidation and reduction of electrons will result in nascent hydrogen at the surface. This process occurring at the surface of the specimens during charging can be seen in Figure 7. It is these hydrogen atoms that are very likely to be dissolved into the matrix of the specimens.

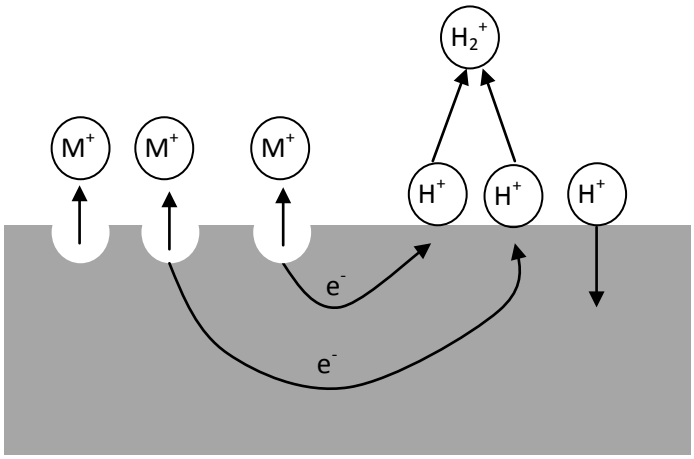

Figure 7: Cathodic reaction occurring at the surface of the specimens during charging[10]

This is a common reaction in acidic corrosion where metallic atoms on the surface will lose electrons and oxidation or metal deposition will take place to produce an ion. The loose electron will participate in hydrogen evolution to produce hydrogen molecules from the hydrogen in the sulfuric acid [10].

3.3. Small Punch Test

Once specimens are ready for testing, they underwent the procedure that will be presented in the following. This section will also discuss the procedure for testing the effects of surface roughness, as well as the new small punch block test which has never been done before.

3.3.1. Procedure

The 3-mm diameter and 0.5-mm thick disks were tested using the SPT method. To hold the specimens during small punch testing, a test jig was machined from annealed A11 tool steel and then tempered and hardened to HRC 55. The dimensions of the jig are shown in Figure 8. The jig consists of a lower portion that holds the specimen and an upper portion that clamps the edges of the specimens down. To begin each test, a specimen was placed in the lower portion of the jig. Then, the upper and lower jigs were clamped together using clamping screws tight enough as to not deform the specimen. Before each test, the push rod was sprayed with a greaseless lubricant in order to minimize frictional interference and to create a consistent frictional force opposing the push rod. A 1-mm diameter steel ball bearing, placed at the end of the push rod, was pushed through each specimen at a constant speed of 0.0021-mm per second while the reaction force from the specimen was measured using a load cell. An Instron 4410 universal tension testing machine was used to create the displacement and measure the force via the load cell with an accuracy of ±0.5%. The force was recorded using a data acquisition system at a frequency of 10 Hz. The displacement of the ball bearing as it moved through the specimen was computed using the time of each load cell

measurement and an assumed constant crosshead speed. A force versus extension (FvE) curve can then be made showing how the material deforms under a centrally loaded force.

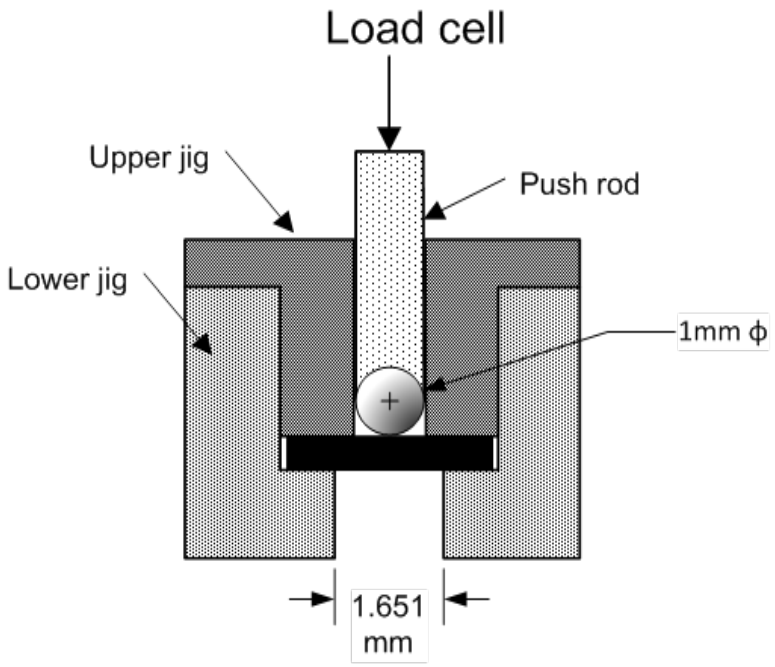

Figure 8: Cross-section of the small punch test jig showing dimensions

3.3.2. Roughness Measurement

Before and after small punch testing, morphological information was obtained using optical microscopy. Images of the specimen's surface were taken at various magnifications using a Keyence VHX-600 digital microscope with a Keyence VH-Z20 digital lens. The surface roughness of representative specimens was measured using a Qualitest TR1900 surface roughness machine. The average roughness for each alloy can be seen in Table 5.

Table 5: The average roughness for each alloy

Material	Average Roughness [μm]
3003-H14	0.488±0.0395
2618-T6	2.06±0.375
Ti-6Al-4V	1.67±0.0382

3.3.3. Small Punch Block Testing

In order to further evaluate the deformation behavior a specimen undergoes during testing, a small punch block test was conducted on the alloys. The same procedure as for the punch test was conducted except a specimen of Ti-6Al-4V was placed under the specimen being tested. This test eliminates the bending portion a specimen would normally undergo. The ball bearing was then pushed into the specimen as in a normal SPT. A cross-section of this test setup can be seen in Figure 9.

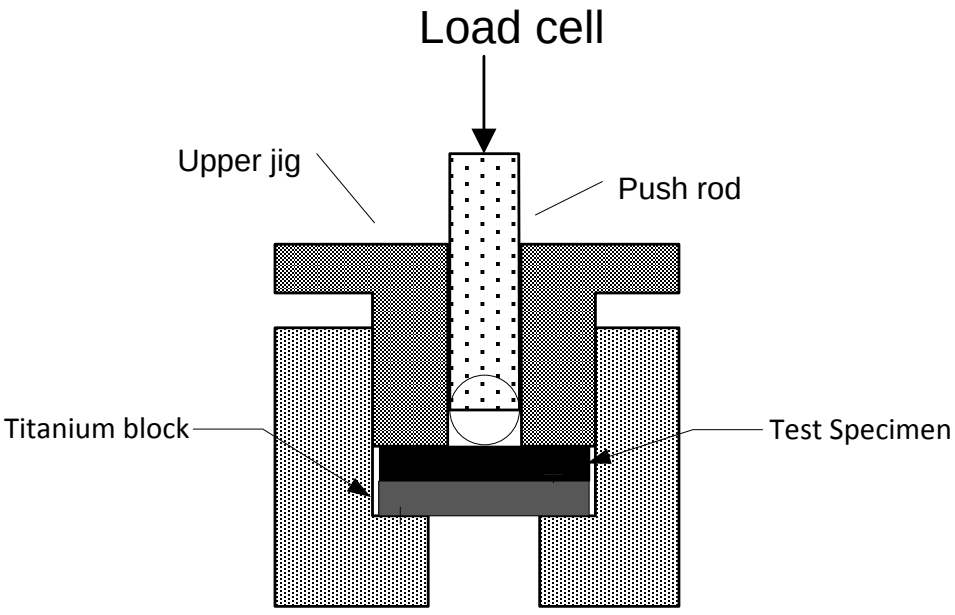

Figure 9: Cross-section of the block test setup

3.4. Tribological Analysis

In order to determine any changes in wear properties between specimens that were charged and uncharged, tribological testing was performed using a CSM-Instruments model number TRB Tribometer in a similar fashion to ASTM standard G99-05. A 6-mm 440 stainless steel ball bearing was used to create a 4-mm half-amplitude linear wear track at a speed of 2.50-cm/s. The wear track was 30 meters long for the 3003-H14 aluminum specimen and 20 meters long for the 2618-T61 and Ti-6Al-4V specimens. The normal load was 1 Newton for the 3003-H14 aluminum specimen, 2 Newtons for the 2618-T61 specimen, and 3 Newtons for the Ti-6Al-4V specimen. Both the charged and uncharged specimens were tested under the same conditions. Microscopic images of the wear track produced can be seen in Figure 31. In order to determine the wear volume removed a Qualitest TR1900 Surface Roughness machine was used to measure the dimensions of the volume removed in the wear track.

3.5. Characterization

In order to understand behavior of materials under mentioned tests, characterization was conducted to evaluate surface morphology and microstructure.

3.5.1. Optical Microscope

Before and after small punch testing, morphological information was obtained using optical microscopy. Images of the specimen's surface were taken at various magnifications using a Keyence VHX-600 digital microscope with a Keyence VH-Z20 digital lens. Reflected light was used for sample analysis.

3.5.2. Scanning Electron Microscope

The deformation and wear mechanisms were studied using high magnification and high resolution images obtained through Tescan VEGA-II LSH Scanning Electron Microscope. The SEM was operated at 20 kV with a working distance of 29.93mm at 200x and 400x magnification.

3.5.3. X-Ray Diffraction

Microstructures were analyzed using a XDL Bruker D-8 Bragg X-Ray Diffraction machine in order to determine the presence of hydrides. It was operated with a step of 0.030˚ and step time 38 seconds.

CHAPTER IV

RESULTS

This chapter will provide the experimental results obtained through procedures discussed in Chapter III. Firstly, results of the Small Punch Test (SPT) will be presented through evaluation of repeatability and materials. Next will be the study of the effects of surface roughness on material behavior. Finally, effects of hydrogen will then be studied through the SPT and tribotesting.

4.1. Repeatability

In order to evaluate the repeatability of the SPT, three tests of identical specimens were conducted for all of the materials tested. Force versus Extension (FvE) cures of the 3003-H14 aluminum alloy are shown in Figure 10. This figure shows the extension of the ball bearing into the material on the X-axis and the corresponding force, measured by the load cell, exerted by the material on the ball on the Y-axis. From these three plots an average and standard deviation can be plotted. The average and standard deviation for the curves seen in Figure 10 are plotted in Figure 11. Average and standard deviation curves for all of the tested materials will be shown later.

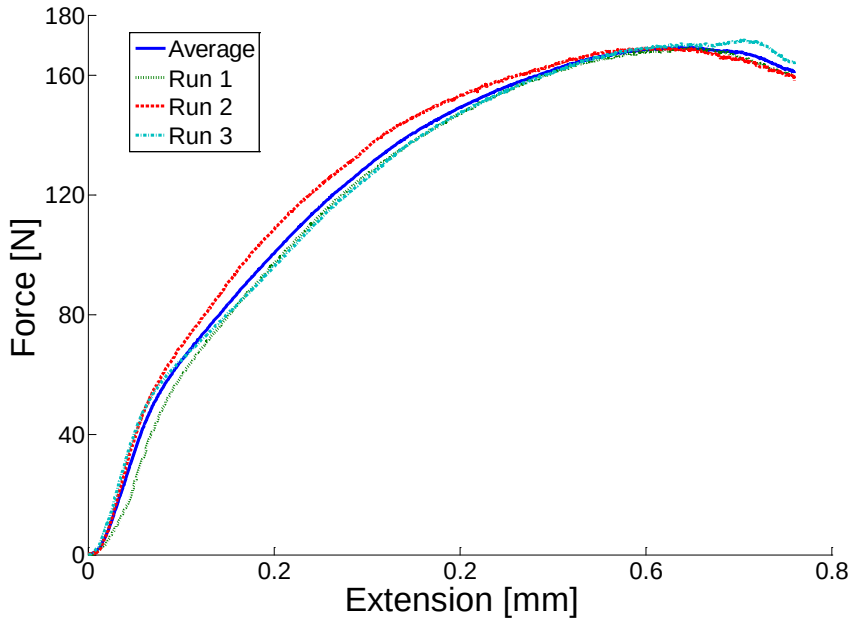

Figure 10: Force versus extension curve for three Al 3003 samples

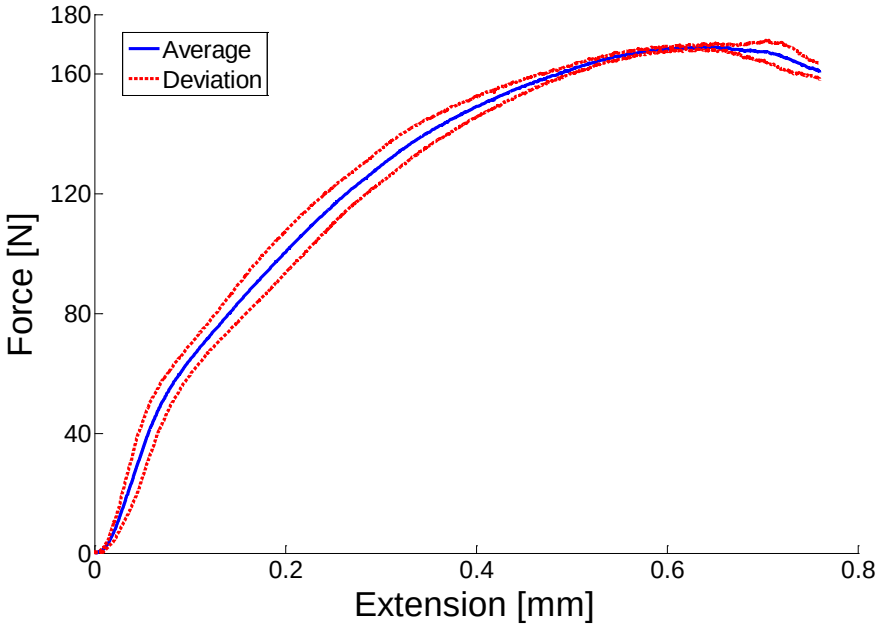

Figure 11: A plot of the average SPT test FvE curve showing its standard deviation for Al 3003

4.2. Effects of Surface Roughness

The effects of roughness on the FvE curve were evaluated through tests of specimens with different roughness. Table 6 lists the average roughness for each test run and its standard deviation.

Table 6: The average values of each run for the roughness test showing an average and standard deviation

	Run 1	Run 2	Run 3	Run 4
Roughness, Ra [μm]	2.56±0.451	0.813±0.083	0.577±0.0519	0.487±0.037

The FvE curves for each of the runs are shown in Figure 12. The X-axis is the extension of the ball bearing into the specimen. The data was adjusted to show an extension of zero when the ball just comes in contact with the surface of the specimen. The Y-axis is the force reacting from the surface of the specimen onto the ball bearing measured by the load cell. Over an average surface roughness range from 0.450 μm to 3.011 μm, the overall percent error[1] of the three runs was calculated to be 4.3%.

[1]See APPENDIX A

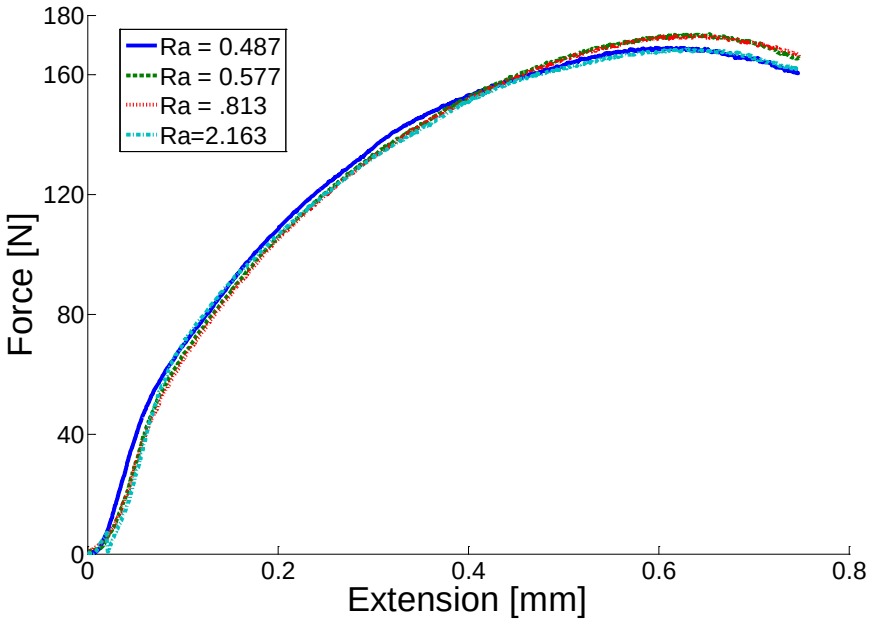

Figure 12: FvE curve for three 3003-H14 specimens of different surface roughness

Figure 13 shows an average of all the roughness tests and its one-sigma deviation at each value of extension.

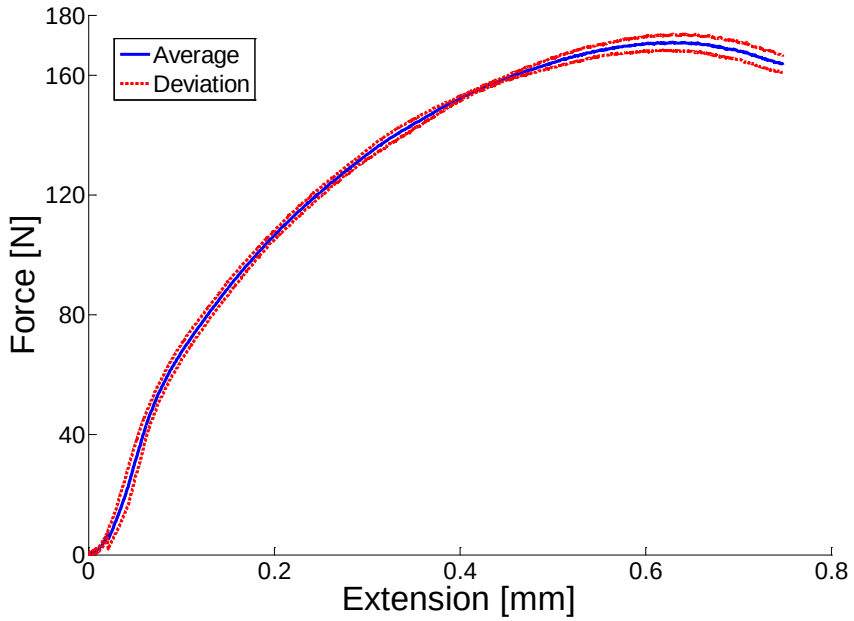

Figure 13: A plot of the average roughness test curve showing its standard deviation

4.3. Behavior of Materials

The FvE curves for the 3003-H14 aluminum, 2618-T61 aluminum , and Ti-6Al-4V specimens were compared and are shown in Figure 14. This figure shows that the Ti-6Al-4V specimens had the heighest maximmum force and that the 3003-H14 aluminum had the lowest maximum force. The 3003-H14 aluminum specimens' maximum force did occur at a larger extension than the other materials.

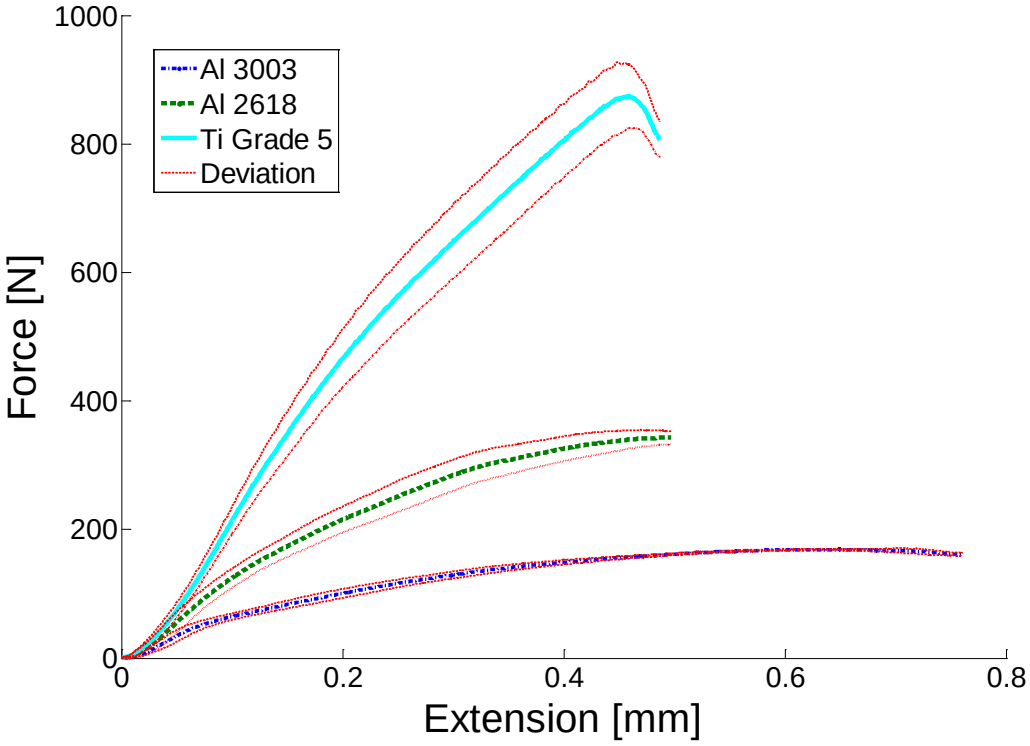

Figure 14: Average force vs. extension curve for the specimens tested showing the standard deviation for each

In order to evaluate the behavior of the materials during a SPT, a number of parameters were found from an average of all the SPT runs for each material. Table 7 lists the average overall percent error[1], the area under each average curve up to the maximum force, the average maximum force with one deviation, and the depth at the maximum force. The values for all of the FvE curves will lay within the deviation lines with a 99.5 % confidence.

Table 7: Results of the SPT

Material	Overall percent error [%]	Area under curve [J]	Average maximum force [N]	Dept at maximum force [mm]
3003-H14	6.13	0.0776	169.21±1.06	0.7082
2618-T61	14.24	0.1107	343.08±2.94	0.4949
Ti-6Al-4V	11.11	0.2216	874.52±12.80	0.4585

Digital microscopic images of a representative specimen for each material type were taken and can be seen in Figure 15. The punched side of a 3003-H14 aluminum specimen is shown in (*a*) and the back in (*b*). The punched side of a 2618-T61 aluminum specimen is shown in (*c*) and the back in (*d*). The punched side of a Ti-6Al-4V specimen is shown in (*e*) and the back in (*f*).

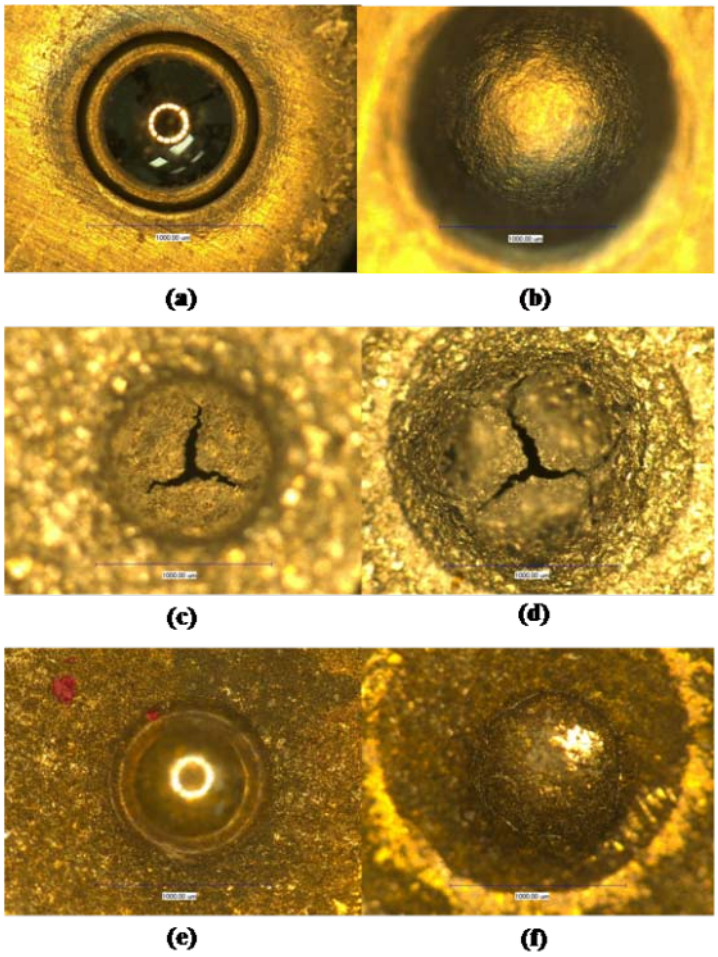

Figure 15: Pictures of specimens after testing. 3003-H14 aluminum- (a) top, (b) bottom, 2618-T61 aluminum- (c) top, (d) bottom, Ti-6Al-4V- (e) top, (f) bottom

4.3.1. Small Punch Block Testing

To eliminate the effect of buckling, block testing was conducted for all three materials and the results can be seen in Figure 16. The Block Test curve is taken as an average of three runs for each material. This figure shows that the Ti-6Al-4V has the

highest slope followed by 2618-T61 aluminum, and finally 3003-H14 aluminum with the smallest slope.

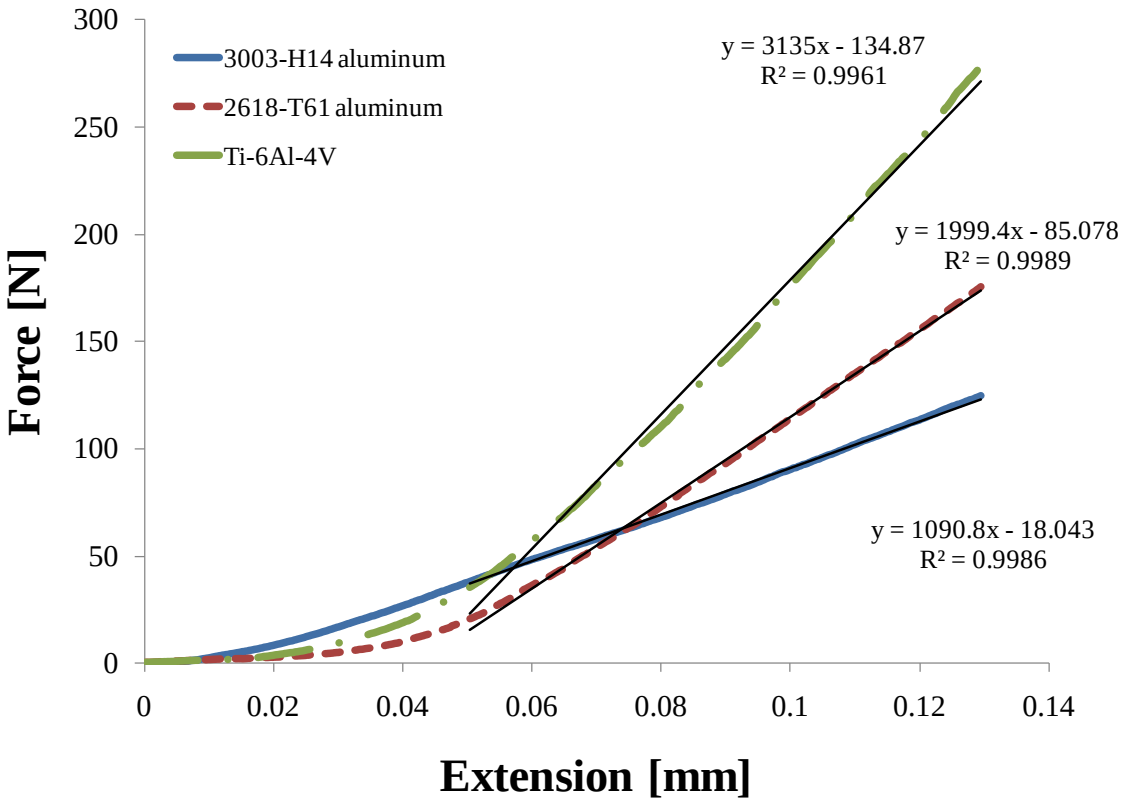

Figure 16: Comparison of the three block tests

Figure 17, Figure 18, and Figure 19 show how the results from the block test compare to a the average of three runs of a normal SPT for each of the materials. The point where the block test FvE curve deviates from the SPT curve is labeled as F_y.

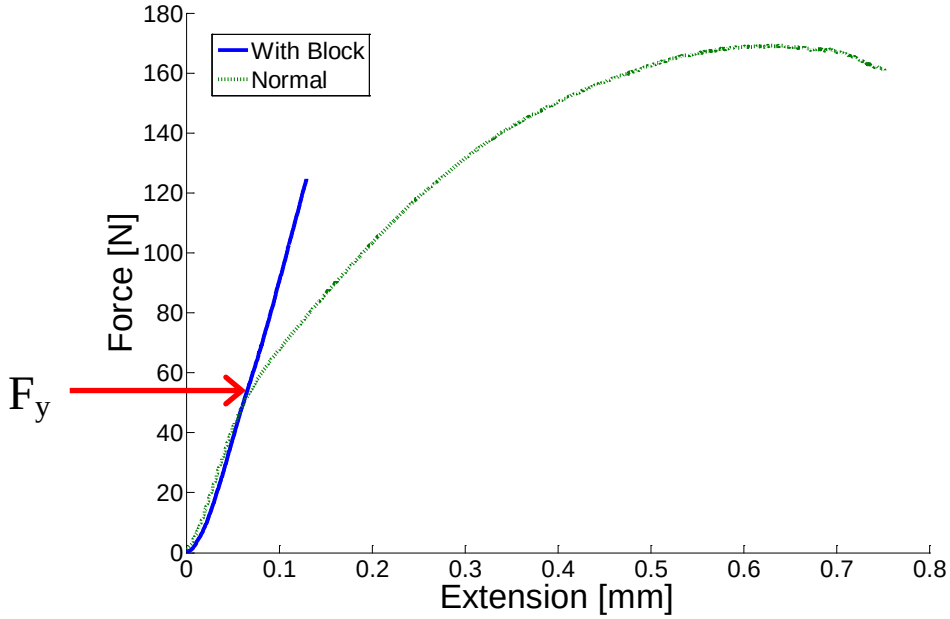

Figure 17: Plot showing the average of the block test results compared to the average of the normal test results for 3003-H14 aluminum

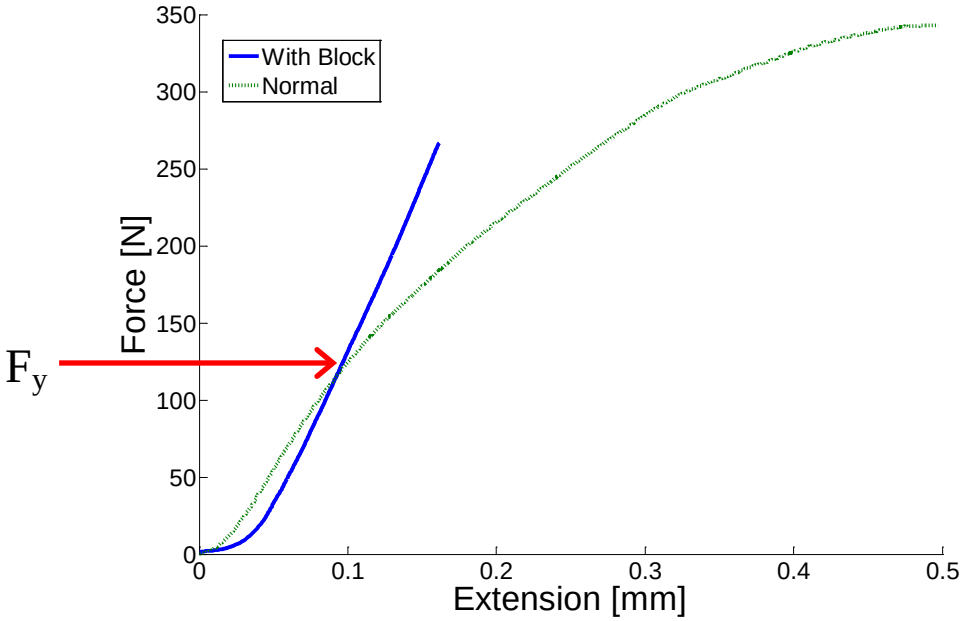

Figure 18: Plot showing the average of the block test results compared to the average of the normal test results for 2618-T61 aluminum

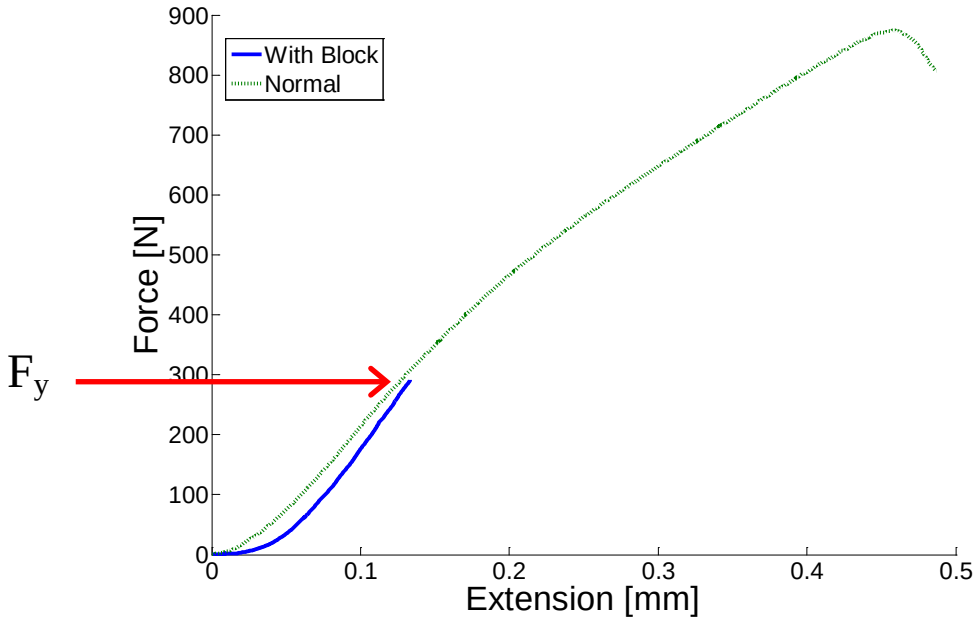

Figure 19: Plot showing the average of the block test results compared to the average of the normal test results for Ti-6Al-4V

4.3.2. Small Punch Testing of Charged Specimens

The FvE curves comparing charged and uncharged conditions for each of the materials are shown in Figures 20-22. The figures show the extension of the ball into each material on the Y-axis as a function of measured force on the X-axis. The FvE curves are plotted until a maximum force is reached. Figure 23 shows FvE curves for all of the materials tested at the same scale.

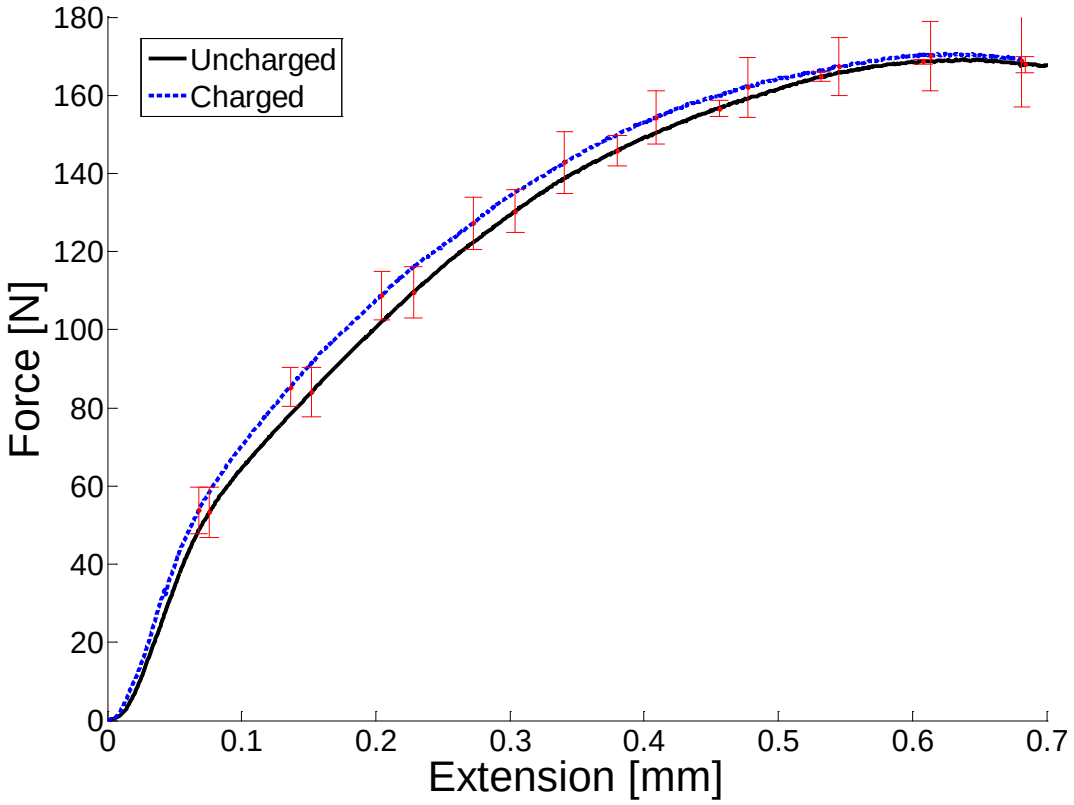

Figure 20: FvE curve for 3003-H14 aluminum under charged and uncharged conditions

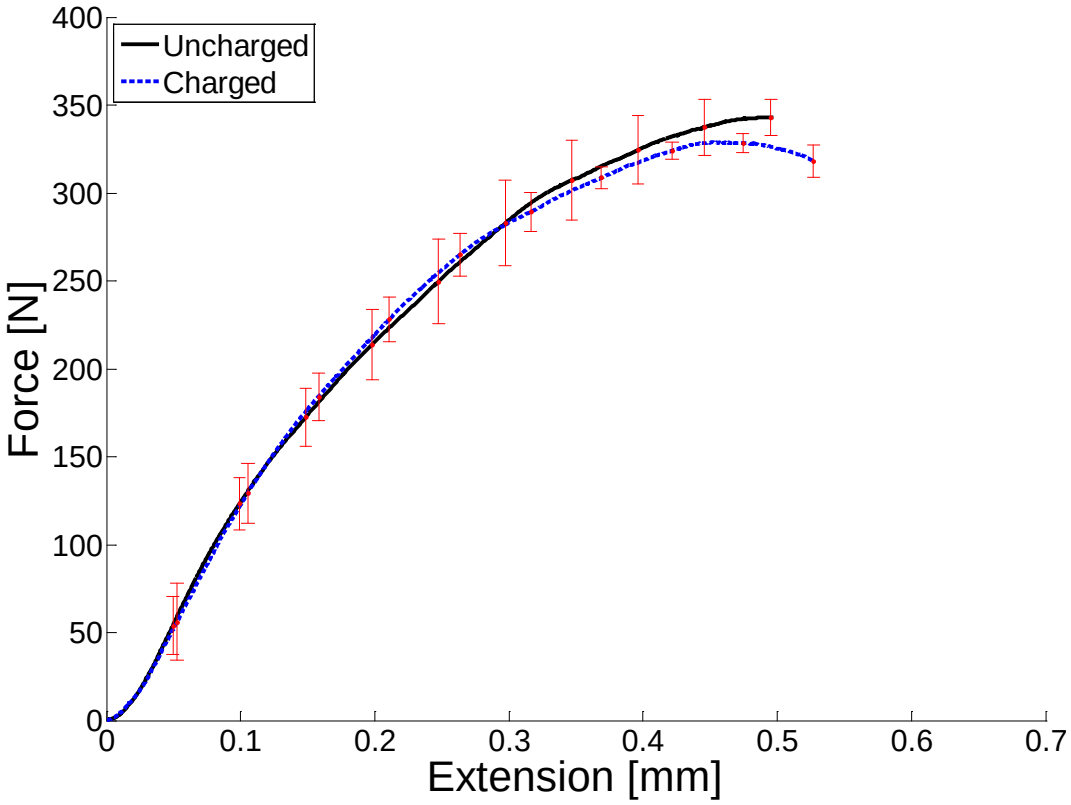

Figure 21: FvE curve for 2618-T61 aluminum under charged and uncharged conditions

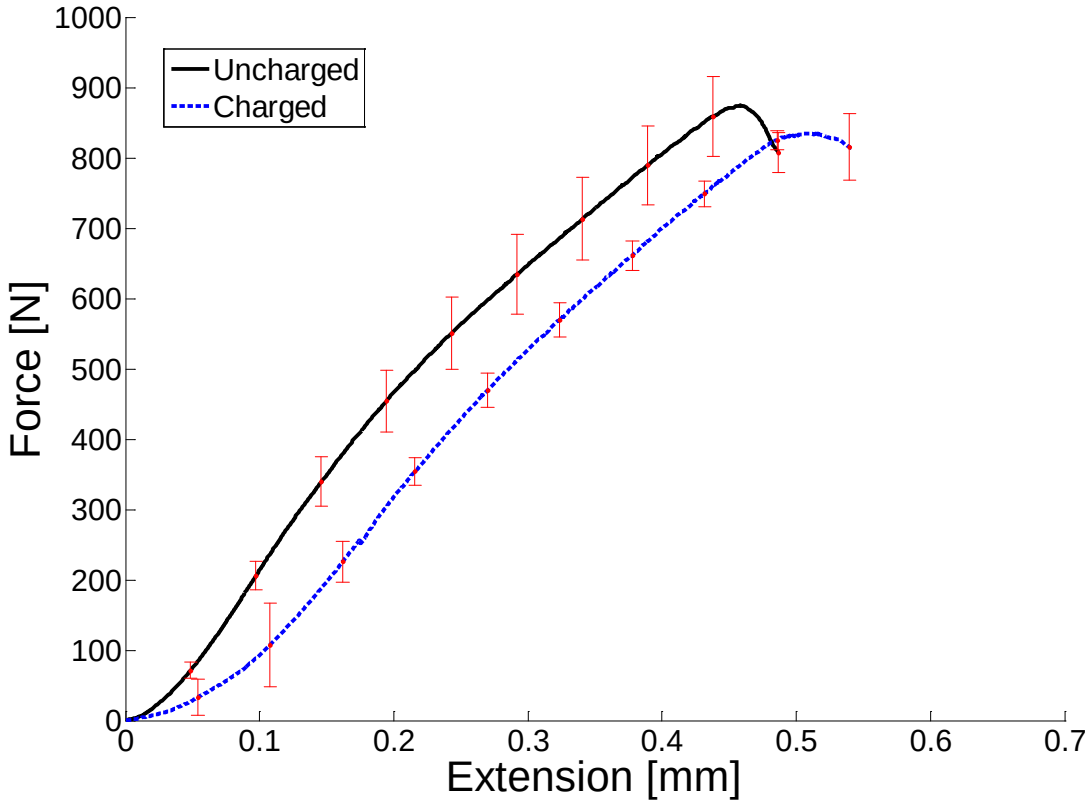

Figure 22: FvE curve for Ti-6Al-4V under charged and uncharged conditions

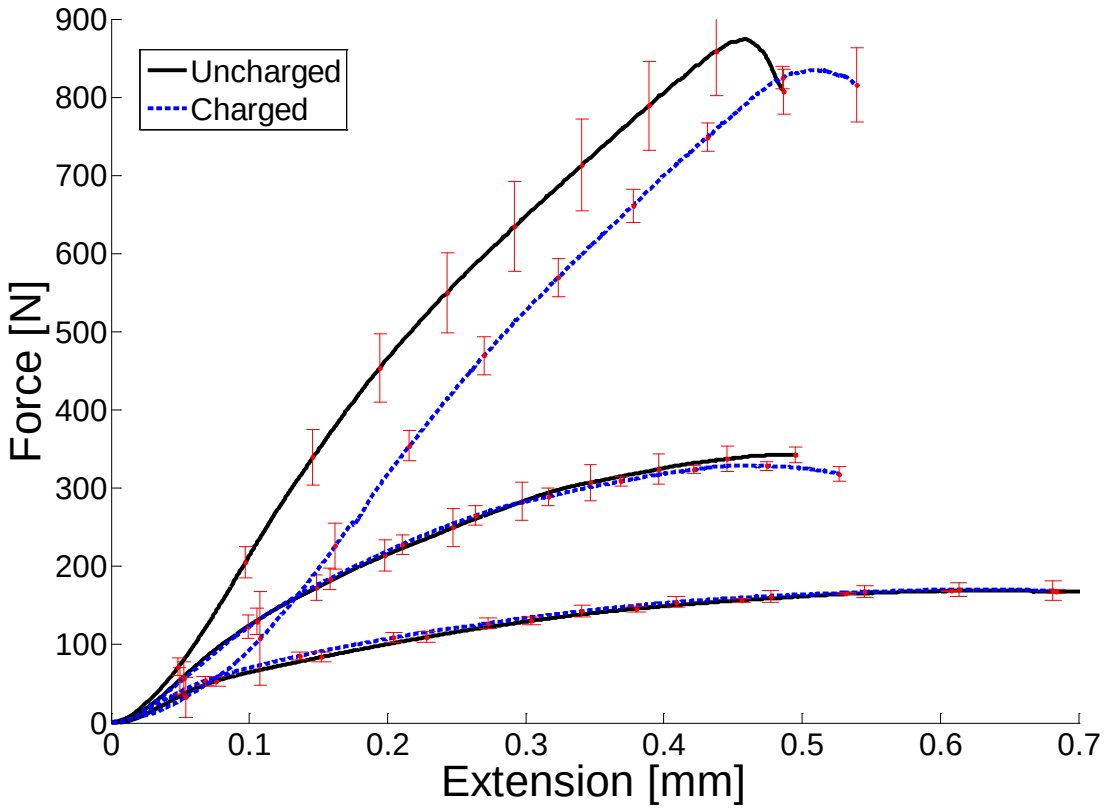

Figure 23: FvE curve for all materials tested showing charged and uncharged conditions

Results similar to Table 7 for uncharged specimens were tabulated for charged specimens and are shown in Table 8.

Table 8:Results of the SPT on charged specimens

Material	Overall percent error [%]	Area under curve [J]	Average maximum force [N]	Dept at maximum force [mm]
3003-H14	8.52	0.078	170.69±2.77	0.63
2618-T61	11.73	0.095	328.92±1.39	0.45
Ti-6Al-4V	20.01	0.213	834.78±9.57	0.59

Microscopic images of representative specimens were taken and are shown in Figure 24. The center part of each sample was deformed by the indenting ball. The images on the left are of a sample without charge as a reference and on the right, a sample that has been charged. There is no visible difference at this magnification due to hydrogen. The 3003-H14 aluminum in Figure 24(a-b) showed no cracks but rather more ductile stretching. The 2618-T61 in Figure 24 (c-d) presented a circumfrencial fractured surface opening up that is much larger than the cracks seen for the Ti-6Al-4V shown in (e-f).

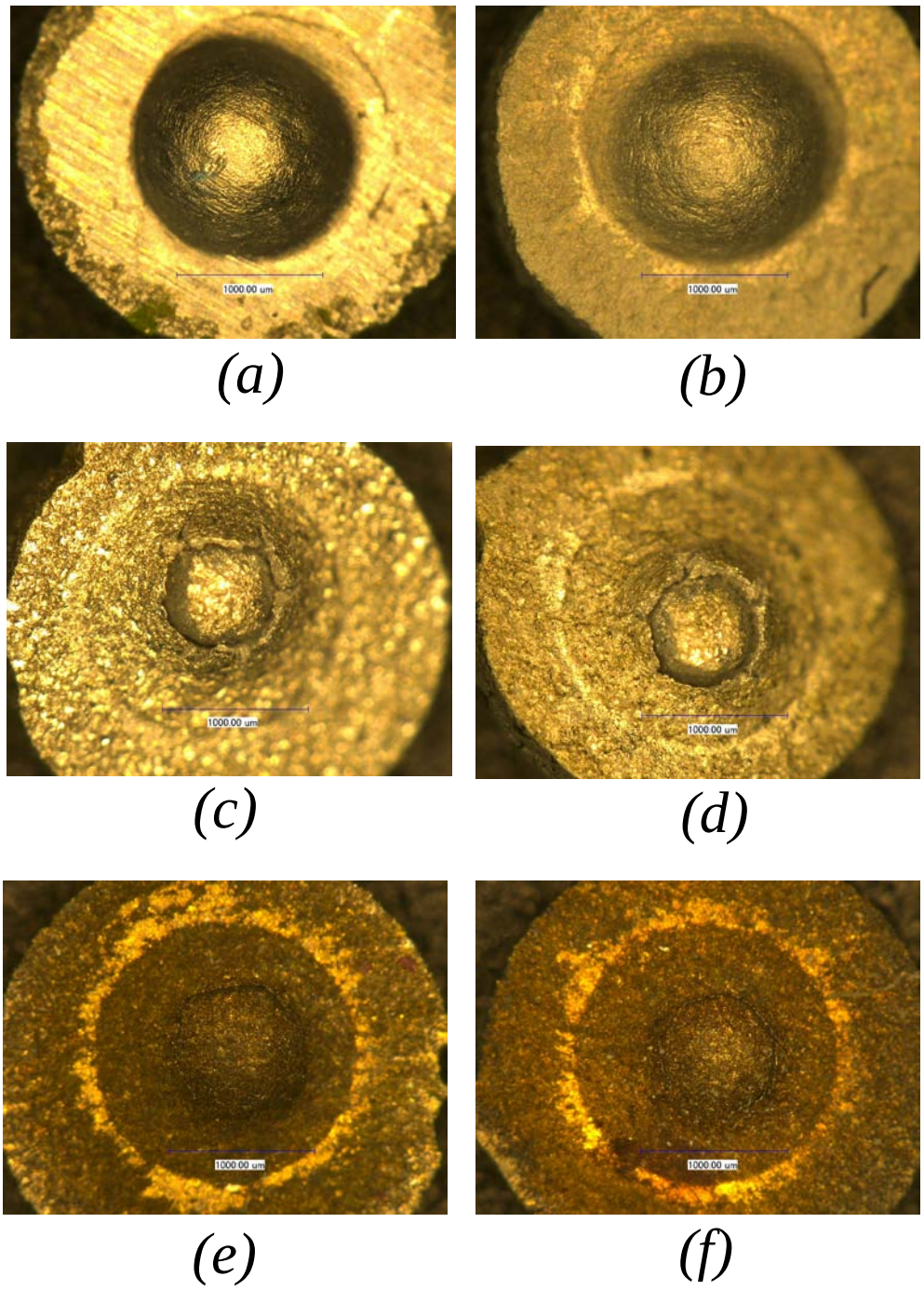

Figure 24: Pictures of backside of SPT specimens charged and uncharged. 3003-H14 aluminum - (*a*) uncharged, (*b*) charged, 2618-T61 aluminum - (*c*) uncharged, (*d*) charged, Ti-6Al-4V - (*e*) uncharged, (*f*) charged

The evolution of the mechanical behavior of the tested materials was conducted using a stop test method. The stop test was conducted by stopping a SPT intermittently while the ball was in contact with the specimen. Without changing the specimen, the ball was pushed into the material again each step slightly deeper. This sequence was repeated nine times for the 3003-H14 aluminum alloy and the FvE curves for all of the runs can be seen in Figure 25.

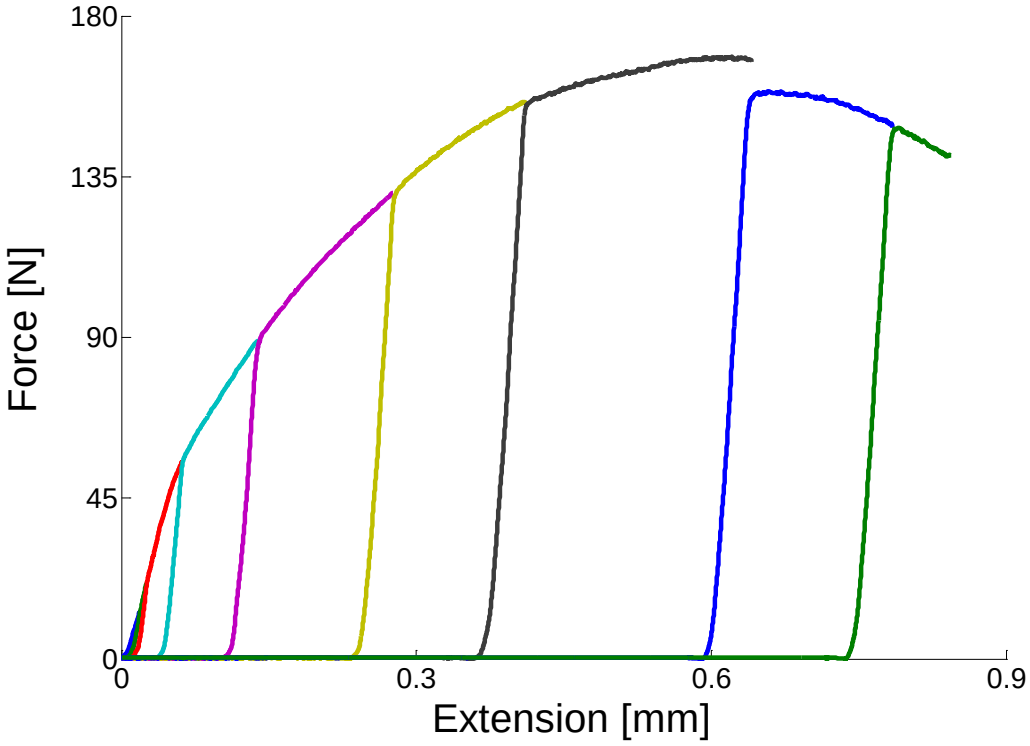

Figure 25: Stop test of 3003-H14 aluminum

A plot of the stop test runs for the 3003-H14 aluminum was compared to a normal SPT run and can be seen in Figure 26. The figure shows that the FvE curve for a normal SPT lines up with all of the runs of the SPT. After a few steps, the stop tests

showed a slight drop in strength in comparison with the normal test (Figure 26). Details will be discussed in the following chapter.

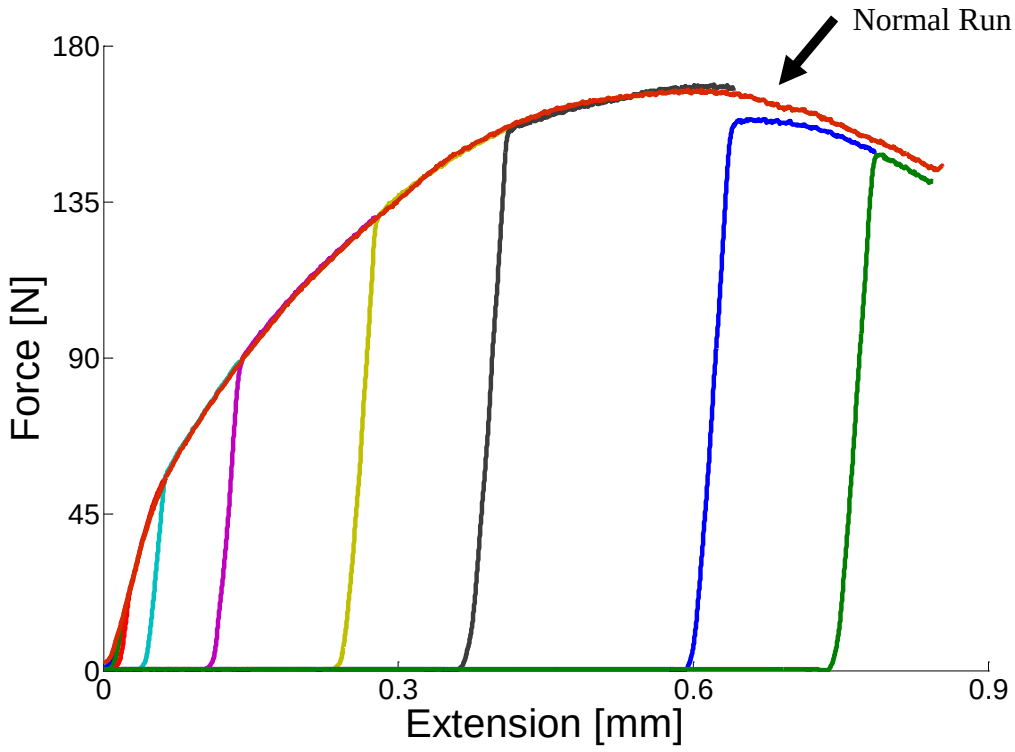

Figure 26: Stop test of 3003-H14 aluminum compared to a normal test run

4.4. Tribological Analysis

In order to gain an understanding of how the tribological properties of each of the three alloys were affected by the charging with hydrogen, the steady state coefficient of friction and wear removal rate were tested and the results are shown in the following sections.

4.4.1. Coefficient of Friction

The data of friction coefficient against time is plotted in Figure 27. Three tests were run for each material and the averages of the three were taken. The figure shows that the stabilized coefficient of friction for all materials is independent of charging condition.

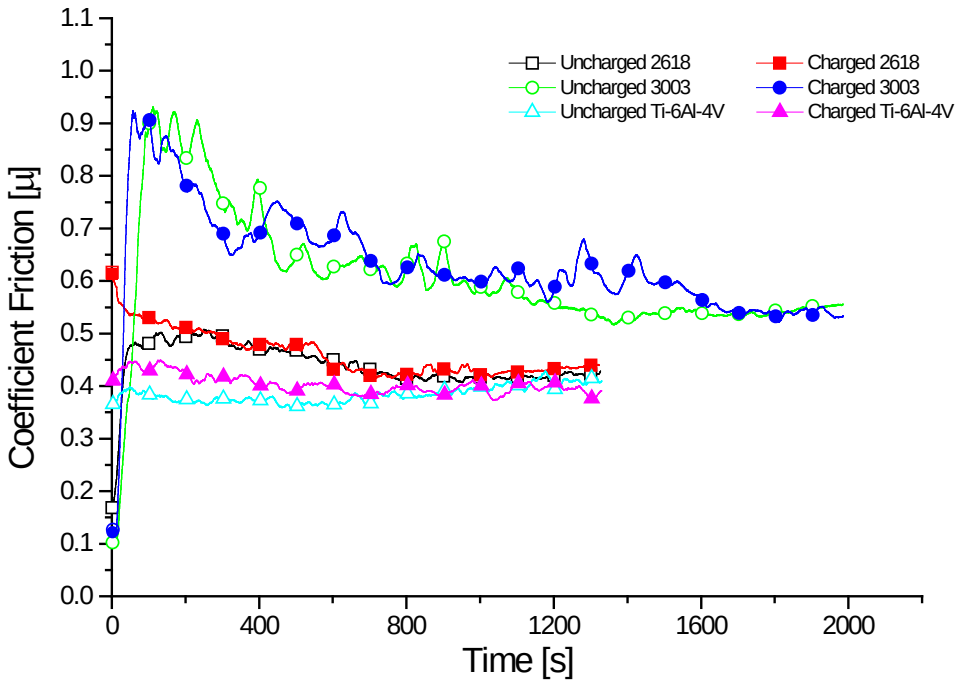

Figure 27: Friction coefficient versus time plot of all tested specimens

Figure 28 shows the steady state friction coefficient averages over three separate runs for each of the test conditions. The figure shows that there is statically no difference in the steady state friction coefficient between the charged and uncharged conditions.

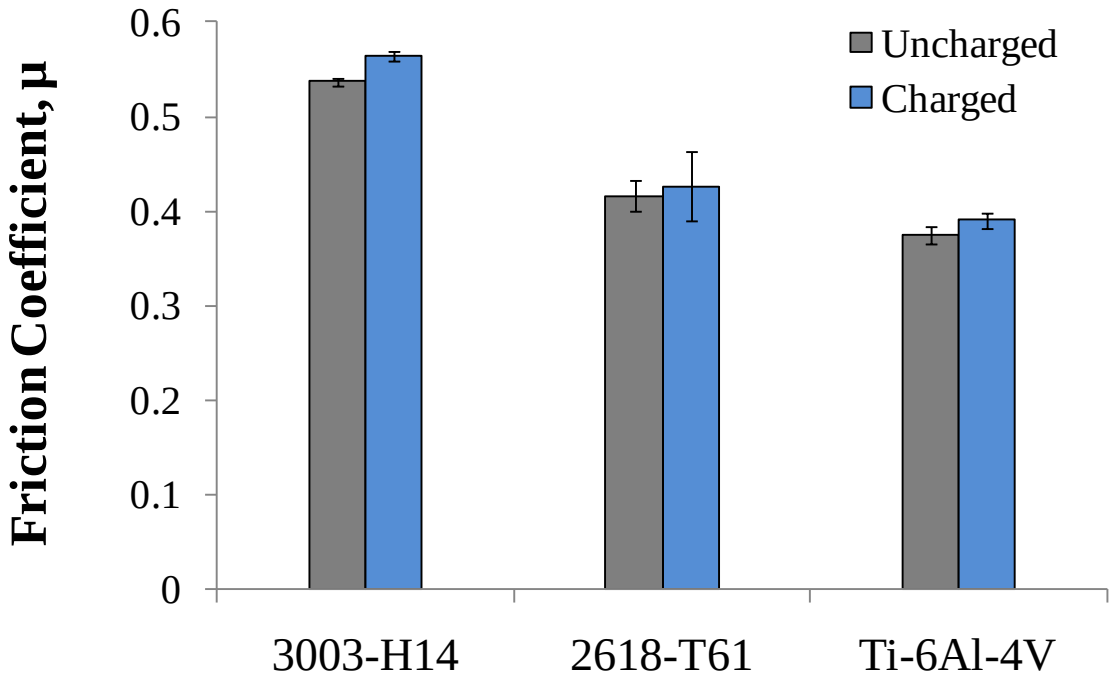

Figure 28: Non-transient friction coefficient for each alloy tested with a charged or uncharged condition showing one standard deviation error bars

4.4.2. Wear Volume

The wear volume was measured during tribolgical testing and is presented in Figure 29. This figure shows that wear is independent of charging condition.

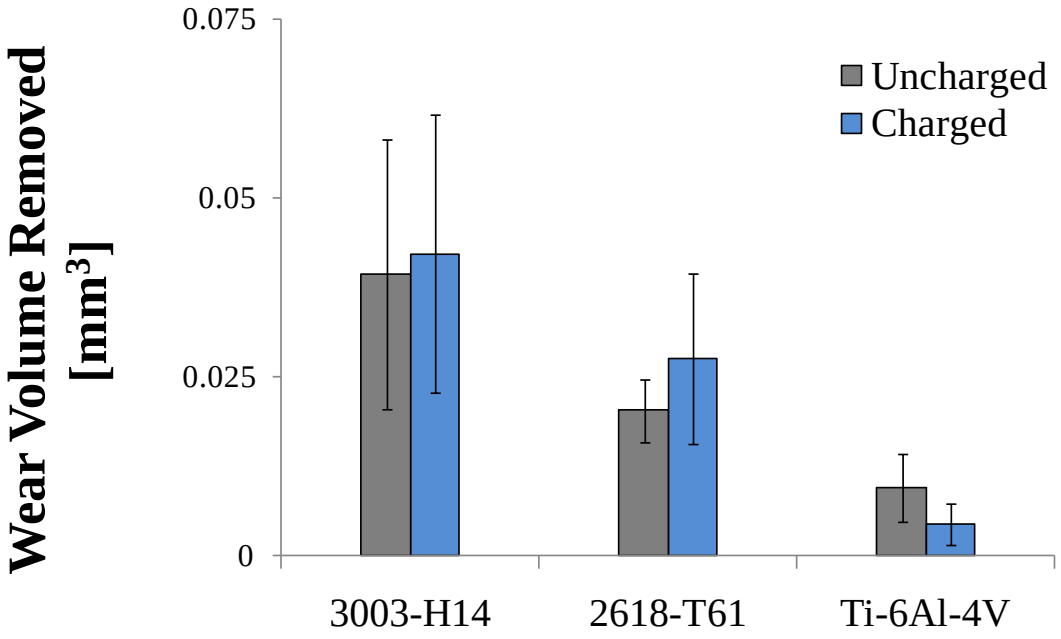

Figure 29: Amount of wear volume removed for each alloy tested with a charged or uncharged condition showing one standard deviation error bars

The data in Figure 29 can also be represented in terms of a wear rate. This representation can be seen in Figure 30.

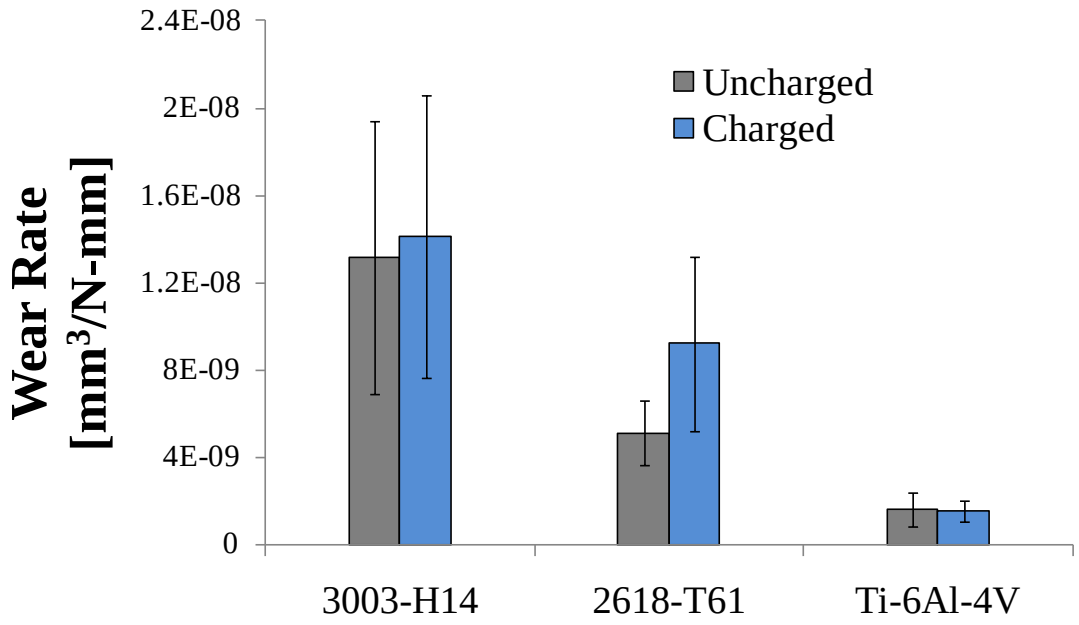

Figure 30: Wear rate for each alloy tested with a charged or uncharged condition showing one standard deviation error bars

The wear track for each condition at 100x can be seen in Figure 31. Highly magnified (500x) images of circled regions for each material are also shown. The images show that the wear mechanisms are similar for charged and uncharged specimens. The images show mostly abrasive wear, however some areas of adhesion are squared.

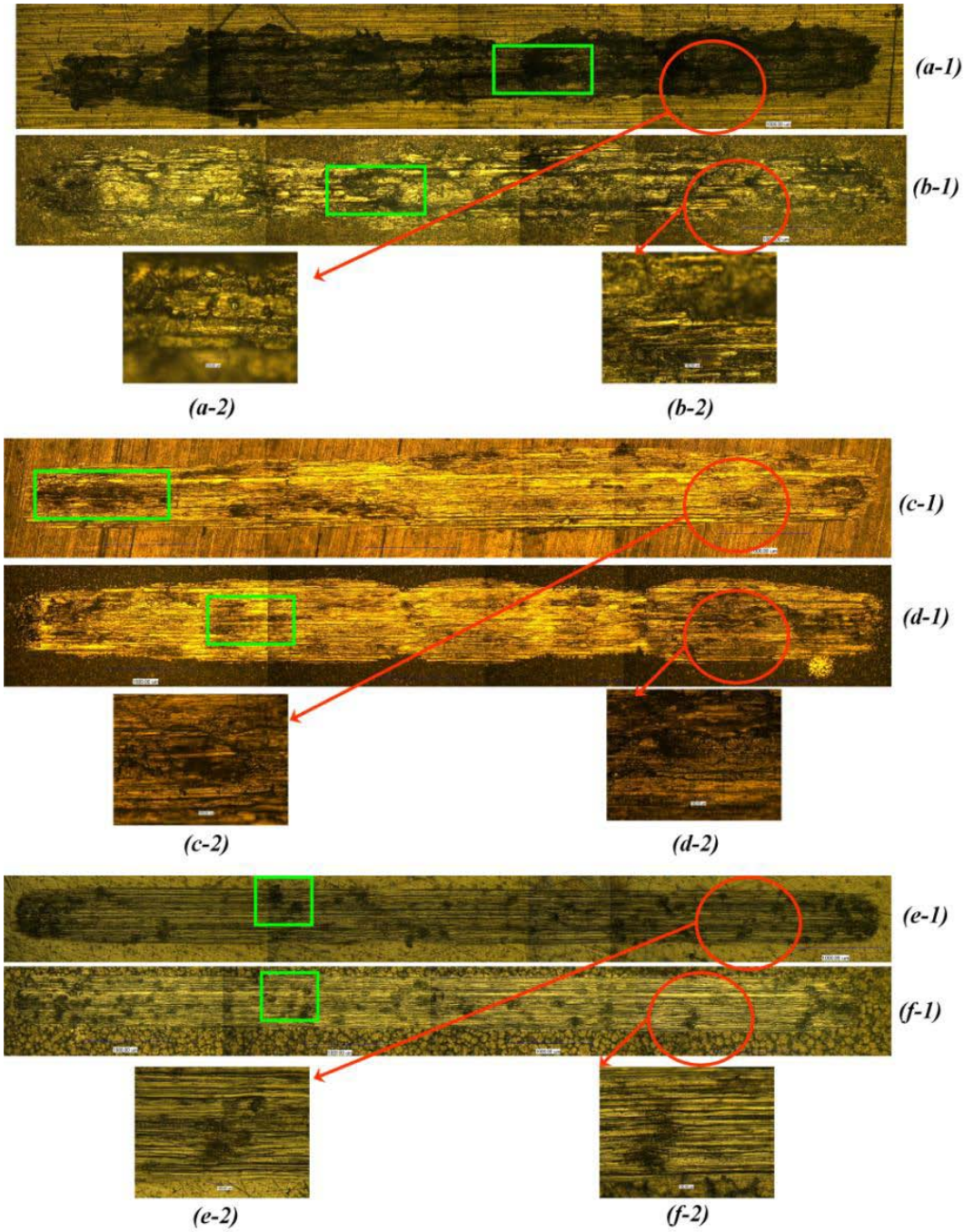

Figure 31: Entire wear tracks for the wear test specimens charged and uncharged at 100x magnification showing areas of adhesion in squares as well as 500x magnification of the circled regions. 3003-H14 aluminum: uncharged-100x (*a-1*) -500x (a-2), charged-100x (*b-1*) -500x (b-2), 2618-T61 aluminum: uncharged- 100x(*c-1*) -500x (c-2), charged -100x (*d-1*) -500x (d-2), Ti-6Al-4V: uncharged -100x (*e-1*) -500x (e-2), charged -100x (*f-1*) -500x (f-2)

Microscopic images of the wear tracks at 200x magnification are shown in Figure 32.

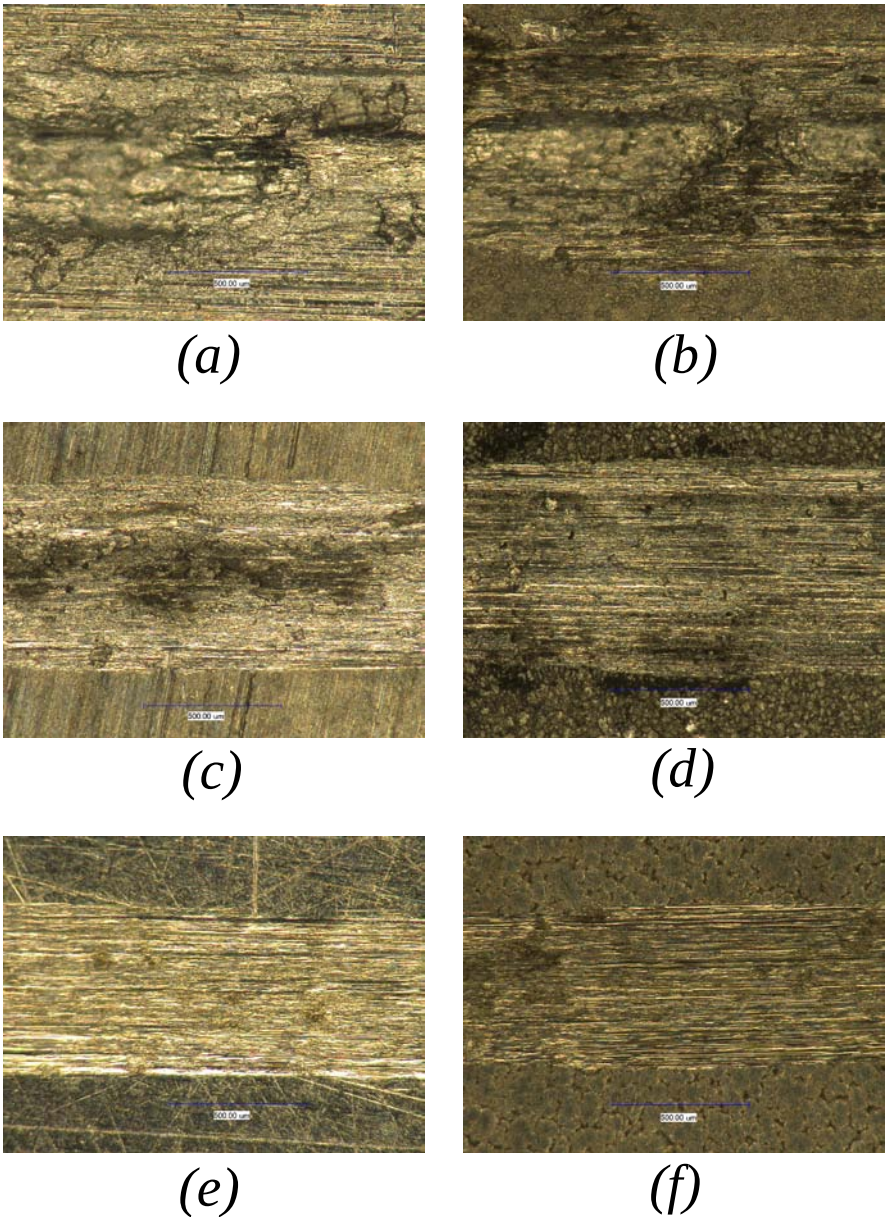

Figure 32: Microscopic images at 200x of the wear track after the wear volume removed and coefficient of friction tests showing 3003-H14 aluminum- (*a*) uncharged, (*b*) charged, 2618-T61 aluminum- (*c*) uncharged, (*d*) charged, Ti-6Al-4V- (*e*) uncharged, (*f*) charged

Microscopic images of the ball bearing used during tribiological testing are shown in Figure 33. The images show that the wear on the ball during testing was similar for both charged and uncharged conditions.

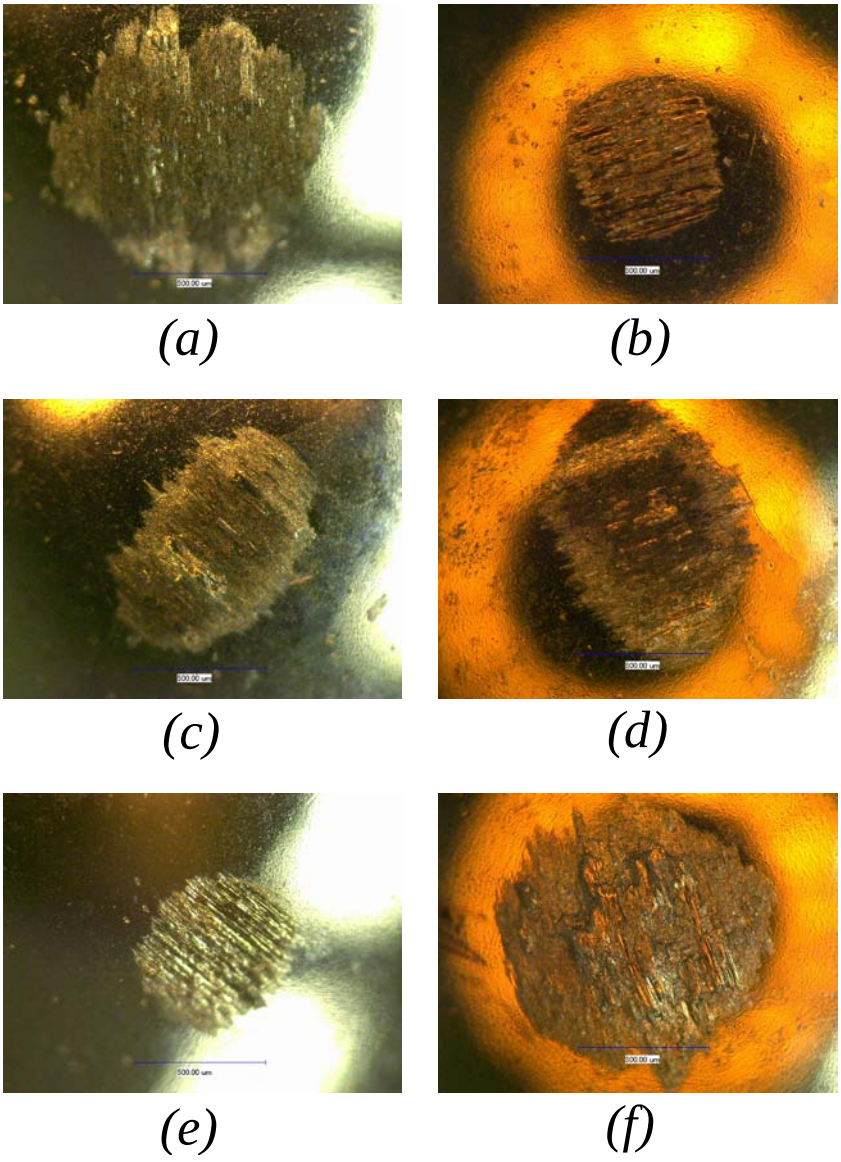

Figure 33: Wear on ball after wear volume removed testing at 200x magnification showing 3003-H14 aluminum- (*a*) uncharged, (*b*) charged, 2618-T61 aluminum- (*c*) uncharged, (*d*) charged, Ti-6Al-4V- (*e*) uncharged, (*f*) charged

4.5. Chemical Analysis

Chemical analysis of the Ti-5Al-4V charged and uncharged specimens is shown in Figure 34. The images label the titanium peaks with black circles and titanium hydride peaks with red triangles.

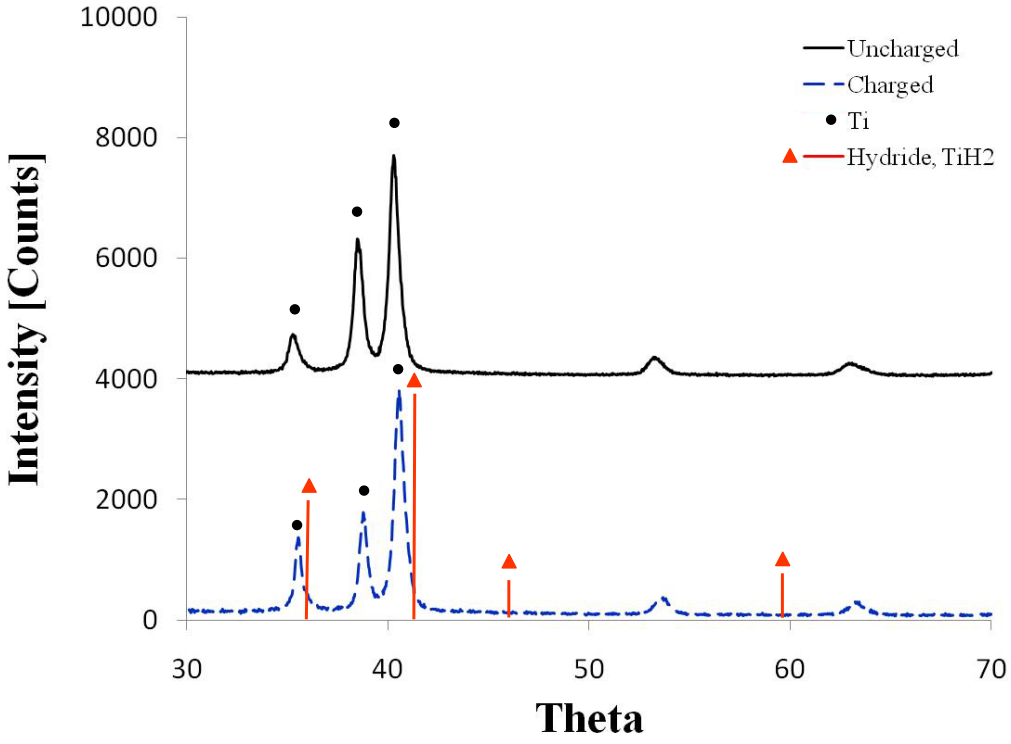

Figure 34: XRD of charged and uncharged Ti-6Al-4V specimens showing TiH2 peaks

4.6. SEM Imaging

Scanning Electron Microscopic images of the fracture surface for each material at each condition are shown in Figures 35-37. Comparing the uncharged surface with the charged, the later of the aluminim alloys are clear and surface features were more

pronounced. The uncharged surfaces have a more deformed, i.e., ductile nature. This is however, not seen in the titanium alloy case.

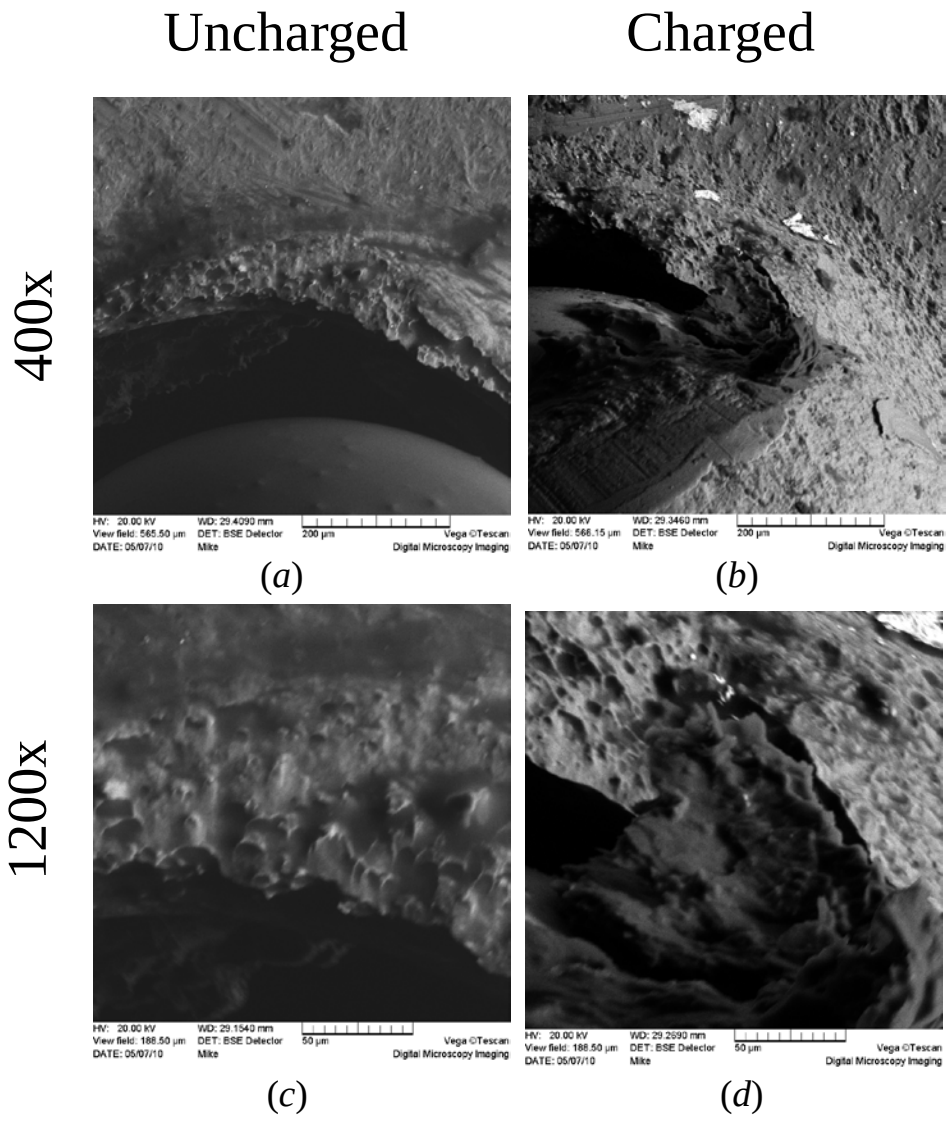

Figure 35: SEM images of 3003-H14 aluminum charged and uncharged specimens at 400x and 1200x

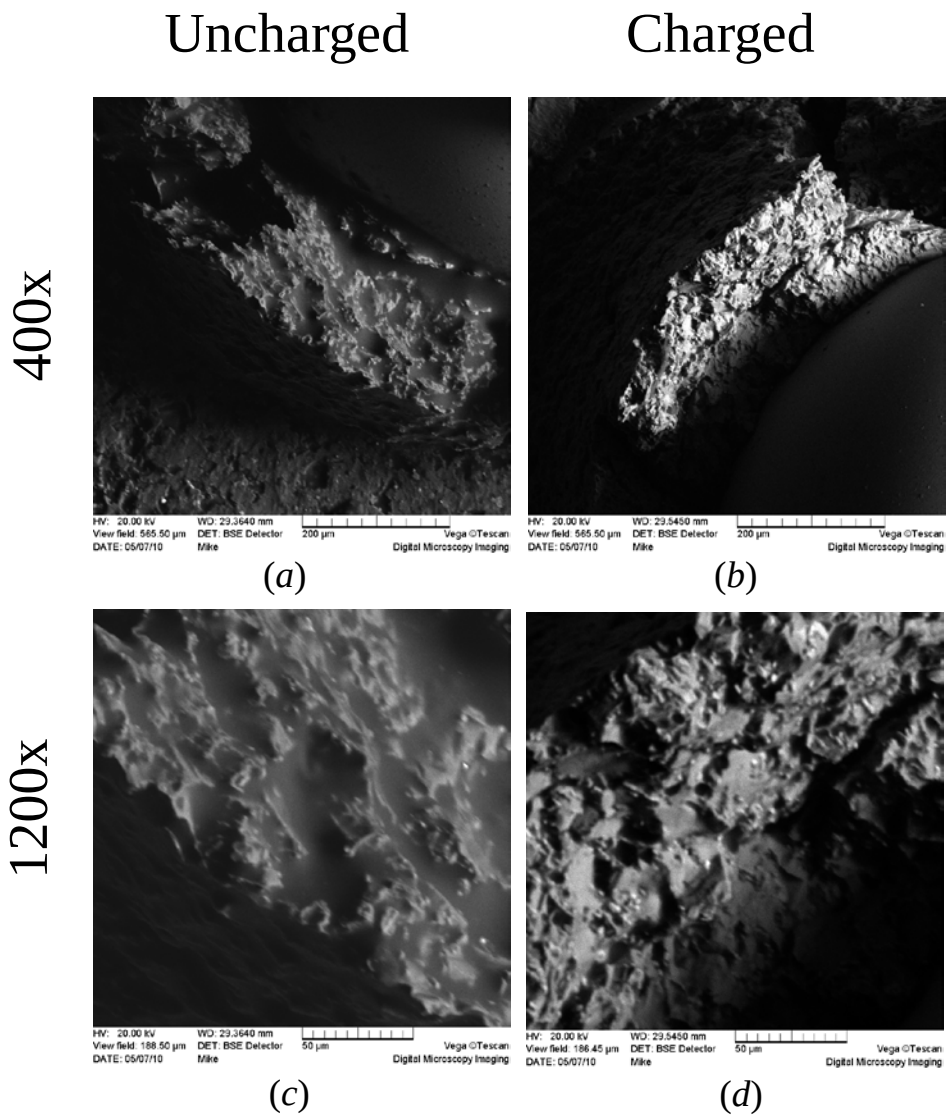

Figure 36: SEM images of 2618-T61 aluminum charged and uncharged specimens at 400x and 1200x

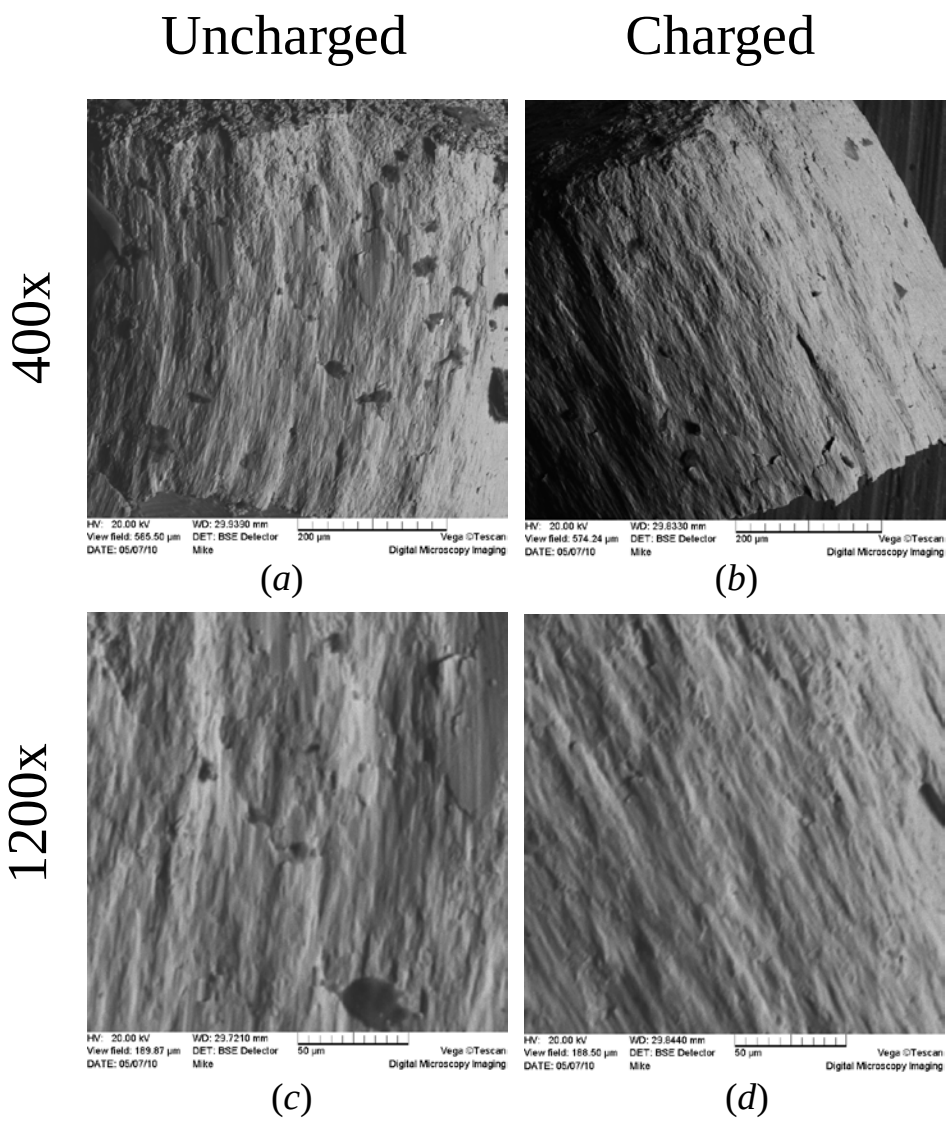

Figure 37: SEM images of Ti-6Al-4V charged and uncharged specimens at 400x and 1200x

CHAPTER V

DISCUSSIONS

This chapter discusses the results presented in the Chapter IV. Details will be given as to the repeatability of the Small Punch Test (SPT), the effects of surface roughness, and the material behavior found during small punch testing. Correlations will be given linking the SPT to the standard material parameters for aluminum alloys. A discussion of the effects of hydrogen on the mechanical and tribological properties of the alloys will also be provided including a relationship between wear rate and a SPT parameter.

5.1. Repeatability

In order to evaluate the repeatability of the SPT, at least three identical runs were conducted with identical conditions for each material. The overall percent error for each of the materials tested can be seen in Table 7. This overall percent error is an average of all the percent errors at each extension using the average as the true value. This percent error means that at each value of an extension, the force should lay within that percentage from the average. The highest percent error was 14.24% for the Ti-6Al-4V. This error is acceptable because it is small enough such that the force versus extension (FvE) curves for each of the materials are distinct as seen in Figure 14. Any error in a SPT could be attributed to material defects in the specimens, such as voids or a higher concentration of dislocations in some of the specimens. When testing the mechanical properties of a material, as the volume of the specimen decreases, material defects and dislocations have an increasingly important role in deformation because they cannot be

averaged out. With testing methods that have large test volumes, the effects of internal material defects can be averaged over the larger volume of the test specimen. Another source of error can include testing jig misalignment. If the test jig is not perfectly circular, differences in loading geometry could result in different results when testing identical specimens. Changes in a specimen's geometry could also result in different FvE curves. Overall the percent error for all the tested materials is acceptably low and the SPT shows good repeatability for titanium and aluminum alloys.

5.2. Effects of Surface Roughness

It is seen that the specimens created from the sheet form have similar roughness and the roughness is much lower than the WEDM cut specimens from stock bar. The surface roughness for the sheet specimens is the result of the extrusion process to form the sheet metal the specimens were cut from. The roughness from the stock bar specimens is the result of the cutting process involved from the electrical current that was used to slice the disks. The average overall percent error for the different roughness 3003-H14 aluminum specimens was 4.3%. It’s noted that the roughness range was from 0.450-μm to 3.011-μm. The error for specimens whose roughness range was ± 0.0395 μm was 6.1%. This error is lower than the error for the SPT of samples of identical surface roughness as seen in Table 7. This means that the roughened specimens did not contribute statistically to the overall percent error of the SPT. The average deviation over the entire extension length was calculated to be 2.0146 Newtons. This small change in the force versus extension curve is expected because the magnitudes of the peaks on the surface of each sample are relatively small compared to the diameter of the ball

bearing. Each sample can be graphically represented as seen in Figure 38. The figure shows sample surface roughness of increasing magnitude from A to C.

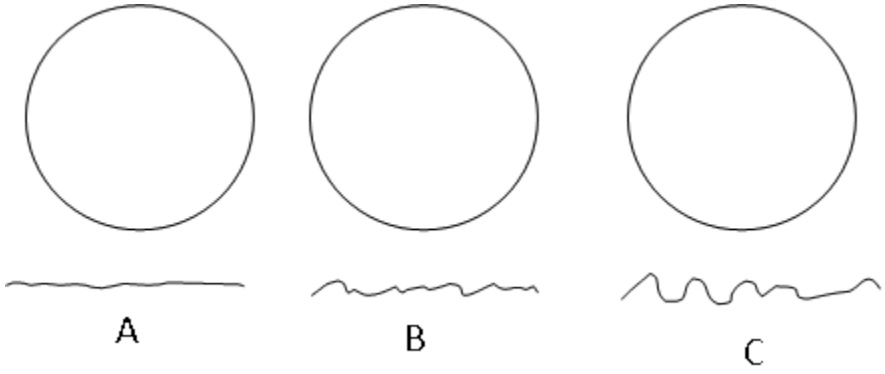

Figure 38: Cross-sectional view of the ball bearing and the different roughness

As the ball bearing pushes into the surface of a sample it will first come in contact with the highest peak on the surface as shown in Figure 39, part A. As the ball bearing is pushed further into the surface it will sense resistance from only those high peaks as shown in B. When the ball continues to push into the material the peaks that are in contact will deform and take the shape of the much harder ball bearing, as shown in part C. Once the ball has been pushed into the surface of the material a depth equal to or greater than the deepest valley of the roughness peaks, the ball and surface will be fully contacted and the material will continue to deform to the shape of the ball as in part D. The overall force versus extension curve will not be affected by surface roughness after the surface of the material has completely formed to the ball bearing. The very small region between where the ball bearing contacts the top peaks and the surface conforms

to the ball will vary depending on surface roughness. However, this region is small and has little effect on the overall force versus extension curve.

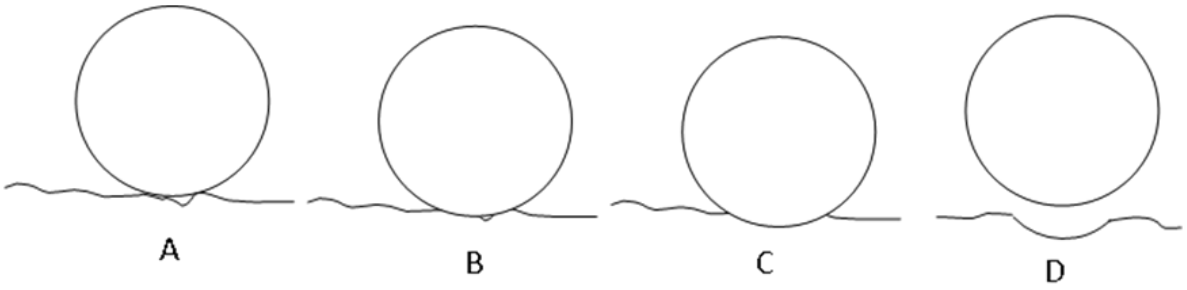

Figure 39: Diagram showing how the ball bearing impacts the surface of a sample

It can be seen that extreme surface roughness could affect the force versus extension curve because the surface peaks would be so large that their deformation to conform to the ball would require large enough amounts of force that it would show on the force versus extension curve. An example of this is seen in Figure 40.

Figure 40: Cross-sectional view of an extreme roughness

From the results, it can be seen that over a surface roughness range of 0.450 μm to 3.011 μm the effect of surface roughness was found to be negligible. This means that

the SPT can be used to compare the mechanical strength properties of materials with similar but different roughness values.

5.3. Behavior of Materials

The FvE curve from a SPT can show how a material resists a centrally loaded biaxial bending stress. For all of the SPTs on all three of the materials, the FvE curves show similar regions that were reported by Vorlicek and Eskner [48, 72] for low-alloy ferritic steels. Of the FvE curves a general trend of five distinct regions can be seen. An example of the regions is shown in Figure 41.

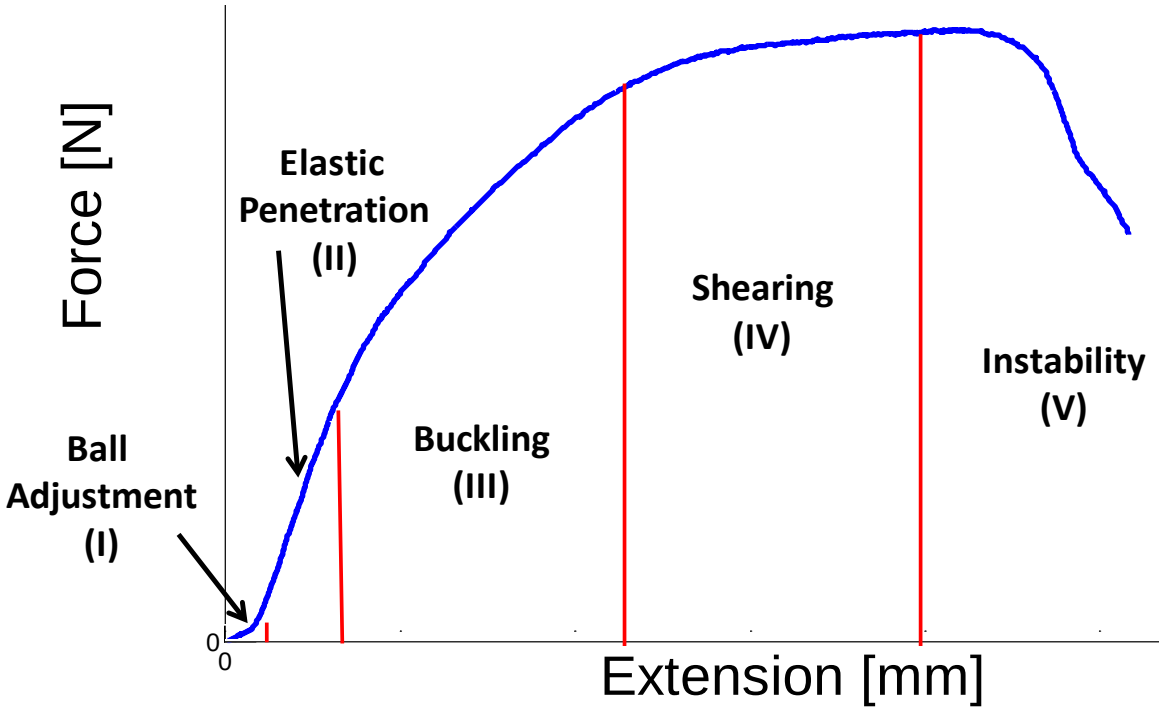

Figure 41: Regions of material behavior during a SPT

The first region is represented on the curve by the ball contacting the surface of the specimen and pushing itself into the material as discussed earlier in regards to the roughness. As the ball pushes into the specimen there is a slight amount of plastic deformation directly under the ball. This region is shown as a parabolic shape on the FvE because as the ball settles into the material the contact area between the ball and the specimen increases. The contact area as a function of extension can be seen in Equation 6 where δ is the extension of the ball into the material.

$$Contact\ Area = -18\pi\cos\left[2\sin^{-1}\left(\frac{1}{6}\sqrt{6\delta}\right) - 1\right] \quad (6)$$

The derivation of Equation 6 can be seen in Appendix B. Once the contact area between the ball and the specimen is sufficient enough, the entire specimen will undergo elastic deformation as depicted on p.68. This elastic deformation can be seen in the FvE curve as a linear region. If the load is removed during a SPT in this region, the specimen will return to its original shape. As the ball continues to push into the material, a biaxial stress state is developed and the FvE curve begins to change slope as seen in region III of Figure 41. While undergoing a SPT, a specimen is being work hardened as dislocations within the material move and plastic deformation occurs. During this yielding the specimen begins to thin and localized necking takes place under the ball bearing as the material is being stretched as seen in region IV. The FvE curve then reaches a maximum and drops as the material fails by necking or through crack propagation in region V. The 2618-T61 aluminum and Ti-6Al-4V specimens seem to fail

by crack propagation while 3003-H14 aluminum fails through necking as evident of the lack of a fracture surface seen in Figure 15. This shows the ductility of the 3003-H14 specimens compared to the other alloys. Information about the amount of plastic yielding taking place during each region can be gained through analysis of the stop tests shown in Figure 25. The stop tests show the amount of elastic recovery from the specimen within each region. It can be seen that in the initial regions I and II the reloading curve follows closely the same path prior to unloading. However, in regions III-V the reloading curves are much different. What this means is that after each stop test, the next run will start with a linear increase of force verses the depth, i.e., elastic regime, and once reaching the stopped point, the curve continues to show plastic deformation. After the extension from the previous run is reached the FvE curve will continue as a normal test as shown in Figure 26.

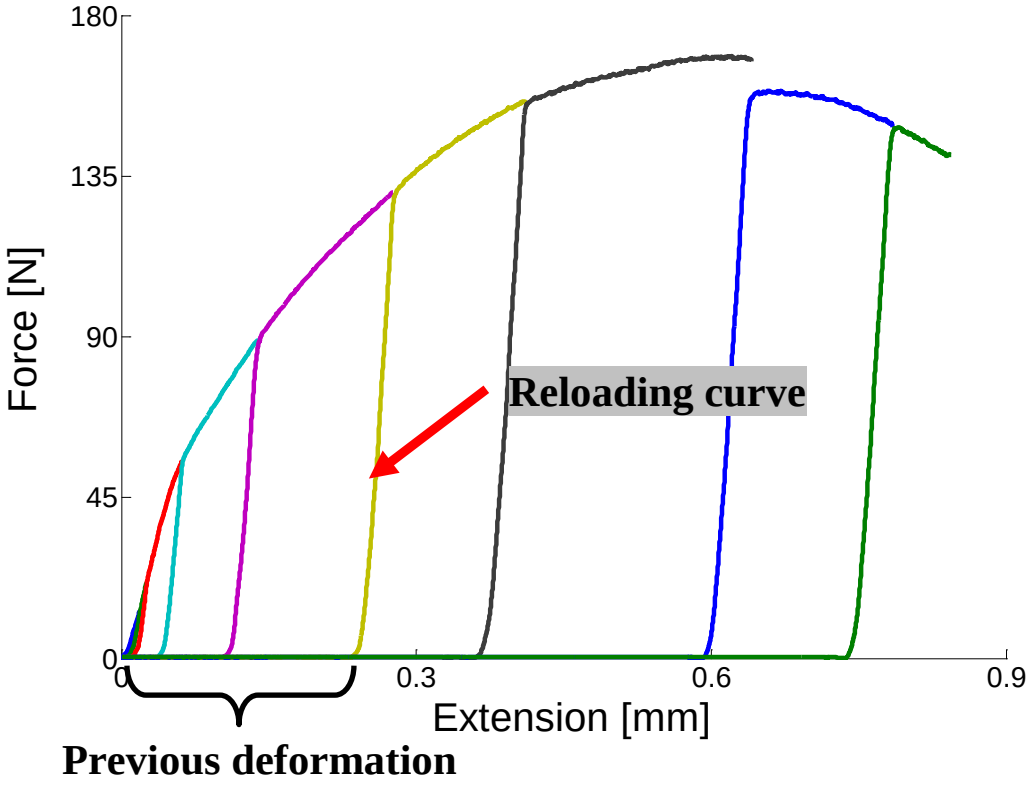

Figure 42: FvE curve for stop test runs showing reloading curves and previous deformations

The slopes of each of the reloading curves were found to increase through regions I through IV but decrease in region V as seen in Figure 42.A schematic of how the material is deforming during each of the regions can be seen in Figure 43. The sudden drop at 0.6 mm is most likely the shear shown in Figure 43 in the IV region shown below.

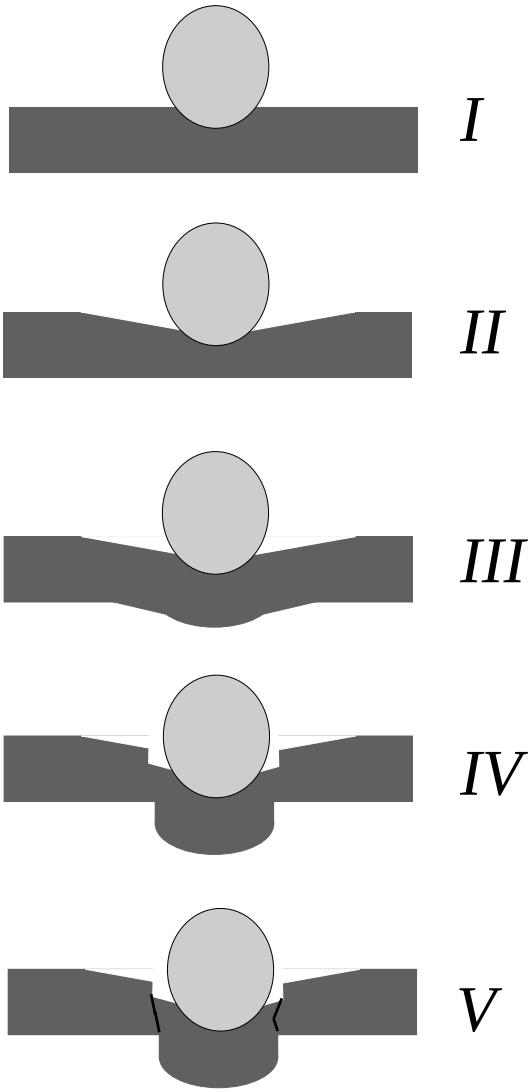

Figure 43: Schematic of how a specimen is deforming during the five regions of a typical FvE curve

Evidence of the accuracy of the behavior predication seen in Figure 43 can be seen in actual specimens pictures in Figure 44. The sheared surface seen in region IV is labeled and the initial cupping of the material taking the shape of the ball bearing, of region III, can be seen directly below the ball on the adjacent side.

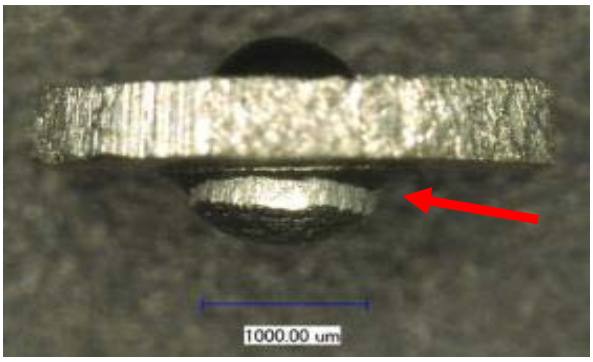

Figure 44: Side view of a specimen after testing

From the results shown in Figure 14 and Table 7, the SPT gives good comparative results for the different aluminum and titanium alloys tested. The material with the highest ultimate tensile strength (Ti-6Al-4V, 900-MPa) did show the highest maximum force on a FvE curve. These results suggest that the SPT could be used to qualitatively compare the strength of materials for both titanium and aluminum alloys. Up until this point, any quantitative prediction of material properties was derived using steel specimens as test subjects. Three other aluminum alloys were tested in order to gain a better approximation. The material properties of these alloys can be seen in Table 9.

Table 9: Material properties of the aluminum alloys tested

	Tensile Strength [MPa]	Yield Stength [MPa]	Modulus of elasticty [GPa]
Al 1100-O	90	34	68
Al 3003-H14	150	145	68
Al 2024-T3	485	345	72
Al 2618-T61	440	370	74
Al 7075-T651	570	505	71

The maximum force achieved during small punch testing is proportional to the material's ultimate tensile strength and a correlation can be seen in Figure 45. This figure plots the measured maximum punch force for a number of different aluminum alloys against their known uniaxial ultimate tensile strength.

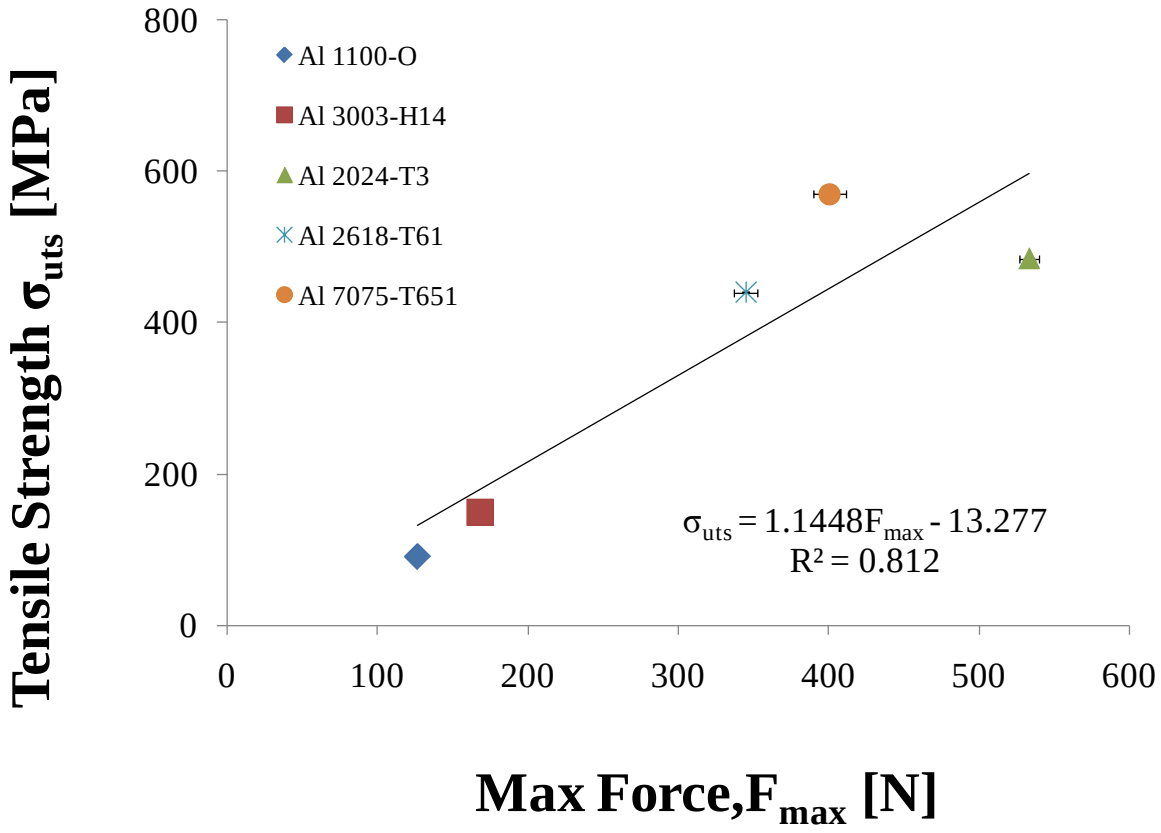

Figure 45: Plot comparing the maximum force obtained from the SPT with the known ultimate tensile strength

It can be seen that a liner trend has developed and a relation between the tensile strength and maximum punch force for these aluminum alloys can be seen in Equation 7, where F_{max} is the maximum force seen on the SPT in Newtons.

$$\sigma_{uts} = 1.145F_{max} - 13.28 \qquad (7)$$

The coefficient in front of the maximum force in Equation 7 is a material parameter related to the strength of the atomic bonds specific to these aluminum alloys. It is predicted that other material classes will have a different coefficient in Equation 7. This explains the differences between the derived equation here (Equation 7) and Mao and Takahashi's equation (Equation 2). The maximum force can also be represented in terms of the contact pressure between the ball bearing and the specimen. A comparison of this ball contact pressure and the tensile strength is shown in Figure 46.

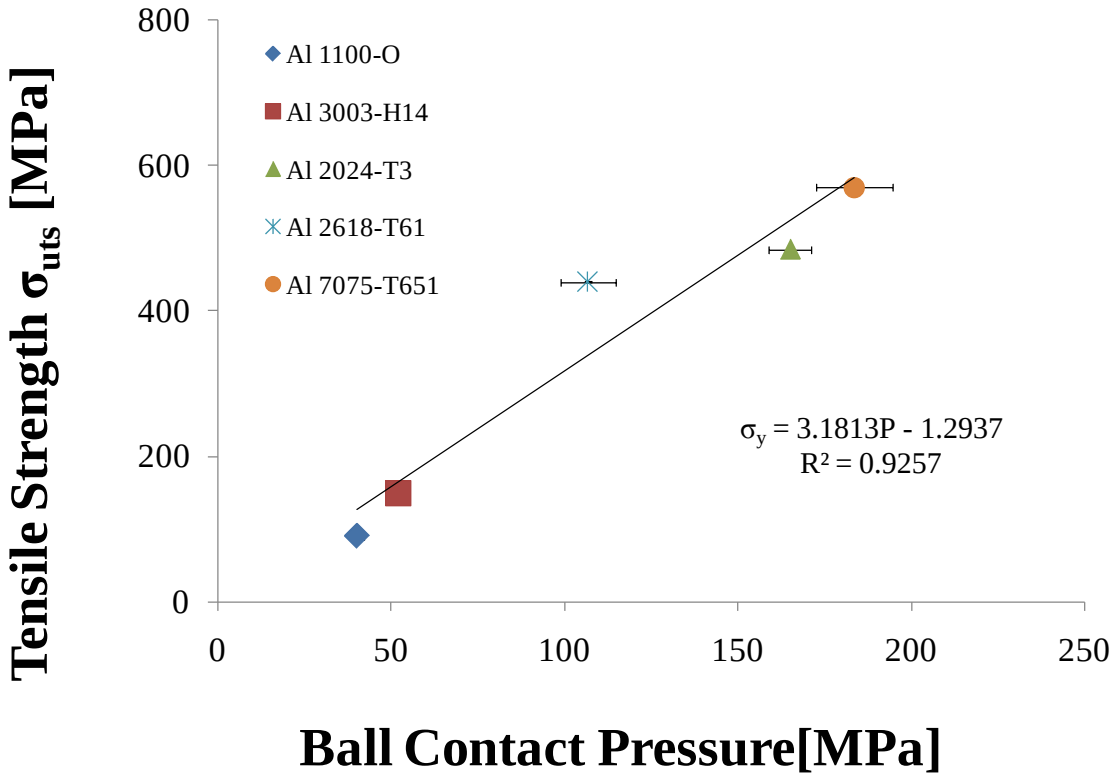

Figure 46: Relation between ball contact pressure and known tensile strength of the aluminum alloys tested

A relation can be derived between the contact pressure (P), in MPa, and the known tensile strengths of the aluminum alloys. This correlation can be seen in Equation 8.

$$\sigma_{uts} = 3.18P - 1.29 \qquad (8)$$

The relationship in Equation 2 was derived through the testing of steel specimens. Iron, the main element in most steels has a body-centered cubic crystal structure while most aluminum has a face-centered cubic crystal structure. Drawings of the crystal structures of the two materials can be seen in Figure 47.

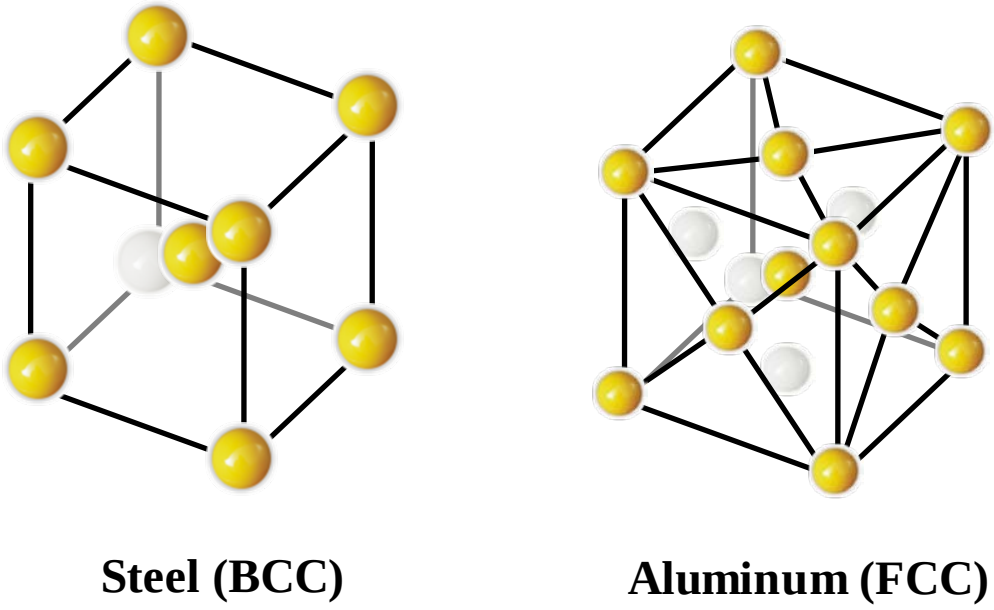

Figure 47: Crystal structures of steel and aluminum

The equation is a modified version of the Mao and Takahashi model. This equation is proven to be suitable for aluminum alloys. The maximum force for the 3003-H14 aluminum specimens occurred deeper than other materials. This would suggest that 3003-H14 aluminum is more ductile than the other materials mentioned. The ductility of

the 3003-H14 aluminum specimens can also be seen in Figure 15, where the 3003-H14 aluminum specimen is the only material tested that did not show any cracks after testing. It is predicted that the 3003-H14 specimens failed due to a loss of stability in the necking region depicted in region III of Figure 43. The 2618-T61 aluminum specimens showed cracks that start at the center of where the ball bearing was placed and extend radially outward. The cracks in the Ti-6Al-4V specimens are circumfrencial and can be seen on the opposite side of the specimen as the ball bearing. The depth at which the maximum force occurs during small punch testing could be used to qualitatively compare the ductility of materials. The area under the curve up to the maximum force can also be used to compare the toughness of a specimen. The area, given in Joules in Table 7, shows that the material with the highest toughness, like Ti-6Al-4V, also has the highest area and the material with the lowest toughness has the lowest area, such as 3003-H14 aluminum.

5.3.1. Small Punch Block Testing

During block testing a specimen is not allowed to bend and it must accept the force of the ball bearing much in the same way as a Brinell hardness test. The results of the block test are shown and compared to a normal SPT in Figure 17 through Figure 19. These figures show that the block test and the normal SPT show very similar FvE curves up to a certain point in regions I and II. Figure 48 and Figure 49 show how the mechanical behaviors of the specimens react in the different regions for the block and normal SPTs respectively.

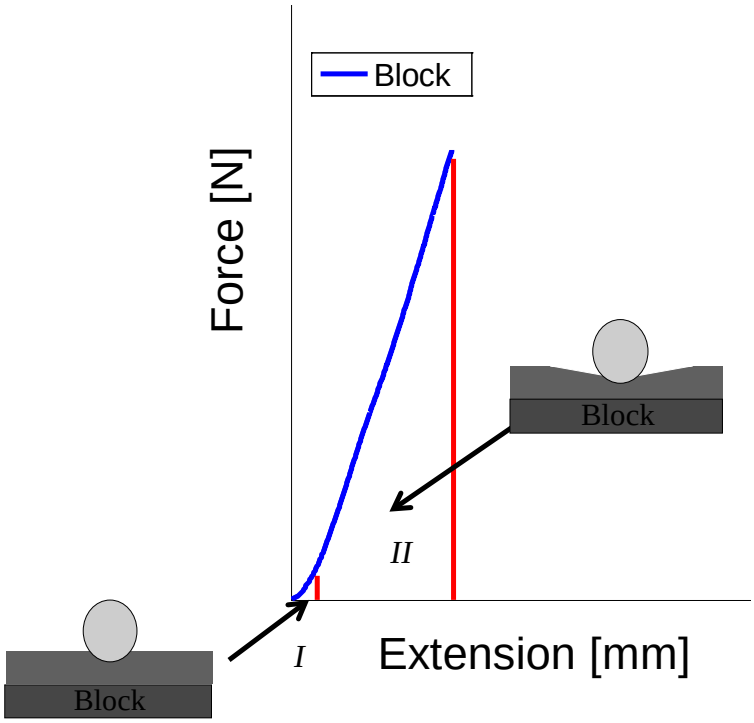

Figure 48: Illustration showing how the material behaves during a small punch block test

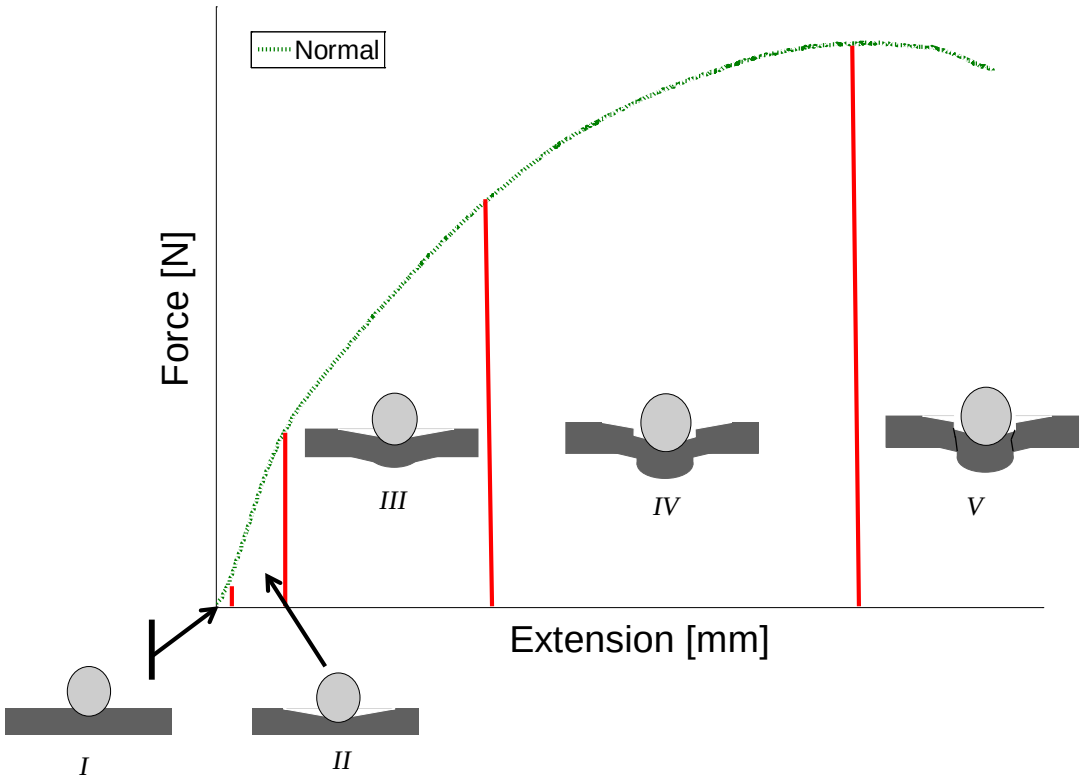

Figure 49: Illustration of the behavior of the material during testing

Using these two figures it can be seen that in regions I and II the FvE curves are similar because the mode of deformation is similar. However, during the block test the buckling mechanism normally seen in region III is restricted. Therefore, the specimens are constrained and not allowed to bend. The point where the block test curve and the SPT curve deviate is the point during a SPT where the specimen's deformation transfers from a majority of elastic compression to a majority of plastic yield bending. It is after this point on the SPT that the specimens exhibit highly irreversible plastic bending and the material work hardens. It is this work hardening effect that is responsible for the smaller but still positive slope of the FvE curve seen in the buckling region III.

The slope of this initial linear region seen in the small punch and block tests is plotted in Figure 50 for some common aluminum alloys tested.

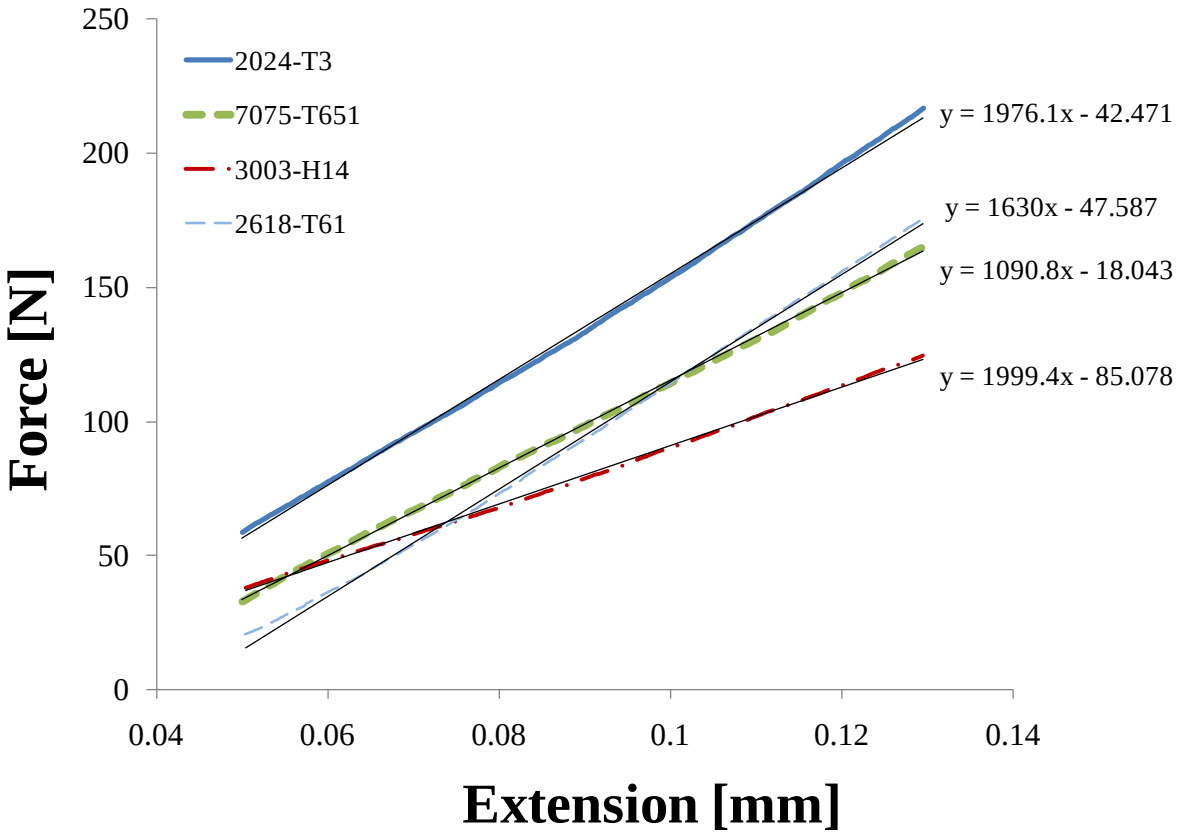

Figure 50: Plot of the small punch block test linear region of the FvE curves for four aluminum alloys

The slopes of the curves in Figure 50 can be compared to the known modulus of elasticity for the materials tested and shown in Figure 51. A linear trend can be seen.

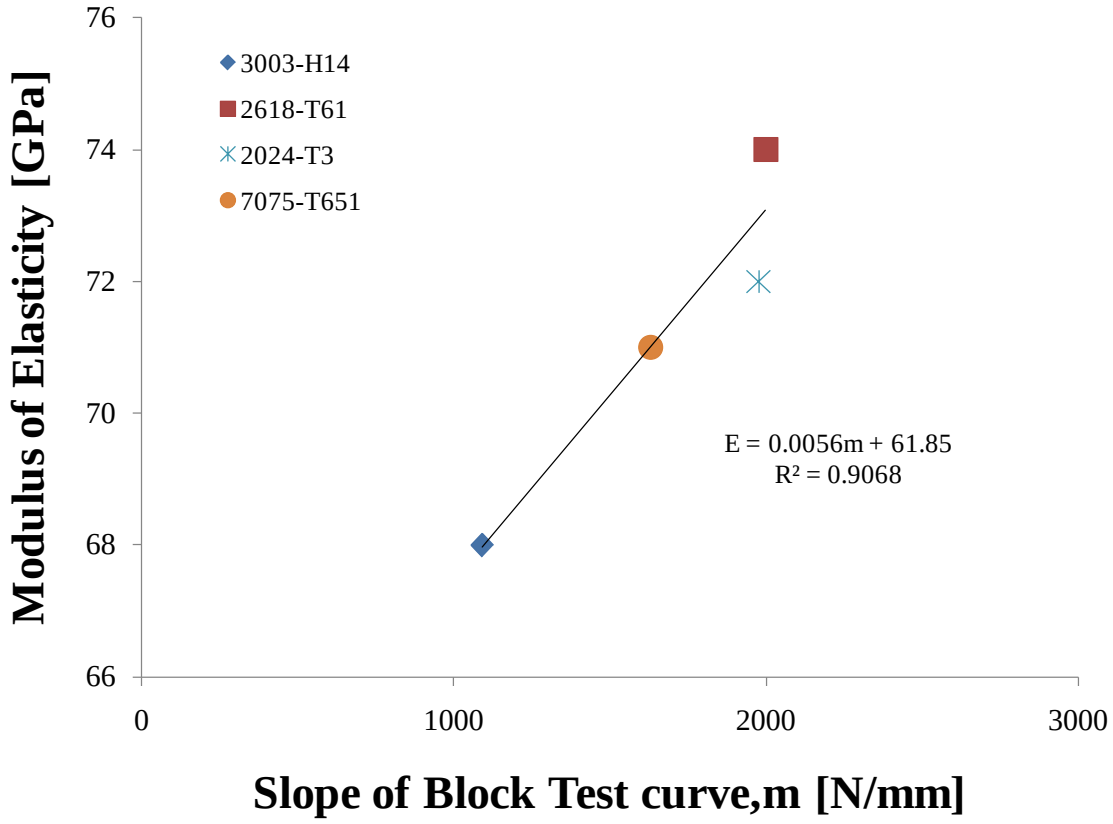

Figure 51: Relationship between the linear slope of four aluminum alloys and their modulus of elasticity

The relationship that links the slope of the block test curve is shown in Equation 9 where E is the modulus of elasticity in GPa and m is the slope parameter from the SPT block test in N/mm.

$$E = 0.0056m + 61.85 \qquad (9)$$

Equation 9 is the first relation that links a SPT parameter to the modulus of elasticity of materials.

It can be seen from the results in Figure 16 and Table 3 that the material hardness can be related proportionately to the slope of the block test curve. Ti-6Al-4V, with the

highest hardness and yield strength, has the highest slope in Figure 16 and of all the materials tested. When comparing a block test to a normal SPT with no block as in Figure 17, Figure 18, and Figure 19 it can be seen that the slopes of the linear regions are different for the different materials tested. A plot comparing the slope from the block test(m) and the known Brinell hardness is shown in Figure 52.

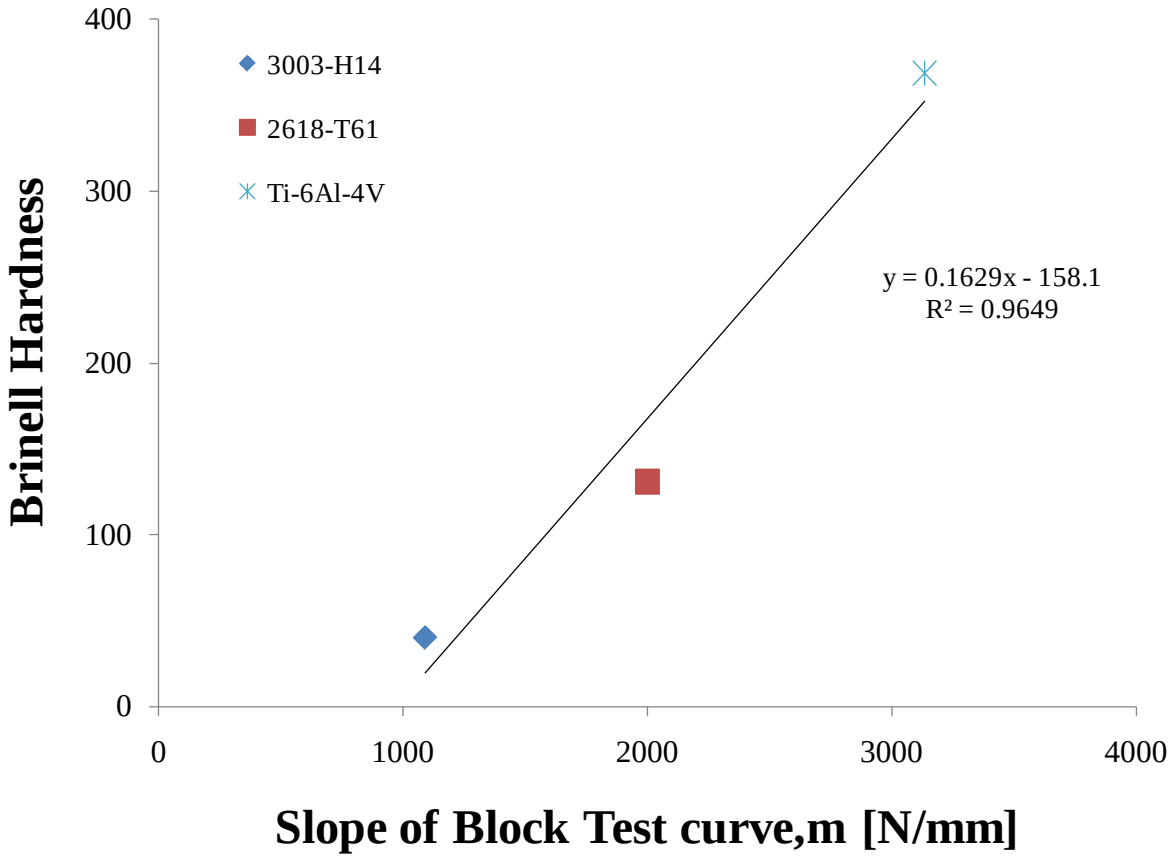

Figure 52: Relationship between the linear slope of four aluminum alloys and their Brinell hardness

The relationship between Brinell hardness and the slop of the block test can be seen in Equation 10.

$$H = 0.163m - 158.1 \qquad (10)$$

It has also been seen that the yield strength of a material could be qualitatively compared and related to the initial slope of the FvE curve. The slope of the initial region has shown to increase with higher yield strength of the test material. This can be seen in Figure 53.

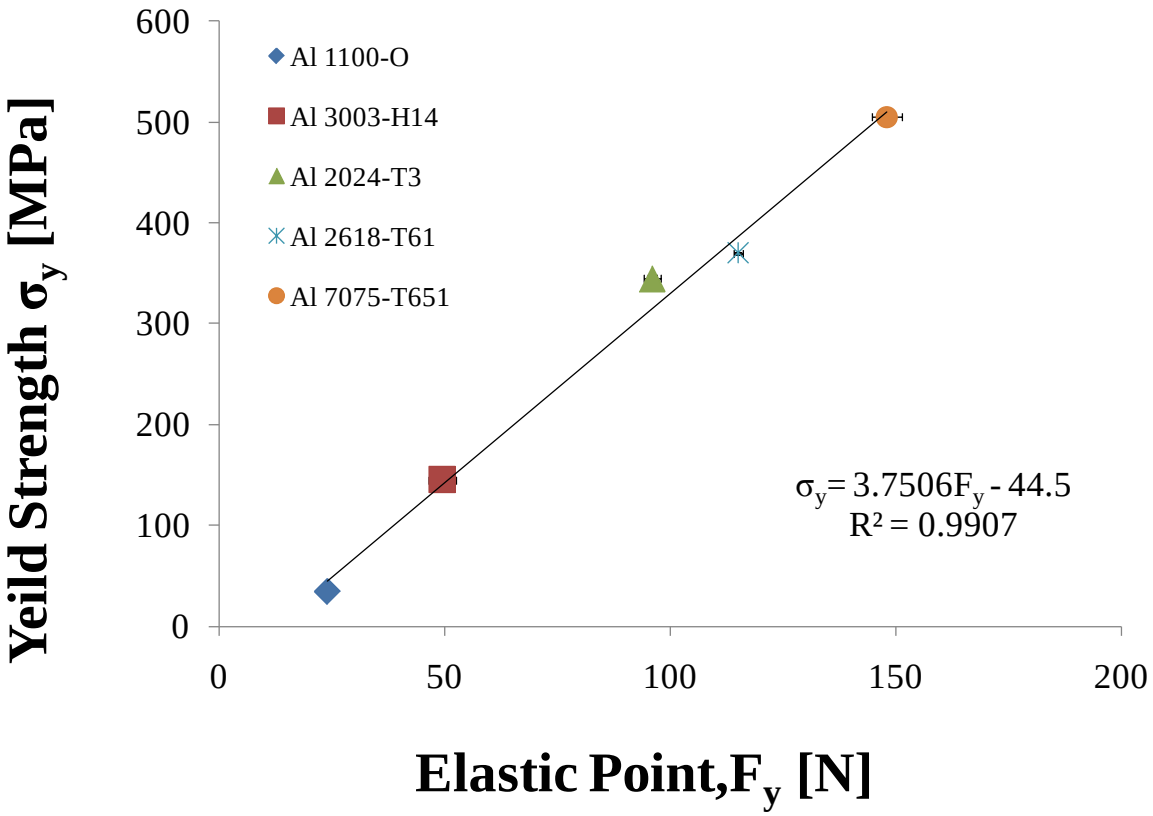

Figure 53: Plot comparing the elastic point of the SPT to the known yield strengths of different aluminum alloys

The derived relationship between the elastic point (in Newtons) from the SPT and small punch block tests and the known yield strength can be seen in Equation 11.

$$\sigma_y = 3.75F_y - 44.5 \qquad (11)$$

Table 10 shows the results of plugging the maximum force (F_{max}) and stray from linearity(F_m) for the aluminum samples into the equations listed in Equations 1-4.

Table 10: Comparison of different predicted values of tensile and yield strength from SPT relations

Ultimate Tensile Strength [MPa]

	Real Value	Sanders	Mao	Milicka
Al 1100-O	90.0	131.5	32.9	42.8
Al 3003-H14	150.0	179.5	43.8	57.0
Al 2024-T3	485.0	597.5	138.7	180.5
Al 2618-T61	440.0	381.4	89.6	116.7
Al 7075-T651	570.0	445.2	104.1	135.5

Yeild Strength [MPa]

	Real Value	Sanders	Mao	Milicka
Al 1100-O	34.0	45.1	32.9	42.8
Al 3003-H14	145.0	141.0	43.8	57.0
Al 2024-T3	345.0	315.6	138.7	180.5
Al 2618-T61	370.0	386.8	89.6	116.7
Al 7075-T651	505.0	510.6	104.1	135.5

It can be seen that the equations from literature do not necessarily agree with each other. The new relations derived in this chapter show much closer agreement. This is due to the fact that the Mao and Milicka relations were both derived using steel test specimens. The present relation was derived using aluminum alloys that represent a closer correlation when predicting the same.

5.3.2. Hydrogen Effects

In regards to how each of the specimens interact with hydrogen during charging, three occurrences are possible:

1. Hydrogen did not enter the matrix of the test specimens
2. Hydrogen did enter the matrix and hydrides were formed
3. Hydrogen entered the matrix but in not high enough concentration to allow hydride formation

The first case is unlikely due to the abundance of molecular and nascent hydrogen that is present at the surface of the specimens during charging. During charging the zinc powder will come in contact with the specimens creating a galvanic couple which will facilitate in creating a potential difference between the two metals. This is schematically illustrated in Figure 54.

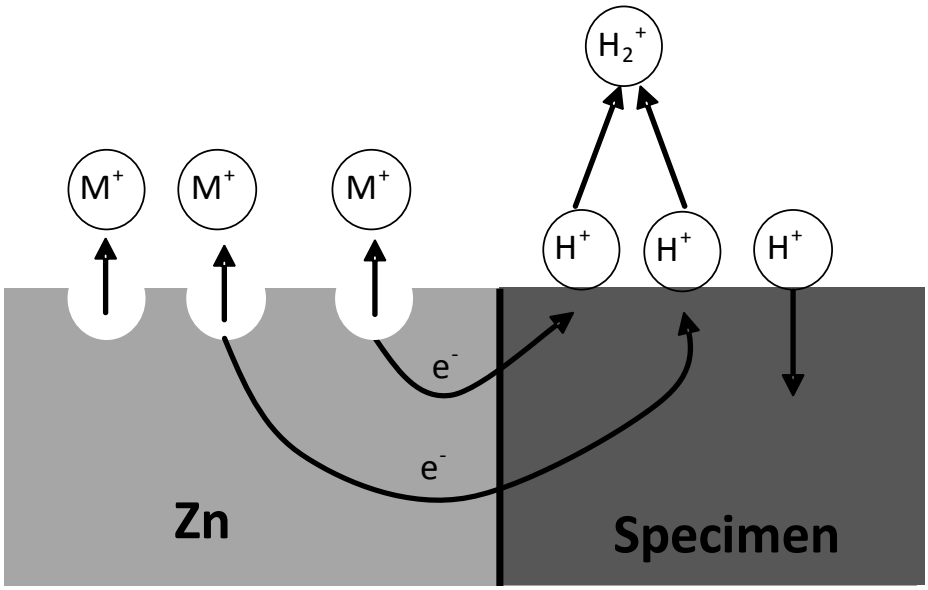

Figure 54: Galvanic couple that exists between the zinc and the specimens during charging

The potential between the two metals will create a driving force for current. Compared to all of the specimens (aluminum and titanium), zinc has the highest (negative) electrode potential and thus will always be more active. This means that when coupled with the specimens, the zinc will act as an anode. Anodic reactions will occur on the zinc surface creating zinc ions that will go into the sulfuric acid solution. The electrons from these ions will then transfer to the cathodic specimens. The less active specimens will then act as cathodes accepting the electrons from the zinc and having them participate in hydrogen evolution at the surface. It is these hydrogen atoms what are highly likely to absorb into the bulk matrix of the specimens. Any gaps, cracks, and spaces would allow the H_2 to enter the surface. The hydrogen is energetically favorable to get into the sample surface.

The second possible condition of having hydrogen exist within the bulk of the specimens in large enough concentrations to create hydrides is unlikely due to the lack of the hydride phase seen in the XRD analysis shown in Figure 34.

Due to the amount of hydrogen adjacent to the specimens during charging it is likely that hydrogen did enter the bulk of the specimens. However, because of the lack of evidence supporting the presence of hydrides from the XRD chemical analysis it is unlikely that hydrides were formed within the bulk of the specimens. This leaves the third condition as the most likely occurrence during charging. Hydrogen was absorbed within the bulk of the material, however it did not exist in large enough concentrations to promote a phase change. The SPT curves in Figure 20 and Figure 21 for the aluminum specimens show statistically no difference between the charged and uncharged samples.

This means that after sitting in a diluted acidic bath with hydrogen gas production for 48 hours, the 3003-H14 aluminum and 2618-T61 aluminum specimens did not statistically show a loss of strength, ductility, or toughness. These alloys both have an ultimate tensile strength below 500 MPa which supports the idea that low-strength alloys are less susceptible to hydrogen embrittlement[9]. Aluminum itself is not a transition or rare earth element, thus the bulk of the aluminum alloy specimens would not form a hydride with hydrogen which could result in unexpected failure. Both of the aluminum specimens contain the transition metals iron, copper, manganese, and zinc with 2618-T61 aluminum also containing titanium and nickel. These elements could form hydrides in the presence of hydrogen, however in both aluminum specimens these elements only exist in less than 3%wt. Showing no strength change in these samples, it is possible that the hydrogen content within the sample was not sufficient enough to allow the formation of a hydride or the weight percent of the transition metal alloying elements was low enough that the strength was not affected. These results suggest that the amount of hydrogen within the bulk of the aluminum alloys was low enough not to affect any mechanical properties. This low amount of hydrogen absorption could be due to the relatively thick oxide layer that aluminum forms in air. Figure 22 shows that the Ti-6Al-4V specimens experienced a change in the way the material behaves under deformation. It has been seen in literature that titanium is affected by hydrogen [73]. A comparison of the results of the SPT for the charged and uncharged condition can be seen in Table 11.

Table 11: Comparison of the SPT parameters for the charged and uncharged conditions

Material		Overall percent error [%]	Area under curve [J]	Average maximum force [N]	Dept at maximum force [mm]
Uncharged	3003-H14	6.13	0.0776	169.21±0.735	0.7082
	2618-T61	14.24	0.1107	343.08±10.2	0.4949
	Ti-6Al-4V	11.11	0.2216	874.52±49.5	0.4585
Charged	3003-H14	8.52	0.078	170.69±9.59	0.63
	2618-T61	11.73	0.095	328.92±4.92	0.45
	Ti-6Al-4V	20.01	0.213	834.78±33.2	0.59

The bulk of the Ti-6Al-4V specimens is a transition metal and the formation of a hydride would be the most likely culprit for affecting the material during small punch testing. However, no hydride formation was shown in the XRD analysis. The relatively high ultimate tensile strength of the titanium specimens, when compared to the aluminum, suggests that higher strength alloys are more susceptible to a loss in toughness and strength due to hydrogen effects. It is believed that during the SPT small localized cracks would expand to show a lower force on the SPT curve; however, the cracks were not large enough to cause the entire material to fail in a brittle fashion. Blisters were not seen on the outside of the specimens tested, therefore it is believed hydrogen blistering was not a factor for the change in SPT curves for the Ti-6Al-4V or the aluminum alloys. However, hydrogen could collect and pressurize in voids to form blisters if sufficient time had been given. The chemical analysis reveals that no titanium hydride was formed in the specimens. This suggests that the amount of hydrogen within

the material was not sufficient enough to form hydrides, however it was enough to affect the mechanical behavior of the material. The small amounts of interstitial hydrogen could collect in voids and grain boundaries in small enough quantities to cause stress concentration but not large enough to cause a drastic reduction in the SPT maximum force. Due to the ductile nature of the failure of the charged aluminum alloys shown in Figure 35 and Figure 36, the SEM images of the fractured surfaces do not suggest a brittle failure. There is also no evidence of intergranular fracture within the bulk of the material, suggesting that any absorbed hydrogen at the grain boundaries did not affect the failure mechanism during small punch testing. Also, the charged and uncharged specimens show the same transgranular fracture and thus there was not a sufficient amount of intergranular absorbed hydrogen to cause a change in maximum punch force.

5.3.3. Tribological Analysis

Table 7 and Figure 30 show that for the uncharged specimens, a higher maximum SPT force of a material will result in a lower wear volume removed. That is to say that the greater the maximum SPT force, the greater the wear resistance of a material. This relationship can be seen in Figure 55. This means that the SPT can be used to qualitatively predict the wear resistance of materials whose volume is not sufficient enough to conduct a typical tribological analysis.

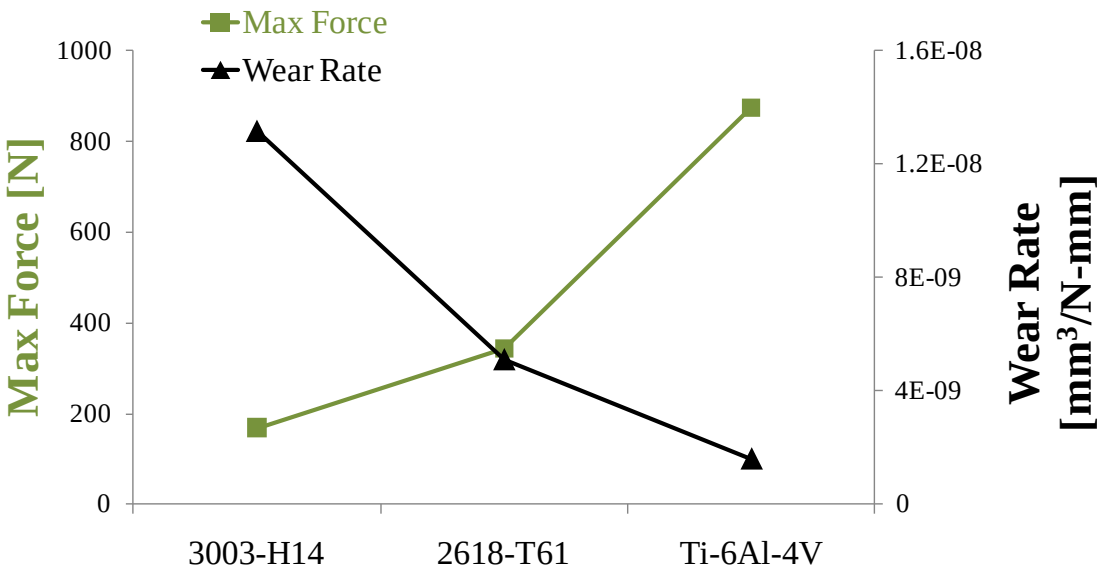

Figure 55: Relationship between uncharged SPT maximum force and wear volume removed

5.3.4. Tribological Analysis of Charged Specimens

Figure 29 and the results from the wear test indicate that the absorption of hydrogen showed no effect on the wear volume removed for any of the materials tested. The entire wear track for each test specimen in Figure 31 demonstrates this overall, for all three materials tested. The areas of adhesion are highlighted in squares. The mechanisms of wear were the same for both the charged and uncharged conditions. High magnification images of 500x in Figure 31 and 200x in Figure 32 of selected regions on the wear track show that for all of the materials, the main mechanism of wear is abrasion with some scattered regions of ductile tearing from localized adhesion. Figure 31 and Figure 32 show that the softest material, 3003-H14 aluminum, had the widest wear track with the most adhesion compared to the other two alloys. The hardest material, Ti-6Al-

4V, shows the smallest wear track and the least amount of adhesion. Figure 33 shows that the same type of wear was seen on the ball used during the wear test for both the charged and uncharged condition for all three allows. This further indicates that the amount of hydrogen absorbed during these tests did not alter the mechanism of wear for all three alloys.

CHAPTER VI

CONCLUSIONS AND FUTURE RECOMMENDATION

6.1. Conclusions

This research investigated the mechanical properties of common titanium and aluminum alloys at the small volume scale via test methodology in the surface-to-bulk region. The near-surface bulk behavior of aluminum and titanium alloys was studied using the Small Punch Test (SPT) and the surface behavior through tribotesting. The effects of environments such as hydrogen on those materials were also investigated. The 3003-H14 aluminum, 2618-T61 aluminum, and Ti-6Al-4V alloys were studied. Results are summarized in the following.

1. The SPT for such alloys were highly repeatable and specimen surface roughness did not have visible impacts on repeatability.
2. Analysis indicated that there was a link between the SPT and conventional mechanical properties. The relationship between the applied force and the slop of the FvE curve is associated with the tensile strength and elastic modulus. Numerical equations were developed.
3. The SPT can be used to qualitatively gage wear resistance.
4. There were no significant effects of hydrogen on the 3003-H14 and 2618-T61 aluminum alloys. The Ti-6Al-4V alloy, on the other hand, showed a much different FvE curve due to the absorption of a small amount of hydrogen.
5. Hydrogen showed no visible effects on friction and wear.

The significance of this research is the establishment of new links between the SPT and standard uniaxial tensile properties. The SPT is now more reliable and more versatile for applications in materials testing of materials with small specimen volumes. Correlations between SPT parameters and tensile strength, yield strength, modulus elasticity, and Brinell hardness have also been developed. The SPT was applied to the mechanical testing of hydrogen charged aluminum and titanium alloys.

6.2. Future Work

A small scale mechanical testing technique known as the Small Punch Test has been developed and applied to aluminum alloys. The SPT has been applied to the testing of hydrogen embrittlement. In order to gain a better understanding of how hydrogen affects the mechanical properties of materials several tasks need to be undertaken in the future.

1. The verification of the correlation developed here can be done through more repeated tests.
2. The methodology and correlation will be used to test many other materials to extend its applications.
3. Specimens will need to be charged in a high temperature, high pressure gases.

REFERENCES

1. Abbott, D., "Keeping the Energy Debate Clean: How Do We Supply the World's Energy Needs?" *Proceedings of the IEEE*, Vol. 98, No. 1, 2010, pp. 42-46.

2. DOE, Rep. "International Energy Outlook," 2009, *U.S. Department of Energy*: Washington, DC 20585.

3. DOE, Rep. "Annual Energy Outlook 2008," *U.S. Department of Energy*: Washington, DC 20585.

4. Forecasting, Rep. E.I.A.O.o.I.A.a., "International Energy Outlook,". *Energy*, 2009, US Department of Energy: Washington, DC 20585.

5. Balat, M., "Potential Importance of Hydrogen as a Future Solution to Environmental and Transportation Problems," *International Journal of Hydrogen Energy*, Vol. 33, No. 1, 2008, pp332-339.

6. Campen, A., Mondal, K., and Wiltowski, T., "Separation of Hydrogen from Syngas using a Regenerative System," *International Journal of Hydrogen Energy*, Vol. 33, No. 1, 2008, pp332-339.

7. Song, C., "Overview of Hydrogen Production Options for Developing Hydrogen Energy, Fuel Processing for Fuel Cells and Mitigation of CO2 Emissions," *Ranliao Huaxue Xuebao/Journal of Fuel Chemistry and Technology*, Vol.33, 2005, pp. 641-649.

8. Louthan Jr., M.R., "Hydrogen Embrittlement of Metals," *Materials Science and Engineering*, Vol. 10, 1972, pp. 357-368.

9. Louthan Jr., M.R., "Hydrogen Embrittlement of Metals: A Primer for the Failure Analyst," *Journal of Failure Analysis & Prevention*, Vol. 8, No. 3, 2008, pp. 289-307.

10. Fontana, M.G., "*Corrosion Engineering*," McGraw-Hill, New York, 1986.

11. Jung, J.K., "Hydrogen Embrittlement Behavior of High Mn TRIP/TWIP Steels," *Korean Journal of Materials Research*, Vol. 18, 2008, pp. 394-399.

12. Kolachev, B.A., Gabidullin, R. "Forms of the Manifestation of Hydrogen Embrittlement in Metals and Alloys." *Soviet Materials Science* (English Translation of Fiziko-Khimicheskaya Mekhanika Materialov), Vol. 12, 1976, pp. 463-468.

13. Korzh, T.V., "Effect of Weld Metal Structure on Its Susceptibility to Hydrogen Embrittlement," *Welding Production* (English translation of Svarochnoe Proizvodstvo), Vol. 32, 1985, pp. 23-25.

14. Takagi, S., "Evaluation of Hydrogen Embrittlement Susceptibility of High Strength Steel by the Weibull Stress," *Nippon Kinzoku Gakkaishi/Journal of the Japan Institute of Metals*, Vol. 65, 2001, pp. 1073-1081.

15. Thomas, R.L.S., Scully, J.R. and Gangloff, R.P., "Internal Hydrogen Embrittlement of Ultrahigh-Strength AERMET 100 Steel," *Metallurgical and Materials Transactions A: Physical Metallurgy and Materials Science*, Vol. 34, 2003, pp. 327-344.

16. Tiwari, G.P., "A Study of Internal Hydrogen Embrittlement of Steels," *Materials Science and Engineering* A, Vol. 289, 2002, pp. 269-281.

17. Vasilenko, I.I., Khomitskii, Y.N., and Koval, V.P., "Mechanism of Influence of Certain Alloying Elements on the Hydrogen Embrittlement of Iron," *Soviet Materials Science*, Vol. 18, 1982, pp. 205-209.

18. Ebtehaj, K., Hardie, D., and Parkins, R., "The Stress Corrosion and Pre-Exposure Embrittlement of Titanium in Methanolic Solutions of Hydrochloric Acid," *Corrosion Science*, Vol. 25, 1985, pp. 415-29.

19. Kim, T.-K., "Characteristics of Hydriding and Hydrogen Embrittlement of the Ti-Al-Zr Alloy," *Annals of Nuclear Energy*, Vol. 29, 2002, pp. 2041-2053.

20. Wyman, L.L., "Copper Embrittlement," *American Institute of Mining and Metallurgical Engineer,*: Vol. 137, 1933, pp. 291-296.

21. Vollmer, L.W., and B.B. Westcott, "Effect of Hydrogen Sulphide on Wire Rope," *Oil and Gas Journal*, Vol. 29, No. 22, 1930, pp. 64-141.

22. Elliss, H., "Gases in Ferrous Materials -- II," *Iron and Steel Industry*, Vol. 10, No. 11, 1937, pp. 487-491.

23. Lease, J.W.M., "Hydrogen Embrittlement Occurring in Pickling Solution for Rods," *Wire and Wire Products*, Vol. 10, No. 3, 1935, pp. 114-122.

24. Nakashima, K., "Effect of High-Pressure Hydrogen Exposure on Wear of Polytetrafluoroethylene Sliding Against Stainless Steel," *Proceedings of the Institution of Mechanical Engineers, Part J: Journal of Engineering Tribology*, Vol. 224, 2010, pp. 285-292.

25. Hollis, A.C., and Scully, J.C., "The Stress Corrosion Cracking and Hydrogen Embrittlement of Titanium in Methanol-Hydrochloric Acid Solution," *Corrosion Science*, Vol. 34, 1993. pp. 821-35.

26. Nagaoka, A., Yokoyama, K., and Sakai, J., "Evaluation of Hydrogen Absorption Behaviour During Acid Etching for Surface Modification of Commercial Pure Ti, Ti-6Al-4V and Ni-Ti Superelastic Alloys," *Corrosion Science,* Vol. 52, 2010, pp. 1130-1138.

27. Nishimura, R., Shirono, J., and Jonokuchi, A., "Hydrogen-Induced Cracking of Pure Titanium in Sulphuric Acid and Hydrochloric Acid Solutions Using Constant Load Method," *Corrosion Science*, 2008. Vol. 50, 2008, pp. 2691-2697.

28. Ogawa, T., "Distribution and Thermal Desorption Behavior of Hydrogen in Titanium Alloys Immersed in Acidic Fluoride Solutions," *Journal of Alloys and Compounds*, Vol. 396, 2005, pp. 269-74.

29. Pyun, S.-I., "Effects of Tribologically-Penetrated Hydrogen on the Abrasive Wear of Mild Steel in H2SO4 Solution," *Steel Research,* Vol. 62, No. 7, 1991, pp. 314-319.

30. Asaoka, K., Yokoyama, K., and Nagumo, M., "Hydrogen Embrittlement of Nickel-Titanium Alloy in Biological Environment," *Metallurgical and Materials Transactions* A (Physical Metallurgy and Materials Science), Vol. 33, No. A, 2002, pp. 495-501.

31. Rodrigues, D.C., "In Vivo Severe Corrosion and Hydrogen Embrittlement of Retrieved Modular Body Titanium Alloy Hip-Implants," *Journal of Biomedical Materials Research - Part B Applied Biomaterials*, Vol. 88, 2009, pp. 206-219.

32. Jiang, X., "A Study of the Corrosive Wear of Ti-6Al-4V in Acidic Medium," *Wear*, Vol. 129, No. 2, 1989, pp. 293-301.

33. Zhang, T. C., Jiang, X. X., and Li, S. Z., "Hydrogen-Induced Embrittlement Wear of a High-Strength, Low-Alloy Steel in an Acidic Environment," *CORROSION NACE International*, Vol. 53, No.3, 1997.

34. Rabinowicz, E., *Friction and Wear of Materials*, New York: John Wiley and Sons, 1995.

35. Gwidon W. and Stachowiak, A.W.B., *Engineering Tribology,.*, Amsterdam: Elsevier Butterworth-Heinemann, 2005.

36. ASTM Standard A370-09a: Standard Test Methods and Definitions for Mechanical Testing of Steel Products, Annual Book of ASTM Standards, ASTM International, West Conshohocken, PA, 2009.

37. ASTM ASTM E 8/E8M: Test Methods for Tension Testing of Metallic Materials, Annual Book of ASTM Standards, ASTM International, West Conshohocken, PA, 2009.

38. ASTM, ASTM E 110 Test Method for Indention Hardness of Metallic Materials by Portable Hardness Testers, Annual Book of ASTM Standards, ASTM International, West Conshohocken, PA, 2010.

39. ASTM, ASTM E 10 Test Method for Brinell Hardness of Metallic Materials, Annual Book of ASTM Standards, ASTM International, West Conshohocken, PA, 2009.

40. ASTM, ASTM E 18 Test Methods for Rockwell Hardness of Metallic Materials, Annual Book of ASTM Standards, ASTM International, West Conshohocken, PA, 2008.

41. ASTM, E190 Test Method for Guided Bend Test for Ductility of Welds, Annual Book of ASTM Standards, ASTM International, West Conshohocken, PA, 2008.

42. ASTM, ASTM E 290 Test Methods for Bend Testing of Materials for Ductility, Annual Book of ASTM Standards, ASTM International, West Conshohocken, PA, 2009.

43. ASTM, ASTM E 23 Test Methods for Notched Bar Impact Testing of MetallicMaterials, Annual Book ofASTM Standards, ASTM International, West Conshohocken, PA, 2007.

44. Srikar, V. and Spearing, S., "A Critical Review of Microscale Mechanical Testing Methods Used in the Design of Microelectromechanical Systems," *Experimental Mechanics*, Vol. 43, No. 3, 2003, pp. 238-247.

45. *Small Specimen Test Techniques Forth Volume STP 1418*, ed. J.D.L. M.A. Sokolov, G.E. Lucas. Vol. 4. 2002, West Conshohocken, PA: ASTM International.

46. *Small Specimen Test Techniques STP 1329*, ed. S.T.R. William R. Corwin, Eric van Walle. 1998, West Conshohocken, PA: ASTM Internatinal.

47. *Small Specimen Test Techniques: 5th Volume STP1502*, ed. M.A. Sokolov. Vol. 5. 2009, West Conshohocken, PA: ASTM International.

48. Vorlicek, V., Exworthy, L.F., and Flewitt, P.E.J., "Evaluation of a Miniaturized Disc Test for Establishing the Mechanical Properties of Low-Alloy Ferritic Steels," *Journal of Materials Science*, Vol. 30 No. 11, 1995, pp. 2936-2943.

49. Manahan, M.P. and Harling, O.K., *Determining Mechanical Behavior of Solid Materials Using Miniature Specimens*. Battelle Development Corporation: United States, 1986.

50. Manahan, M.P., Argon, A.S. and Harling, O.K., "The Development of a Miniaturized Disk Bend Test for the Determination of Postirradiation Mechanical Properties," *Journal of Nuclear Materials*, Vol. 103-104, 1981, pp. 1545-1550.

51. Mao, X., and Takahashi, H., "Development of a Further-Miniaturized Specimen of 3mm Diameter for TEM Disk Tests*," Journal of Nuclear Materials*, Vol. 105, No. 1, 1987, pp. 42-52.

52. Mao, X., Takahashi, H., and Kodaira, T., "Estimation of Mechanical Properties of Irradiated Nuclear Pressure Vessel Steel by Use of Subsized ct Specimen and Small Punch Specimen," *Scripta Metallurgica et Materialia*, Vol. 26, No. 11, 1991, pp. 2487-2490.

53. Foulds, J.R., "Fracture Toughness by Small Punch Testing," *Journal of Testing and Evaluation*, Vol. 23, No. 1, 1995, pp. 3-10.

54. Brookfield, D.J., "Material PropertiesFrom Small Specimens Using the Punch and Bulge Test," *Journal of Strain Analysis for Engineering Design*, Vol. 34, No. 6, 1999, pp. 423-435.

55. Foulds, J.R., Jewett, C.W., and Viswanathan, R., "Miniature Specimen Test Technique for FATT," *International Power Generation Conference*, 6-10 October, San Diego, CA.

56. Giddings, V.L., "A Small Punch Test Technique for Characterizing the Elastic Modulus and Fracture Behavior of PMMA Bone Cement Used in Total Joint Replacement," *Biomaterials*, Vol. 22, No. 13, 2001, pp. 1875-1881.

57. Kurtz, S.M., "Miniature Specimen Shear Punch Test for UHMWPE Used in Total Joint Replacements" *Biomaterials*, Vol. 23, No. 9, pp. 1907-1919.

58. Rodriguez, C., "Mechanical Properties Characterization of Heat-Affected Zone Using the Small Punch Test," *Welding Journal* Vol. 88, No. 9, 2009, pp. 188-192.

59. Lee, J., Kim, I., and Kimura, A., "Application of Small Punch Test to Evaluate Sigma-Phase Embrittlement of Pressure Vessel Cladding Material," *Journal of Nuclear Science and Technology*, Vol. 40, No. 9, 2003, pp. 664-671.

60. Zidan, A.A., and Brookfield, D.J., "A Technique for the Determination of Post-Yield Material Properties from the Small Punch Test," *Journal of Strain Analysis for Engineering Design*, Vol. 26, No. 4, 2003, pp. 367-370.

61. Milicka, K., and Dobe, F., "Small Punch Testing of P91 Steel," *International Journal of Pressure Vessels and Piping*, Vol. 89, no. 9, 2006, pp. 625-634.

62. Wei, T., "Assessment of the Fracture Toughness of 6061 Aluminium by the Small Punch Test and Finite Element Analysis," *Materials and Testing Conference*, 10 October - 2 November 2005, 2006, Fremantle, WA.

63. Hamilton, M.L., Toloczko, M. B., Edwards, D. J., Sommer, W. F., Borden, M. J., Dunlap, J. A., Stubbins, J. F., and Lucas, G. E., "Correlation Between Shear Punch and Tensile Data for Neutron Irradiated Aluminium Alloys," *American Society for Testing and Materials*, Vol. 1270, 1996, pp. 1057-1067.

64. Ezugwu, E.O., and Wang, Z.M., "Titanium Alloys and Their Machinability--A Review," *Journal of Materials Processing Technology*, Vol. 63, No. 3, 1997, pp. 262-274.

65. Kaufman, J.G., *Properties of Aluminum Alloys Tensile, Creep, and Fatigue Data at High and Low Temperatures*, New York: ASM International, 2000.

66. Gibbons, M.R., Richards, W.J., and Shields, K., "Detection of Hydrogen in Titanium Aircraft Components Using Neutron Tomography," *Proceedings of SPIE - The International Society for Optical Engineering*, Vol. 2945, 1996, pp. 104-115.

67. Jiang, X., "Study of the Corrosive Wear of Ti-6Al-4V in Acidic Medium," *Wear*, Vol. 129, 1989, pp. 293-301.

68. Donachie, M.J., *TITANIUM A Technical Guide*. 1988, Metals Park, OH: ASM International.

69. ASTM B209M-07: *Standard Specification for Aluminum and Aluminum-Alloy Sheet and Plate*, Annual Book ofASTM Standards, ASTM International, West Conshohocken, PA, 2007.

70. SAE, "Aluminum Alloy, Die and Hand Forgings," AMS-A-22771A, 2008.

71. ASTM B265-10: *Standard Specification for Titanium and Titanium Alloy Strip, Sheet, and Plate*, Annual Book ofASTM Standards, ASTM International, West Conshohocken, PA, 2009.

72. Eskner, M. and Sandstrom, R., "Mechanical Property Evaluation Using the Small Punch Test." *Journal of Testing and Evaluation*, 2005. 33(4): p. 282-289.

73. Yilbas, B.S., "Hydrogen Embrittlement of Ti-6Al-4V Alloy with Surface Modification by TiN Coating." *International Journal of Hydrogen Energy*, Vol. 23, No. 6, 1998, pp. 483-489.

APPENDIX A

The overall percent error for each alloy was calculated using Equation 15.

$$\%error = \frac{1}{N}\left[\sum_{i=1}^{N}\frac{F(i)-\left[F(i)+std(i)\right]}{F(i)}\right] \qquad (12)$$

Where:

N = total number of data points

F = F is the average force measurment at point i, in Newtons

std = is the standard deviation at point i

This error uses the average value as the accepted value and the deviation at each time step as the measured value. The percent error takes the average of the individual percent error at each data point. The area under the force verus extension curve up to the maximum force (T) was approximated using the Trapoziod Method of definite intergration shown in Equation 16.

$$T = \int_{a}^{b} f(x)dx = \frac{b-a}{N}\left[\frac{f(a)+f(b)}{2}+\sum_{K=1}^{N-1} f\left(a+K\frac{b-a}{N}\right)\right] \qquad (13)$$

Where:

T = maximum force in Newtons

N= total number of data points

a and f(a) are reference points of zero when the ball just touches the surface of the specimen

b = depth of the ball when the maximum force is reached in mm

f(b) = maximum force in Newtons

APPENDIX B

In order to determine the surface area between the ball bearing and the specimens during testing Figure 56 was used to define R as the radius of the ball bearing and δ as the extension of the ball bearing into the material.

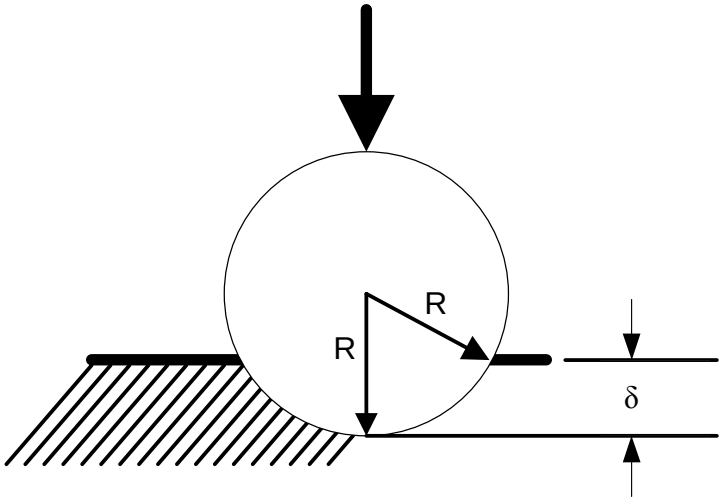

Figure 56: Cross-section of ball bearing pushing into material

A polar coordinate system was set up and can be seen in Figure 57.

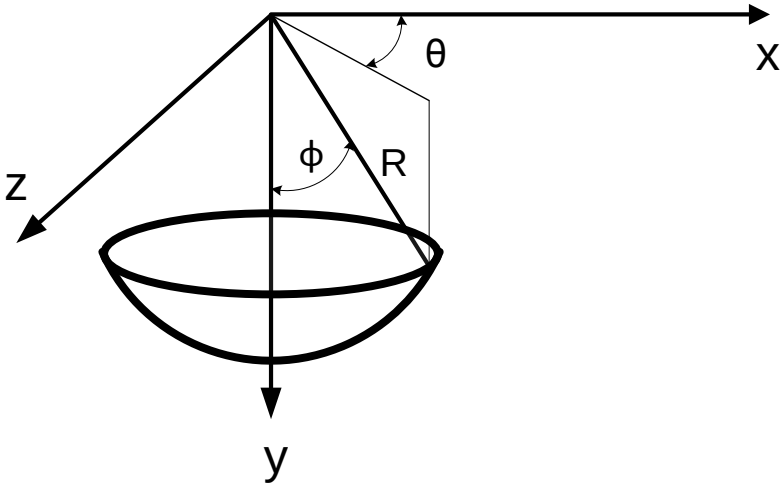

Figure 57: Coordinate system used to calculate surface contact area

The relation between the angles in Figure 56 and Figure 57 can be seen in Figure 58

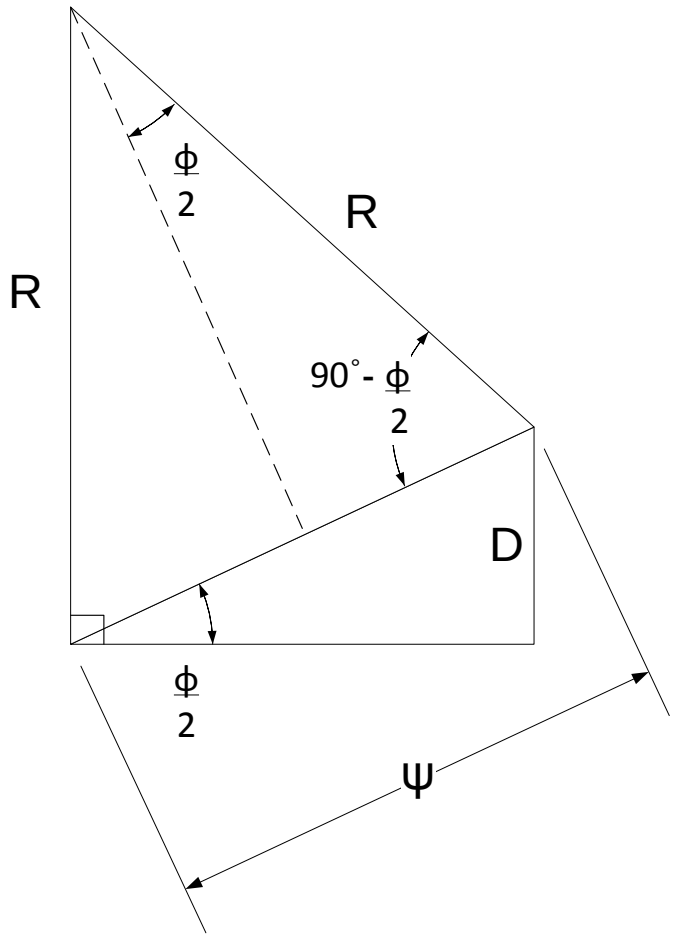

Figure 58: Geometry and symbols used to calculate surface contact area

The relation between the distance ψ and the angle ϕ was established as:

$$\frac{\psi}{2} = Rsin\left(\frac{\phi}{2}\right)$$

$$\psi = 2Rsin\left(\frac{\phi}{2}\right)$$

The relationship between the extension of the ball bearing into the material and the angle ϕ was found to be:

$$\delta = \psi sin\left(\frac{\phi}{2}\right)$$

$$\delta = 2Rsin\left(\frac{\phi}{2}\right) sin\left(\frac{\phi}{2}\right)$$

$$\delta = 2Rsin^2\left(\frac{\phi}{2}\right)$$

$$sin\left(\frac{\phi}{2}\right) = \sqrt{\frac{\delta}{2R}}$$

$$\frac{\phi}{2} = sin^{-1}\sqrt{\frac{\delta}{2R}}$$

$$\phi = 2sin^{-1}\sqrt{\frac{\delta}{2R}}$$

In order to find the surface area the definite double integral was taken for the angles ϕ and θ and is:

$$Surface\ Contace\ Area = \int_0^{2\pi}\int_0^{\pi} R^2 sin\phi d\phi d\theta$$

$$Surface\ Contact\ Area = \int_0^{2\pi}\int_0^{\phi} R^2 sin\phi d\phi d\theta$$

$$Surface\ Contact\ Area = \int_0^{2\pi} \int_0^{2sin^{-1}\sqrt{\frac{\delta}{2R}}} R^2 sin\phi d\phi d\theta$$

Solving the double integral becomes:

$$Contact\ Area = -2\pi \mathrm{R}^2 \cos\left[2\sin^{-1}\left(\sqrt{\frac{2\delta}{4\mathrm{R}}}\right) - 1\right]$$

Substituting 3mm for R gives the final relation:

$$Contact\ Area = -18\pi \cos\left[2\sin^{-1}\left(\sqrt{\frac{\delta}{12}}\right) - 1\right]$$

VITA

Matthew Wayne Sanders received his Bachelor of Science degree in mechanical engineering from Texas A&M University in 2009. He entered the mechanical engineering Master's program at Texas A&M University in June 2009, and he received his Master of Science degree in August 2010. His main research interests include in characterization of hydrogen damaged material using the Small Punch Test. He is also interested in the study of fundamental materials science as well as mechanics of materials. Mr. Sanders may be reached at Stress Engineering Services, Inc., 13800 Westfair East Dr., Houston, TX 77041. His email address is mattsanders09@gmail.com. His current contact information may be found from his Master's Thesis advisor, Dr. Hong Liang of the Mechanical Engineering Department, Texas A&M University.